UNIVERSIDAD COMPLUTENSE DE MADRID

FACULTAD DE CIENCIAS FÍSICAS

TESIS DOCTORAL

Advanced electron microscopy characterization of complex oxide interfaces
Estudio de interfases en óxidos complejos por técnicas avanzadas de microscopía electrónica

MEMORIA PARA OPTAR AL GRADO DE DOCTOR

PRESENTADA POR

Gabriel Sánchez Santolino

Directores

María Varela del Arco
Jacobo Santamaría Sánchez-Barriga

Madrid, 2015

Facultad de Ciencias Físicas
Universidad Complutense de Madrid

Advanced electron microscopy characterization of complex oxide interfaces

Estudio de interfases en óxidos complejos por técnicas avanzadas de microscopia electrónica

Memoria presentada por

Gabriel Sánchez Santolino

para optar al grado de Doctor en Ciencias Físicas

Directores:

María Varela del Arco
Jacobo Santamaría Sánchez-Barriga

Madrid, 2015

Agradecimientos

Este trabajo es el resultado de cuatro largos años dedicados a aprender, no sólo en el ámbito científico, sino también en lo personal. En este tiempo he aprendido a ser mejor compañero, mejor persona y mejor amigo. Nada de esto, ni de todo el trabajo reflejado en esta tesis habría sido posible sin las personas que me han apoyado desde el principio y sin las personas a las que he conocido durante este proceso.

En primer lugar, quiero agradecer a María Varela por haberme dado la oportunidad de realizar un sueño: dedicarme a la investigación. Quiero agradecerle además, todo lo que me ha enseñado estos años en los que ha sabido exigirme y valorarme, apoyarme y alentarme, sacando lo mejor de mí en cada momento. También quiero agradecer a Jacobo Santamaría por abrirme las puertas cuando aún estaba estudiando la carrera y haber sido el guía científico de este proyecto.

No podían faltar en estos agradecimientos todos los compañeros con los que he trabajado estos años: A Flavio, que me ayudó a dar mis primeros pasos en la investigación. A todos los profesores del grupo: Carlos León, Alberto Rivera, Zouhair Sefrioui, Javier Barriocanal y Rainer Schmidt por sus aportes científicos y sus consejos. Al resto de estudiantes que durante estos años han sufrido a mi lado: A Javi por ser un maestro, a Mirko por darnos a todos una clase magistral de cultura italiana día a día, a Ana por su entusiasmo y la felicidad que desprende, a Fabián por su sinceridad, a David por enseñarnos a todos que las cosas se consiguen con esfuerzo. Y por supuesto, a Mariona, por todo lo que hemos compartido, por su apoyo personal y su compañía durante las estancias en Oak Ridge.

I would also like to thank the people from the STEM group, at the Oak Ridge National Laboratory, formerly directed by Steve Pennycook and now by Matt Chisholm. I will always be grateful for making me feel like part of the group. Thanks to Steve Pennycook for all the advice and to Andy Lupini for being always so helpful, any day, anytime.

Thank Janie for the making the sample preparation a funny step of the process. Thank you all the rest of you for teaching me how to survive in this world.

Todavía en Oak Ridge, quisiera agradecer a la *Spanish Mafia.* Habéis estado siempre ahí cuando lo necesitaba en lo profesional y habéis aportado toda la vida social posible a un lugar tan especial como Tennessee. A Jaume por acogerme como su pupilo desde que aterricé en Atlanta en mi primer viaje. A Neven por sus consejos, las conversaciones en el *pluri* y por su ayuda para corregir esta tesis. A Manuel y Lidia por tratarnos a todos como parte de su familia. A Juan Carlos por sus enseñanzas y su alegría, a Leo por su compañerismo, a Juan por descifrarme lo que es el mundo teórico y a Raúl por ser un grandísimo anfitrión.

También quiero darles las gracias a José González Calbet, por haber traído a Madrid la corrección de aberraciones y a Oscar Rodríguez y Beatriz Martínez por las muestras de TiO_2 y por un fabuloso trabajo.

A mis amigos, por todos los buenos ratos pasados durante estos años, os voy a echar de menos.

Gracias a mis padres, por haberme inculcado desde pequeño el interés por la ciencia y a ellos y a mi hermana por todo su apoyo y sus ánimos durante los malos momentos.

Y por último, gracias Inés. Sabes que lo mío no son las palabras y que no podría plasmar aquí mis agradecimientos por todo lo que has hecho por mí estos años. Sólo quiero que sepas que eres la fuente de mi motivación, mis fuerzas y mi felicidad. Te quiero.

Contents

Resumen en español **1**

Introducción 1

Resultados 2

Conclusiones 4

Bibliografía 5

Chapter 1: Introduction **9**

Interfaces between complex oxide materials 10

Aberration corrected STEM-EELS 12

Motivation and aims of this thesis 13

Thesis outline 14

Chapter 2: Experimental methods **17**

Scanning Transmission Electron Microscopy 18

Electron energy-loss spectroscopy 24

Imaging and EELS advanced analysis techniques 28

Atomic column position mapping 29

Peak Pairs analysis (PPA) 31

EELS compositional quantification 33

Multiple linear least-square fitting 34

Principal component analysis (PCA) 36

Electron Microscopes 38

Sample growth 39

Specimen preparation 41

Chapter 3: Irradiation effects on the surface of oxide materials. 43

Introduction 44

Two paradigmatic titanium oxides: TiO_2 and $SrTiO_3$ 45

Experimental results 46

Transport characterization 47

Surface characterization 48

STEM-EELS characterization 49

Specimen preparation: damage vs. no damage? 50

Surface phases in $SrTiO_3$ 52

Discussion 59

Chapter 4: Origin of ionic conductivity barriers at Y_2O_3 stabilized ZrO_2 grain boundaries 63

Introduction 64

Ytrium stabilized zirconia (Y_2O_3 stabilized ZrO_2) 66

Experimental results 68

Transport measurements 68

Structural characterization 70

Strain analysis 71

EELS characterization 74

Density functional theory calculations 79

Discussion 81

Chapter 5: Oxygen Octahedral rotations in $LaMnO_3/SrTiO_3$ superlattices 85

Introduction 86

$LaMnO_3$ crystalline structure 87

Experimental results 90

Structural analysis 90

Oxygen octahedral rotations in $LaMnO_3$ bulk 95

Octahedral rotations in $LMO_{17\ u.c.}$ / $STO_{2\ u.c.}$ superlattices 96

Octahedral rotations in $LMO_{17\ u.c.}$ / $STO_{12\ u.c.}$ superlattices 99

Discussion 101

Chapter 6: Resonant tunneling transport through confined electronic states in multiferroic heterostructures 103

Introduction 104

$La_{0.7}Sr_{0.3}MnO_3$ 105

$BaTiO_3$ 108

Experimental results 110

Transport measurements 111

Structural characterization 113

Study of the ferroelectric polarization 122

Discussion 129

Chapter 7: Summary 133

Experimental Results 133

Conclusion 135

Annex 137

List of publications 137

Conference contributions 139

Short research stays 141

Bibliography 145

Resumen en español

Introducción

Pequeños cambios a nivel atómico de la estructura, composición o estado electrónico de un material pueden producir sorprendentes efectos macroscópicos. En particular, en óxidos complejos basados en metales de transición, un gran número de fenómenos físicos como transiciones metal-aislante, magnetorresistencia colosal, superconductividad de alta temperatura o multiferroicidad son extremadamente sensibles a estas variaciones, que además dan lugar a complicados diagramas de fases (*1–5*). Por tanto, para abordar el estudio de sistemas con tales características, técnicas experimentales con capacidad de analizar materiales a escala atómica y en el espacio real se hacen indispensables. La microscopía electrónica de transmisión con barrido (STEM) combinada con la espectroscopia de pérdida de energía de electrones (EELS) forman una pareja con posibilidades únicas para estos estudios (*6*). Estas técnicas han crecido enormemente desde el desarrollo del corrector de aberración esférica en la última década (*7–10*). Los límites de resolución espacial se encuentran actualmente por debajo de la frontera de los 0.5 Å (*11–13*), lo que nos permite estudiar átomos individuales dentro de un cristal (*14*). El uso de estos microscopios electrónicos corregidos supone una herramienta única para el estudio de sistemas complejos, más aún cuando la dimensionalidad se reduce a pocos nanómetros como en películas delgadas o interfaces. En estos casos, técnicas de difracción promediadas macroscópicamente pueden no ser suficientemente sensibles a los parámetros que rigen la física relevante y por tanto, la gran sensibilidad espacial de la microscopía electrónica supone una gran ventaja. El objetivo principal de este trabajo será precisamente establecer la conexión entre los mecanismos a nivel atómico y las propiedades físicas de una serie de sistemas basados en óxidos complejos cuidadosamente escogidos. Analizaremos en el espacio real fluctuaciones mínimas, casi por debajo del umbral de detectabilidad, responsables últimas del comportamiento macroscópico.

Resultados

Con este fin, se han analizado los siguientes ejemplos paradigmáticos donde mínimas concentraciones de defectos puntuales o cambios estructurales locales difíciles de detectar afectan profundamente la respuesta macroscópica del sistema:

- En primer lugar, se ha irradiado de forma controlada la superficie de óxidos complejos con el objetivo de inducir nuevas fases superficiales. Analizando los sistemas tratados mediante microscopía electrónica se ha observado cómo estos procesos producen la formación de una capa de TiO con alto grado cristalino en la superficie de monocristales de TiO_2 (*15*) y como además dan lugar a estados metálicos superficiales en un aislante de bandas como es el $SrTiO_3$ (*16*, *17*). Este último fenómeno se produce por la formación y reorganización de vacantes de oxígeno inducidas mediante la irradiación que dopan electrónicamente los átomos de titanio superficiales dando lugar a la variación de la estructura de bandas en el sistema y en consecuencia a una transición aislante-metal.

- Continuando este estudio en sistemas más complejos, se ha analizado como la reestructuración electrónica debida a la presencia de vacantes de oxígeno puede explicar el bloqueo observado en fronteras de grano de conductores iónicos, materiales que se emplean habitualmente en forma policristalina, y cuyo rendimiento se ve altamente afectado por dicho bloqueo de la conductividad iónica en dichas fronteras (147–149). La combinación de análisis mediante microscopía electrónica y cálculos DFT ha permitido desvelar una fuerte segregación de Y hacia las posiciones atómicas expansivas dentro de los núcleos de dislocación, además de la presencia de vacantes de oxígeno estructurales en la frontera. Estas variaciones composicionales producen una falta de estequiometria en una región de 5 Å a ambos lados de la frontera de grano, descartando la presencia de una amplia zona de carga espacial, como se suponía anteriormente (*18–20*). Además, los electrones cedidos por las vacantes de oxígeno son capturados en estados electrónicos accesibles en la frontera de grano, cargando eléctricamente la frontera y dando lugar a una barrera de potencial. De esta manera se ha explicado por primera vez el origen electroestático del bloqueo

iónico en fronteras de grano de materiales con importantes aplicaciones energéticas.

- Se ha querido abordar también el estudio de pequeñas distorsiones estructurales, que son ahora detectables gracias a la gran sensibilidad espacial de la microscopía con corrector de aberraciones. En especial, se han analizado mediante espectroscopia EELS con resolución atómica y nuevos métodos de imagen con mayor sensibilidad a átomos ligeros, las distorsiones colectivas de la red de oxígeno en heteroestructuras de óxidos complejos y su relación con la aparición de estados físicos inexistentes en los materiales masivos. En superredes compuestas por el aislante de Mott $LaMnO_3$ y el aislante de bandas $SrTiO_3$ se ha encontrado una correlación entre rotaciones del octaedro de oxígenos (BO_6) y la tensión epitaxial inducida al variar el espesor de las capas de titanato. Además, estas distorsiones se relacionan con la estabilización de una fase interfacial ferromagnética y conductora en el sistema (*21*, *22*). Se ha extendido este análisis a sistemas más complejos como uniones túnel multiferroicas donde se ha obtenido la configuración de dominios ferroeléctricos midiendo las distorsiones en la red de oxígenos para cada celda unidad. Este estudio muestra una de las primeras observaciones experimentales de una configuración de dominios ferroeléctricos tipo head-to-head en capas de $BaTiO_3$ ultra-delgadas. Las capas muestran una inversión de la polarización en la dirección fuera del plano mediante un gradiente de polarización muy pronunciado que alcanza unos valores de saturación cercanos al valor del material masivo en las interfases. Se ha encontrado además la presencia de carga de apantallamiento confinada a la pared de dominio que genera estados estados electrónicos accesibles en el interior de la barrera ferroeléctrica que proporcionan los mecanismos para estabilizar un tuneleamiento cuántico resonante.

Conclusiones

A lo largo de esta tesis hemos mostrado como la microscopia electrónica con corrector de aberraciones es una técnica esencial para el análisis de materiales con resolución atómica. Hemos visto como pequeñas distorsiones estructurales o fluctuaciones en la composición química a nivel atómico pueden dan lugar a una gran variedad de fenómenos físicos macroscópicos. Actualmente podemos analizar pequeñas concentraciones de defectos, variaciones en la tensión epitaxial o fronteras de dominio ferroeléctricas con un nivel de detalle sin precedentes, estableciendo la conexión entre los mecanismos atómicos y las propiedades electrónicas del sistema. El continuo desarrollo de estas técnicas experimentales, sobrepasando los límites actuales en la resolución espacial y en energía hacen vislumbrar un futuro prometedor tanto para la ciencia de materiales como para la microscopía electrónica. Ahora, más que nunca, está a nuestro alcance la exploración de fronteras a escala atómica aún por revelar.

Bibliografía

1. E. Dagotto, *Complexity in strongly correlated electronic systems.* Science. 309, 257–262 (2005).

2. E. Dagotto, T. Hotta, A. Moreo, *Colossal magnetoresistant materials: the key role of phase separation*. Phys. Rep. 344, 1–153 (2001).

3. M. Imada, A. Fujimori, Y. Tokura, *Metal-insulator transitions*. *Rev. Mod. Phys.* 70 (1998), pp. 1039–1263.

4. Y. Tokura, N. Nagaosa, *Orbital Physics in Transition-Metal Oxides*. *Science (80-.).* 288 (2000), pp. 462–468.

5. Y. Tokura, *Correlated-Electron Physics in Transition-Metal Oxides*. Phys. Today. 56, 50 (2003).

6. M. Varela *et al.*, *Materials Characterization in the Aberration-Corrected Scanning Transmission Electron Microscope*. Annu. Rev. Mater. Res. 35, 539–569 (2005).

7. O. Scherzer, *Über einige Fehler von Elektronenlinsen*. Zeitschrift für Phys. A Hadron. Nucl. (1936).

8. O. Scherzer, *The Theoretical Resolution Limit of the Electron Microscope*. J. Appl. Phys. 20, 20 (1949).

9. M. Haider, S. Uhlemann, E. Schwan, H. Rose, *Electron microscopy image enhanced*. Nature. 392, 5–6 (1998).

10. O. L. Krivanek, N. Dellby, A. R. Lupini, *Towards sub-Å electron beams*. Ultramicroscopy. 78, 1–11 (1999).

11. O. L. Krivanek, P. D. Nellist, N. Dellby, M. F. Murfitt, Z. Szilagyi, *Towards sub-0.5 Å electron beams*. Ultramicroscopy. 96, 229–37 (2003).

12. R. Erni, M. Rossell, C. Kisielowski, U. Dahmen, *Atomic-Resolution Imaging with a Sub-50-pm Electron Probe*. Phys. Rev. Lett. 102, 1–4 (2009).

13. Y. Sawada, H. Shimura, N. Satoh, K. Okinishi, E. Hosokawa, F. Shibata, N. Ikuhara, *Resolving 45 pm with 300 kV Aberration Corrected STEM*. Microsc. Microanal. 20, 124–125 (2014).

14. O. L. Krivanek *et al.*, *Atom-by-atom structural and chemical analysis by annular dark-field electron microscopy*. Nature. 464, 571–574 (2010).

15. B. Pabón *et al.*, *Formation of titanium monoxide (001) single-crystalline thin film induced by ion bombardment of titanium dioxide (110)*. Nat. Commun. 6 (2015).

16. F. Bruno, J. Tornos, M. del Olmo, G. Santolino, *Anisotropic magnetotransport in $SrTiO_3$ surface electron gases generated by Ar^+ irradiation*. Phys. Rev. B. 83, 1–8 (2011).

17. G. Sánchez-Santolino *et al., Characterization of surface metallic states in $SrTiO_3$ by means of aberration corrected electron microscopy.* Ultramicroscopy. 127, 109–113 (2012).

18. X. Guo, R. Waser, *Electrical properties of the grain boundaries of oxygen ion conductors: acceptor-doped zirconia and ceria*. Prog. Mater. Sci. 51, 151–210 (2006).

19. K. Kliewer, J. Koehler, *Space Charge in Ionic Crystals. I. General Approach with Application to NaCl*. Phys. Rev. 140, A1226–A1240 (1965).

20. J. Maier, *Ionic conduction in space charge regions*. Prog. Solid State Chem. 23, 171–263 (1995).

21. J. Garcia-Barriocanal *et al., "Charge leakage" at $LaMnO_3/SrTiO_3$ interfaces.* Adv. Mater. 22, 627–32 (2010).

22. G. Sanchez-Santolino *et al., Oxygen octahedral distortions in $LaMO_3/SrTiO_3$ superlattices.* Microsc. Microanal. 20, 825–31 (2014).

Chapter 1: Introduction

Electronic reconstructions produced by atomic scale variations of the structure and composition in epitaxial interfaces between transition metal oxides (TMOs) can give rise to dramatic macroscopic physical effects (*1*–*3*). The presence of many competing interactions in these materials leads to complicated phase diagrams (*4*) and a wide range of physical phenomena, such as metal-insulator transitions, colossal magnetoresistance, high temperature superconductivity, multiferroicity and so on (*4*–*8*). In order to harness such challenging properties, experimental techniques with probes capable of studying materials in real space and down to the atomic scale are essential. Aberration corrected scanning transmission electron microscopy (STEM) combined with electron energy loss spectroscopy (EELS) techniques form a duet with unique capabilities along these lines (*9*). Being able to observe and explain the correlation between the atomic and the macroscopic worlds provides an exciting path towards the discovery of new physics and also for the development of devices based on novel physical functionalities. The work included in this thesis aims at establishing this link for a number of carefully chosen examples of oxides for energy, electronic or spintronic applications.

Interfaces between complex oxide materials

Interfaces between TMOs pose a promising scenario to pursue novel physical effects due to the possibility of combining materials with very distinct physical properties in high quality heterostructures (*2*). Many of the aforementioned physical properties stem from the presence of electronic correlations in TMOs (*8*). The complex interactions between the spin, charge, lattice and orbital degrees of freedom give rise to a wide variety of electronic phases. The behavior of electrons in these materials cannot be described by one-electron band models, since each single electron is subject to unscreened Coulomb interactions with its neighbors (*10*). Thus, physical states that are not predicted by conventional band theories may arise. For example, some materials may present an insulating state for a partial occupancy of the energy bands for which band theory predicts the opposite. This effect happens when the Coulomb repulsion energy between electrons is strong enough to create an energy gap. This state is called a Mott insulator.

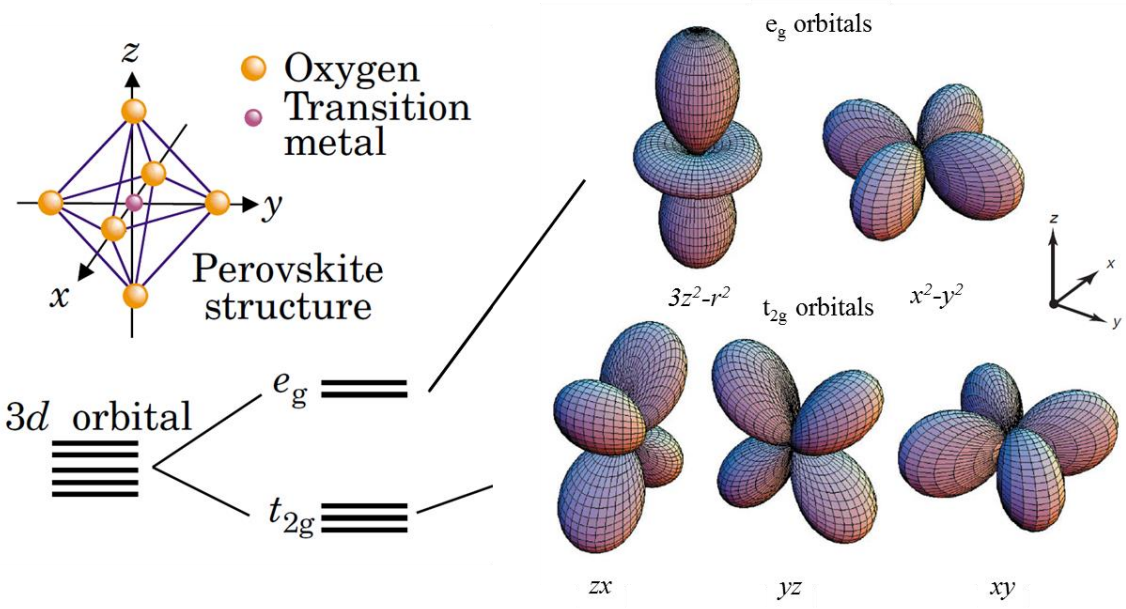

Figure 1.1: Schematic illustrating how degenerate orbitals at the atomic level are splitted by a crystal field potential. The quantum mechanical *d* orbitals in the octahedral coordination of the O^{2-} are shown on the right. Adapted from ref. (*8*)

Many TMOs present a perovskite crystalline structure, where the transition-metal ion is surrounded by six doubly negative charged oxygen ions. This arrangement produces a crystal field potential that lifts the degeneracy of the five-fold *d* orbitals of the TMO

(Figure 1.1). They are split into two-fold degenerate orbitals, with wave functions pointing to the negatively charged O^{2-} ions ($d_{x^2-y^2}$ and $d_{z^2-r^2}$) known as the e_g orbitals and also into three-fold degenerate orbitals, with wave functions pointing between the O^{2-} ions (d_{xy}, d_{yz} and d_{zx}), called the t_{2g} orbitals. The possible electronic configurations of these orbitals provide a material with the orbital degree of freedom (*11*, *12*).

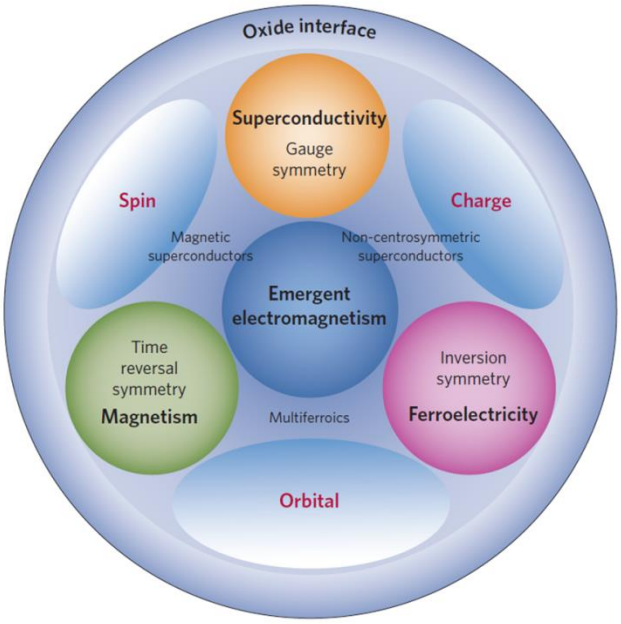

Figure 1.2: Diagram exhibiting the symmetries and degrees of freedom of SCE that can be tailored at oxide interfaces. Adapted from ref. (*3*)

The physical properties of TMO interfaces are usually conditioned by reconstructions of the charge, spin and orbital states at the atomic scale (Figure 1.2). In 2002 Ohtomo et al. (*13*) found a redistribution of the charge in a heterostructure composed of the band insulator $SrTiO_3$ (STO) and the Mott insulator $LaTiO_3$ (LTO). In this system, titanium atoms have different *3d* band occupancies in each of the materials, $3d^2$ for STO and $3d^3$ in LTO. Hence, a rearrangement of interfacial charge occurs, with electrons leaking from the LTO to the STO. This phenomenon results in metallic conductivity even though the system is composed of two insulators. The symmetry breaking at interfaces may result in even more unexpected physical states. For example, the discovery of a superconducting two-dimensional electron gas at the interface between two wide-gap insulators ($LaAlO_3$ and $SrTiO_3$) (*14*) has generated a great interest in the last years. This interface is an archetype of the "polar catastrophe" effect. Along the (001) direction, $SrTiO_3$ is a stacking of nominally neutral $(SrO)^0$ and $(TiO_2)^0$ planes while $LaAlO_3$ is composed of

nominally charged $(LaO)^+$ and $(AlO_2)^-$ planes. Therefore a polar discontinuity will always occur at a sharp interface. In order to avoid the diverging electrostatic energy, half an electron per two-dimensional unit cell is transferred from the $LaAlO_3$ to the $SrTiO_3$. This electronic reconstruction results in a doping of the Ti atoms, producing a conducting interfacial sheet and providing a promising scenario for future electronic applications. Spin and orbital reconstructions can also be produced in complex oxide heterostructures by the epitaxial strain resulting from the mismatch of the lattice parameters of the constituent materials. For example, tensile or compressive strain can induce Jahn-Teller distortions, where the orbital degeneracy is removed by favoring the in-plane ($d_{x^2-y^2}$) or out-of-plane ($d_{z^2-r^2}$) *d* orbitals (*15*, *16*). Moreover, large epitaxial mismatches in oxide heterostructures can produce strong distortions in the lattice that affect greatly the properties of the system. This is the case of the superlattices between $SrTiO_3$ and the ionic conductor ZrO_2:Y_2O_3 (YSZ), with a 7% epitaxial mismatch. The epitaxial strain produces an extreme disorder of the oxygen sublattice in the ultrathin YSZ layers, increasing several orders of magnitude the ionic conductivity of the material (*17*).

Aberration corrected STEM-EELS

The properties of most of the aforementioned systems rely on the presence of small active regions (be it defects or the interface itself) which must be studied by real space techniques. In this context, the evolution of STEM-EELS since the development of the aberration corrector (*18–21*) has brought these techniques to the forefront of material science research. The spatial resolution limits have been pushed down to the half-an-Ångstrom frontier (*22–24*) and we are now capable of analyzing single atoms within a crystal (*25*). In addition, recent advances in monochromated electron microscopes (*26*, *27*) bring new exciting possibilities to the field. One of the advantages of using STEM-EELS is the possibility of studying multiple signals simultaneously. Electrons that have suffered scattering events after interacting with the nucleus of the atoms can be recorded by different means. Annular shaped detectors can give different types of images with complementary information, such as Z-contrast or annular bright field, depending on the detection geometry. The crystalline structure, epitaxial strain or distortions in the lattice produced by defects such as oxygen vacancies or collective phenomena can now be

studied with an unprecedented level of detail. At the same time, when electrons pass through the sample, some of them are dispersed inelastically, loosing part of their initial energy (*28*). This signal can be collected in the EEL spectrometer and provides information about the chemical and electronic properties of the material. We can use the EELS signal to map the elements in our system or study the details of the local electronic band structure. Therefore, the combination of STEM and EELS constitutes a very powerful tool for the study of TMOs. Furthermore, when the dimensions of the system are reduced to a few nanometers (as in an interface) STEM-EELS may be the only approach. In these cases, macroscopically averaged techniques may not provide the necessary information and the spatial resolution of the aberration corrected electron microscope supposes a great advantage. Studies of novel physical effects in interfaces, such as the confined 2D electron gas at the $LaAlO_3/SrTiO_3$ interface (*14*) or the colossal ionic conductivity in epitaxial $ZrO_2{:}Y_2O_3/SrTiO_3$ heterostructures (*17*), have benefited greatly from these developments.

Motivation and aims of this thesis

The main objective of this work is precisely, to unveil mechanisms underlying novel macroscopic behaviors in complex oxide heterostructures and establish a bridge between the atomic and macroscopic worlds. For this aim, we will exploit the power of the analytical capabilities of state-of-the-art aberration corrected STEM-EELS, studying fluctuations just within the sensitivity limits of these techniques. In the first two experimental chapters we analyze the presence and effects of point defects. In particular, we discuss electronic reconstructions caused by oxygen vacancies in complex oxides. Next we approach the problem of ionic conductivity blocking in polycrystalline materials by studying how the presence of intrinsic structural oxygen vacancies within a grain boundary gives rise to an electrostatic barrier. In the following chapters we shift gears towards subtle structural effects and measure how minor lattice distortions may result in dramatic responses due to long range electronic reconstructions in heterostructures composed of different TMOs. We study the relationship between collective phenomena such as magnetism or ferroelectricity with structural deformations of the BO_6 oxygen octahedra and epitaxial strain. Furthermore, we investigate the emergence of novel

interfacial states that can give rise to unexpected phenomena such as quantum resonant tunneling in multiferroic tunnel junctions.

Thesis outline

With these objectives in mind, the results in this thesis are organized in chapters which start with an introduction expressing the motivation and objectives of the experiment and are closed with a brief discussion of the most relevant findings:

- Chapter 2 is dedicated to the description of the experimental techniques used during this work. An extensive introduction to the components and mechanics of the aberration corrected electron microscope is given, along with a description of the data analysis techniques used to obtain the results presented in this thesis.

- Chapter 3: here we give two examples on the effect of irradiation on complex titanium oxides. Using the electron microscope we show how we can controllably modify the surface of these materials and even create new phases with physical properties different from the parent compound.

- Chapter 4: polycrystalline materials are of great importance in energy related applications, where ceramics such as yttria stabilized zirconia are used as electrolytes in solid oxide fuel cells. In this chapter we take advantage of the atomic resolution analysis possibilities of STEM-EELS to study the origins of ionic conductivity blocking in grain boundaries.

- Chapter 5: charge transfer effects in interfaces between different complex oxide materials such as the Mott insulator $LaMnO_3$ and the band insulator $SrTiO_3$ have been reported in recent studies (*29*). Here we show how differences in epitaxial strain and structural distortions in the form of oxygen octahedral rotations are related to the transport and magnetic properties of superlattices with different thickness ratios.

- Chapter 6: In this chapter we show how a charged domain wall is formed in an ultra-thin ferroelectric layer used as a barrier for a multiferroic tunnel junction. The confined charge provides empty electronic states within the insulating tunneling barrier that give rise to a resonant tunneling transport effect in the multiferroic heterostructure.

Finally, chapter 7 summarizes the main conclusions of this work. We also attach an annex including the list publications resulting from this thesis, along with other relevant information such as conference contributions and short stays in international research centers.

Chapter 2: Experimental methods

In this work we have investigated diverse complex oxide materials by advanced electron microscopy techniques, such as scanning transmission electron microscopy and electron energy loss spectroscopy. These techniques allow the simultaneous exploration of structure, chemistry and electronic properties of these systems in real space and with atomic resolution. This chapter gives an overview of the actual techniques used in detail. We explain the basis of scanning transmission electron microscopy, the different components of the microscope and the theory behind aberration correctors. We also describe in detail the operation of the electron energy loss spectrometer and the analysis techniques used to obtain the results presented in this thesis.

Scanning Transmission Electron Microscopy

In a scanning transmission electron microscope (STEM), an electron beam is focused into a small probe and scanned over a thin specimen. The electrons interact with the atoms in the sample as they pass through it, undergoing diffraction and scattering events. These scattering events produce electrons that go out of the sample with different angles and can be measured in different imaging and analytical detectors at the same time, providing different signals and complementary information. The first STEM was designed and constructed by Manfred von Ardenne in 1937-1938 (*30*, *31*) and it had a resolution of 40 nm in the scan direction. The electron probe in modern aberration corrected STEMs can be smaller than one Ångström (*21*, *22*), and this characteristic has made the technique a very powerful tool to study the structural, electronic and compositional properties of materials, down to the atomic scale (*9*).

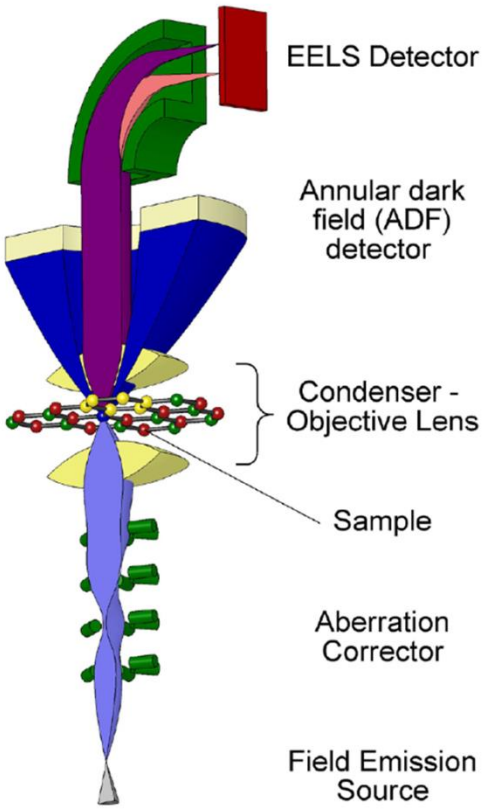

Figure 2.1: Schematic showing the different components of an aberration corrected electron microscope. Adapted from the Nion UltraSTEM User Manual.

The electron probe is a demagnified image of the source and hence, to obtain high spatial resolution, a small source is needed. To form the electron beam, electrons have to be extracted from the source and this process can be achieved in different ways. In thermionic sources, electrons are extracted heating the tungsten or LaB_6 filament whereas in field emission sources, a high voltage is used to extract the electrons. The field emission guns (FEG) operate on the basis that the strength of an electric field is greatly increased at a sharp point (*32*). This way, using a very fine needle, or tip as a source and applying a strong extraction voltage, the work-function barrier is lowered enough for electrons to tunnel out of the material. For the field emission process to occur the surface of the tip needs to be clean of contaminants and hence, an ultra-high vacuum environment is needed for the operation. In this case, the filament is maintained at room temperature and the source is called a cold FEG (cFEG). Furthermore, cFEGs have an overall better performance than thermionic sources, with higher brightness, smaller source size and lower energy spread. A second voltage is applied to the electrons extracted from the tip, called the acceleration voltage, which accelerates the electrons to the desired energy and controls the effective source size and position producing a crossover. After the gun, a set of condenser lenses form a demagnified image of the source that is scanned over the sample using the scan coils, two layers of fast deflectors that produce a shift of the beam and then, bring the beam back to the parallel with the optic axis. The final step in the formation of the electron probe is done by the objective lens that produces the largest demagnification of the probe.

The spatial resolution in the microscope is in principle, determined by the energy of the electrons as dictated by the de Broglie equation (*32*). However, in modern electron microscopes the resolution is actually limited by the optics aberrations of the magnetic lenses that compose the microscope (*33*). This problem has been partially solved with the introduction of aberration correcting lenses inside the microscope column (*21*). A perfect lens would form a focused spot with all the rays that come from the same spot. However, in reality the lenses focus the rays differently because of aberrations. Rays coming in at different angles, positions or energy will be focused with varying strengths. Aberrations are the difference in the optical path length between the real wave front and the perfect sphere. For STEM, the off-axis aberrations can be neglected as the electron probe is really small and there is nearly no difference in the position of the incoming rays. Lens

aberrations are classified in two categories, geometric aberrations due to errors in the optical path lengths and chromatic aberration due to a spread of the beam energy. The chromatic aberration (energy dependence) can be treated separately as the energy dispersion is really small when using cFEG, although it can be reduced further more using a monochromator (*26*).

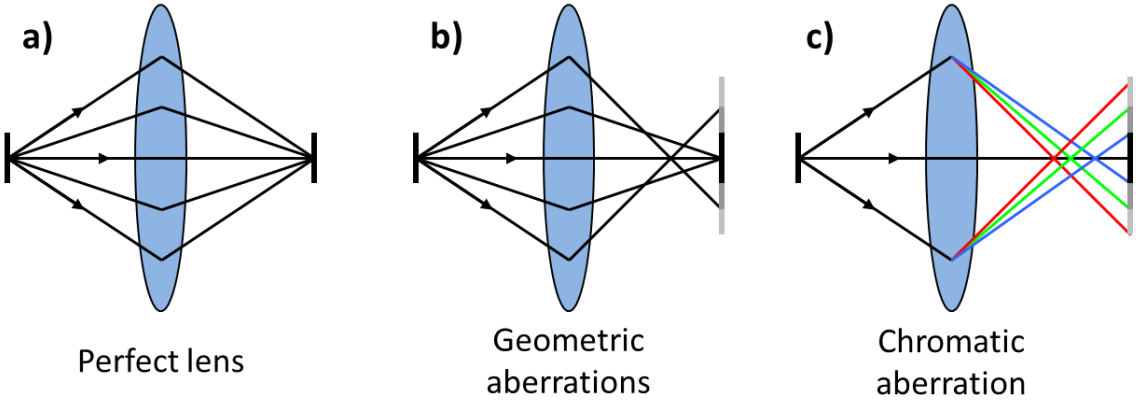

Figure 2.2: (a) Ray diagram for an ideal lens with no aberrations. (b) Diagram showing the effect of spherical aberration. (c) Diagram showing the effect of the chromatic aberration. Adapted from ref. (*34*)

Assuming that the geometric aberration function depends only upon the angle of a particular ray with the optic axis, aberrations in the electron microscope can be expressed as a mathematical expression (*21*, *35*):

$$\chi(\theta) = \frac{1}{2}C_1\theta^2 + \frac{1}{4}C_3\theta^4 + \frac{1}{6}C_5\theta^6 + \frac{1}{8}C_7\theta^8 + \cdots$$

This expression is a power series in function of the angle from the optic axis (θ), the subscript N of each term indicates the order of the aberration, which reveals how rapidly the aberration increases off-axis. The lower order terms predominate in the aberration function as θ is really small. This first order terms are the defocus and astigmatism, which can be corrected easily even in non-corrected electron microscopes. Spherical aberration, C_3 or C_S, expresses the angular dependence in the effect of the lens on the electron beam, rays propagating at different angles, are focused in different points. This aberration can be reduced by introducing an aperture that limits the range of angles at which the rays reach the lens. However, with the use of a small aperture one has to consider diffraction effects

that could also limit the resolution. The optimum aperture allows one wavelength of third-order spherical aberration at its perimeter (*19*, *36*), and is given by:

$$\alpha_{opt} = \left(\frac{4\lambda}{C_S}\right)^{1/4}$$

In 1936, Scherzer (*18*) showed how this aberrations were impossible to correct with conventional magnetic lenses with rotational symmetry, but later, he proposed how to pass this limitation, breaking the rotational symmetry of the system (*19*). In the late nineties, thanks to the advances in technology and computing power, spherical aberration correctors were developed for the electron microscope. There were two different approaches, depending on the symmetry of the multipoles used: Haider et al. achieved the correction of aberrations in a TEM using a hexapole corrector in 1998 (*20*) and Krivanek et al. used a cuadropole/octupole geometry to correct the aberrations in a STEM in 1999 (*21*). In both cases, the multipole magnetic lenses produce a magnetic field that changes with the distance to the optic axis, equal as the spherical aberration does, and hence, after measuring the aberration coefficients, the corrector produces a field that counteracts the aberration.

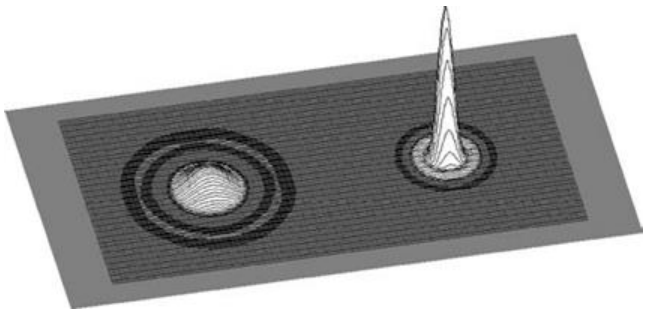

Figure 2.3: Electron beam intensity calculated before and after aberration correction with parameters based on the VG Microscopes HB603 STEM at ORNL, using an acceleration voltage of 300KV and an energy dispersion of 0,3 eV. Adapted from ref. (*34*)

Figure 2.3 shows the effect of the aberration correctors in the electron beam for the HB603U STEM at Oak Ridge National Laboratory (ORNL). Before the correction, the full width at half maximum (FWHM) was 0.12 nm and after the correction, it decreases to FWHM = 0,05 nm, meaning that the electron probe is thinner and much intense after aberration correction. This improvement allows a better spatial resolution and more

sensitivity to individual atoms (*25*). The development of aberration correctors has continued in the recent years and now is possible to correct aberrations up to the 5th order (*22*) and resolutions under 0.5 Å have been achieved at 300kV (*23*, *24*). The aberration correctors have also helped to achieve atomic resolutions at lower voltages and even study single atoms at 60kV (*37*, *38*) or 30kV (*39*).

The post-sample optics consist of an objective lens that collects the electrons scattered at the sample and conduce them back parallel to the optic axis and the projector lenses. Together, these lenses make sure that the different signals enter the various detectors at the proper angles for any given detection mode as shown in Figure 2.4.

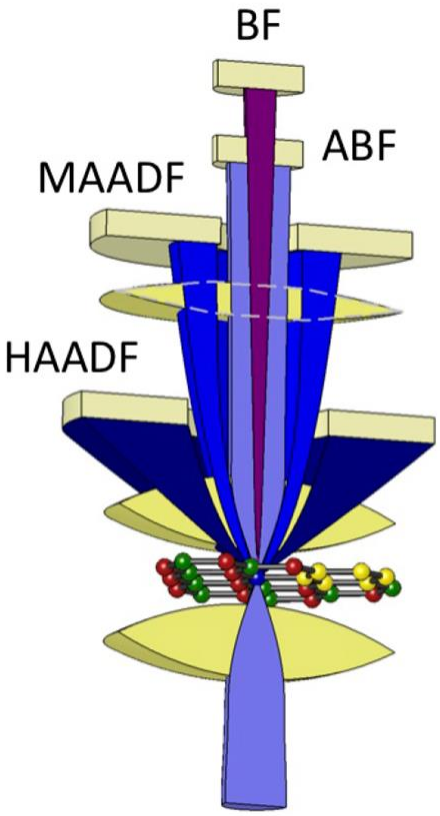

Figure 2.4: Schematic showing a few different possible imaging detectors in a scanning transmission electron microscope. Adapted from the Nion UltraSTEM User Manual.

The principal imaging modes in a STEM are the annular dark field (ADF) and bright field (BF) imaging (*34*). The ADF detector collects electrons scattered to high angles (50-100 mrad) excluding the first-order diffracted beams (*34*). These elastic high angle scattering processes are produced when the electrons pass close to the atomic nucleus

(usually within 0.3 Å). The scattering angle per atom is approximately quadratically proportional to the atomic number, Z, as dictated by Rutherford equation. Hence, ADF imaging is usually referred as Z-contrast imaging (*40*). The ADF signal is largely incoherent, with independent contributions from all the atoms. Atomic columns in the image appear bright on a dark background. This fact implies that the interpretation of the ADF images is very straightforward: intense spots in the image correspond to atomic columns, and the brighter these spots, the heavier the atoms are (*41*). Hence, this technique allows the study of the structural and chemical properties of a material with atomic resolution (*25*). Depending on the detector angles, there can be medium angle ADF (MAADF) or a high angle ADF (HAADF), with a collection angular range from 100 to 200 mrad (*42*). With higher angles the dependence of the intensity with Z increases as the signal from lower angles is reduced.

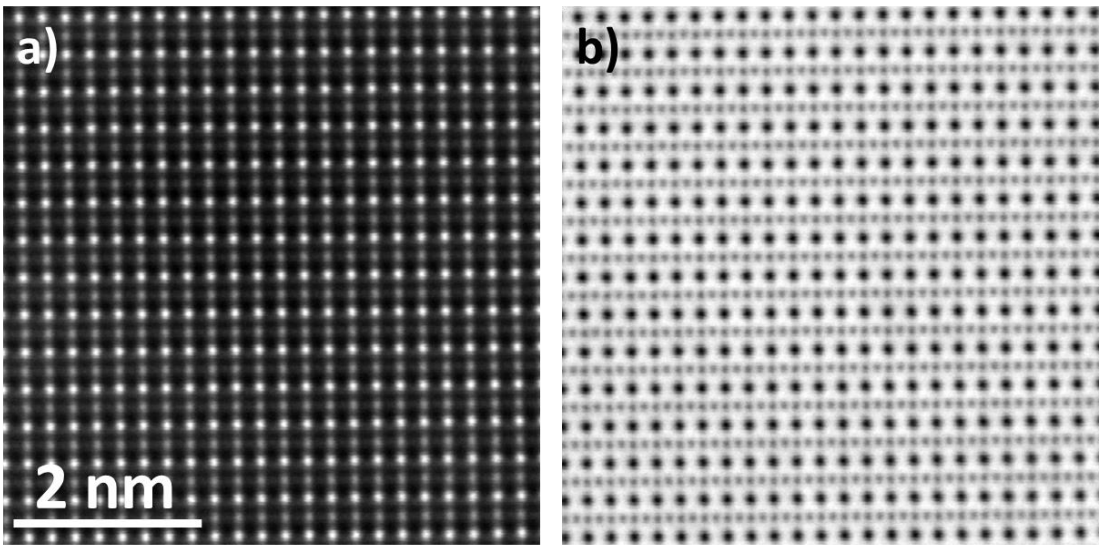

Figure 2.5: Simultaneously acquired HAADF (a) and ABF (b) images of $SrTiO_3$ down the (110) projection obtained with a Nion UltraSTEM 200 operated at 200kV.

Other detectors commonly available are the bright field and annular bright field (ABF). These detectors produce images similar to the conventional high resolution transmission electron microscopes. The image is form with the "bright field disk", the illumination cone incident on the sample. Typically, atomic columns in BF images appear as dark spots sitting on a bright background. This effect is produced when an atomic column has deflected the incident electrons to locations other than where the detector sits. The BF image is coherent, which means that the contrast depends on the relative phase of

the scattered and unscattered electron waves. The image can change from dark to bright if the interference changes from destructive to constructive. The phase also varies with defocus, sample thickness or sample orientation. These aspects make the interpretation of bright field images harder. Very often simulations are required.

The ABF detector, which has been introduced recently (*43*) is an annular detector with an inner angle of 10 mrad and an outer angle of 20 mrad approximately, that is used in STEM mode to produce images with a contrast similar to BF ones. However, ABF imaging is less sensitive to thickness or defocus changes (*44*). This detector has been widely used to image light atoms as oxygen and even hydrogen, which has been imaged using this technique recently (*45*). This detector is more sensitive to lighter atoms because the signal from high Z atoms goes mostly to higher angles and it is not collected in the detector (*46*). Figure 2.5 exhibits an example of simultaneously acquired HAADF and ABF images of $SrTiO_3$ down the (110) orientation. These images were obtained averaging a multiple-shot image sequence that is aligned by means of a cross-correlation process (*47*). The development of newer detectors for the electron microscope is a very promising field of study, and with the advances in technology new types and geometries of detectors will be possible such as pixelated (*48*) or segmented (*49*) detectors.

Electron energy-loss spectroscopy

When electrons pass through the sample and interact with the atoms some of them are dispersed inelastically, transferring part of their energy to the sample (*28*). Some of these processes can be understood as the excitation of a single core electron to a higher energy orbital. The incident electron loses a given energy depending on the energy difference between the two levels. The transmitted beam can be focalized after travelling down the column into the EEL spectrometer, which has a magnetic prism that deflects the electrons depending on their energy as illustrated in Figure 2.6. The electrons are selected by an entrance aperture and then pass through a drift tube which deflects them by 90° with a magnetic field. Electrons that have undergone inelastic scattering are deflected to larger angles that those which have lost no energy. The EEL spectrum is then formed by a set of magnetic lenses in the dispersion plane, where a CCD camera or a photodiode is placed.

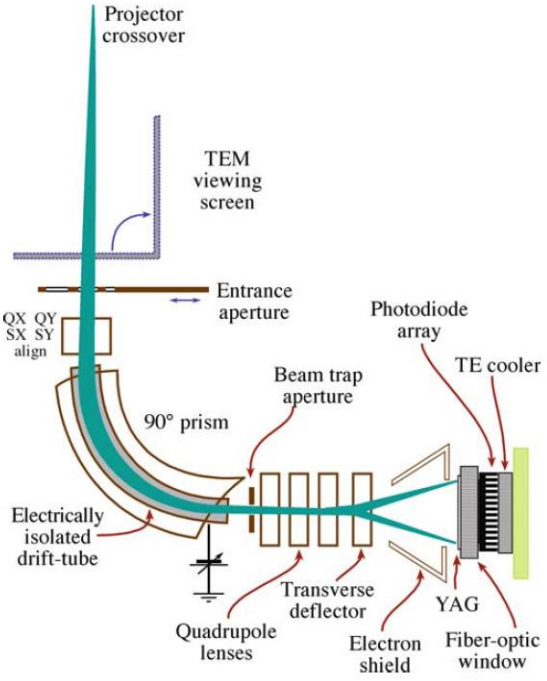

Figure 2.6: Schematic of an EEL spectrometer. Adapted from Williams & Carter (*32*)

The EEL spectrum can be divided in three regions: the zero-loss, low-loss and core-loss as shown in Figure 2.7. The elastic peak (zero loss) gathers the electrons that have been dispersed elastically, without losing energy, and also some of the electrons that have excited phonons, losing too little energy to be resolved by the spectrometer. The width of this peak serves as an indication of the energy resolution in the spectrum which, in theory, should only be limited by the energy dispersion of the electron source. The background present in the EEL spectrum extending from the zero loss tail towards higher energies is created by plural scattering. The intensity of the background is proportional to the sample thickness because the probability of electrons to suffer more than one scattering event (e.g., excite multiple plasmons) increases with sample thickness. It is very important, therefore, that the specimens to be studied are as thin as possible in order to increase the signal-to-noise ratio (SNR) reducing plural scattering.

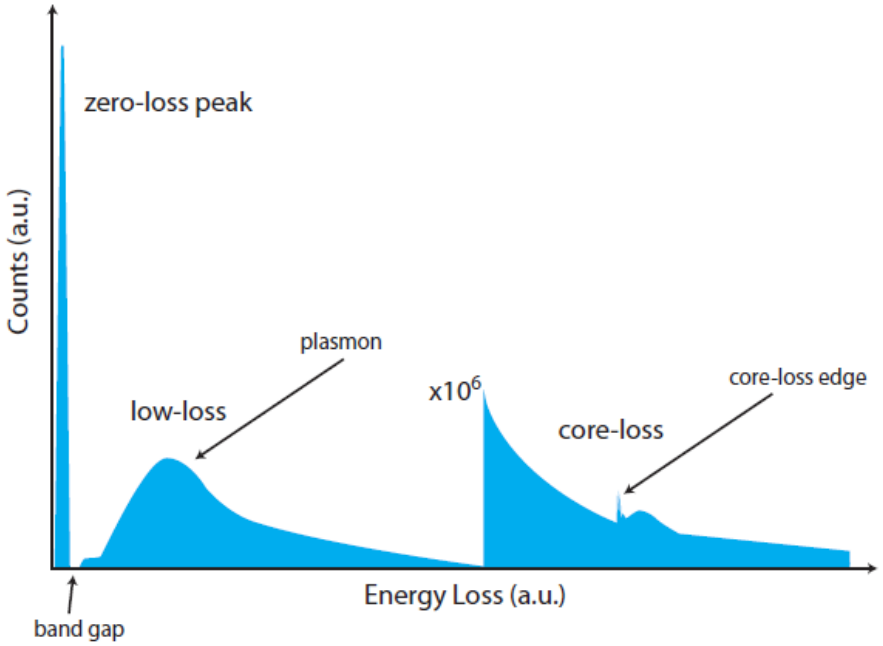

Figure 2.7: Schematic of an EEL spectrum. Adapted from ref. (*50*)

The lowest lying electronic transitions in the material are present in the low-loss region. If the material is an insulator or a semiconductor, the band-gap should be visible in this region. However, usually the width of the zero-loss peak is too large and bang-gap detection becomes a challenging task (*51–55*). The low-loss region also exhibits plasmon excitations produced by the interaction of the electron beam with the sample. In fact, the sample thickness can be estimated from the ratio between the zero-loss peak and the plasmon peaks integrated intensities. Inelastic scattering, due to the interaction of the incident electrons with the outer shells of the atom is visible in the EEL spectrum through a characteristic peak for each element in the range of 5-50 eV (low loss regime, including intraband transitions as well). The interaction with inner shells produces higher energy losses (above 50 eV) that appear in the spectrum as absorption edges (core-loss). These transitions are produced when an electron from the inner shells is excited into unoccupied states above the Fermi level. The edge energy onset corresponds with the ionization threshold which is characteristic of each set of core levels of a particular element, and allows the determination of the elements composing the studied sample. Figure 2.8 shows the characteristic shape of these features. The fine structure of the absorption edges corresponds to the convolution of the core levels with the unoccupied densities of states, modulated by the quantum mechanical rules governing electronic transitions. Each edge gathers all the features coming from transitions with the same principal quantum number

and orbital angular momentum. The analysis of the fine structure provides information about the electronic structure of the material directly from the EEL spectra. This structure is divided in two regions: the lowest energy features from the energy loss near-edge structure (ELNES) are the reflection of the unoccupied density of states and provide information about the local bonding environment such as the coordination and the valence. On the other hand, the higher energy features are called the extended energy loss fine structure (EXELFS) and arise from the effects of plural scattering.

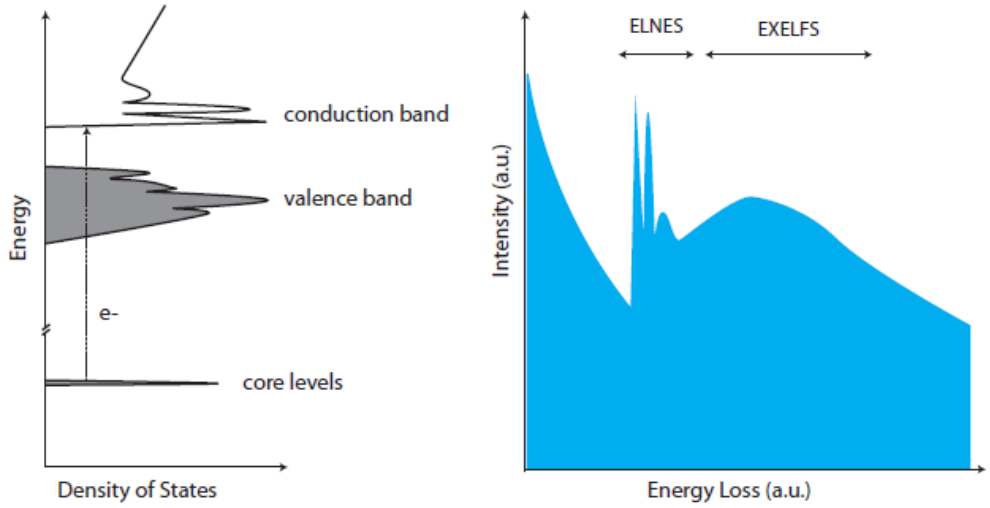

Figure 2.8: Schematic of the ionization edges fine structure demonstrating how EELS reflects the unoccupied density of states with electronic transitions from sharp core loss levels. Occupied states are indicated with gray shading in the density of states plot. Adapted from ref. (*50*)

The EEL spectrometer is capable of producing different types of datasets. A single EEL spectrum can be acquired while the beam is placed on a given position in the sample or while scanning over a region of interest. Such spectra can be averaged achieving high signal to noise ratios. Other measurement method consists on scanning the probe over a region of interest (ROI) which is divided into a network of pixels, and acquiring an EEL spectrum for each pixel. This way a so-called spectrum image (SI) can be acquired (*56*, *57*). Usually, SIs are acquired scanning a rectangular ROI, which creates a three-dimensional datacube of intensity as a function of energy-loss and position I(x,y,E). This technique permits the mapping of the intensity of the spectroscopic features as a function of position in an image, and allows mapping the different atomic species in the sample or even their electronic properties with atomic resolution (*58*). We can, therefore, create

atomic resolution spectrum images (*58–61*) distinguishing the elemental composition of every atomic column as shown in Figure 2.9.

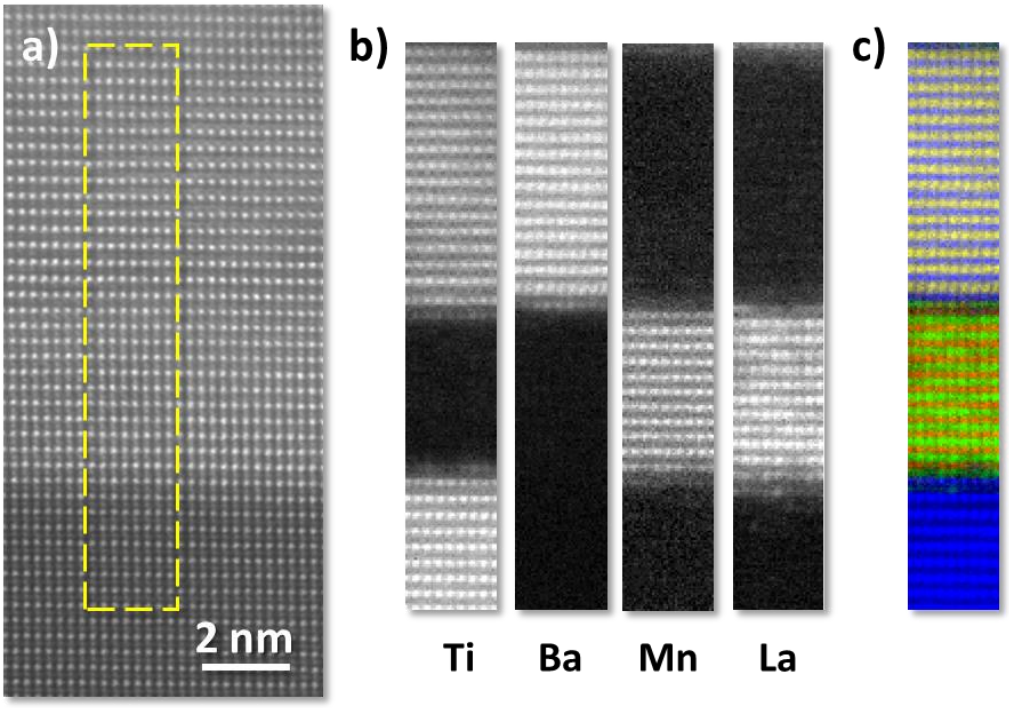

Figure 2.9: Spectrum image of a $La_{0.7}Sr_{0.3}MnO_3$ / $BaTiO_3$ / $La_{0.7}Sr_{0.3}MnO_3$ trilayer grown on top of a (001) STO substrate. a) HAADF image of the region studied. b) Ti $L_{2,3}$, Ba $M_{4,5,}$ Mn $L_{2,3}$ and La $M_{4,5}$ EELS integrated intensity maps. d) RGB color mix image produced by overlaying the Ti (blue), Mn (red), La (green) and Ba (yellow) maps.

Imaging and EELS advanced analysis techniques

In this work several advanced data analysis techniques have been used for both images and EEL spectra acquired with the electron microscope. For example, atomic column positions have been measured in both HAADF and ABF images to study, with high precision, structural distortions such as oxygen octahedral rotations or even ferroelectric polarization. We have also use the *Peak Pairs* analysis (PPA) plug-in for Digital Micrograph (available from HREM Inc.) to analyze strain effects in our samples caused by lattice mismatch between different materials or by extended defects as dislocation cores. By means of EELS, spatially resolved quantitative information has been extracted in order to analyze the chemical and electronic properties of the specimens studied. For this aim, we needed to use advanced analysis techniques such as the

compositional quantification routines in Digital Micrograph or fitting methods as the multiple linear least square fit (MLLS).

Atomic column position mapping

We used a direct atomic position mapping method to analyze structural distortions (*62–64*). In order to do so, we need to reduce the common noise present in the images to be able to measure the atomic column positions in a correct fashion. For this aim, a Fourier filter mask has been used (*65*), such as in the example shown in Figure 2.10. These images belong to a $LaMnO_3$ bulk specimen. This material has a perovskite structure but exhibits an orthorhombic distortion, where the oxygen octahedron is rotated around the three-fold axis. This is visible in the (110) direction as a zig-zag-like relative displacement in between the Mn and O columns in the same atomic plane. In the filtered image (b), the contrast is enhanced. We can use this filtered image to obtain the atomic columns coordinates and quantify the possible distortions.

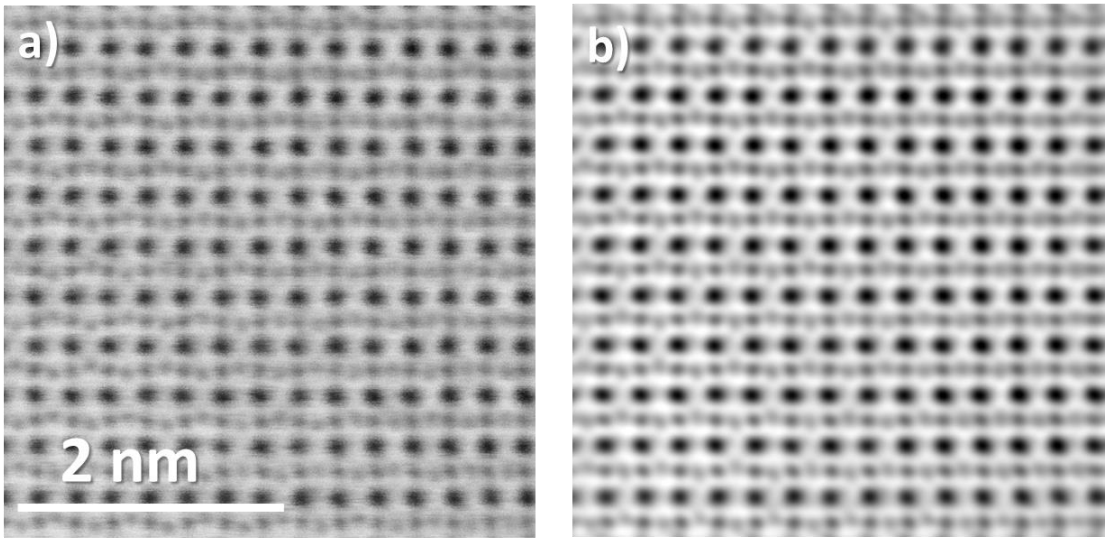

Figure 2.10: a) Raw ABF image of bulk orthorhombic $LaMnO_3$ down the [110] zone axis. b) Image resulting after filtering the image in (a) using a FFT mask.

In order to determine the atomic column positions, we need to invert the contrast of the ABF image because our method looks for the center of the intensity (I) of each atomic column. The method use an initial guess (manual input) of the grid of atomic column positions based on the number of horizontal and vertical unit cells within the

region selected (marked in red in Figure 2.11(a)). After obtaining this initial set of coordinates, the positions are refined in an iterative manner. For each iteration, the center (x_j, y_j) of the intensity (I) for the jth atomic column is calculated as $(x_j, y_j) = (\sum_i I_{ij} x_{ij}, \sum_i I_{ij} y_{ij}) / \sum_i I_{ij}$, where the denominator is the addition of all intensities, and the sums over i include all pixels within a user-defined radius from the center of the previous step. This process gives an estimate of the column position (with sub-pixel accuracy) and, since the intensity is averaged over several pixels, it is less sensitive to noise than taking a single pixel maximum. This procedure is typically iterated for about 20 or more iterations for decreasing pixel radios and the convergence monitored. After the process, atomic columns that were too far from the initial estimate were treated as potentially unreliable. The results are shown in Figure 2.11(b), where we can appreciate the displacement of the oxygen atoms in the Mn-O plane due to the rotation of the oxygen octahedron. Once we have the positions, we can calculate different parameters or distortions within our crystalline structure as will be shown in the following chapters.

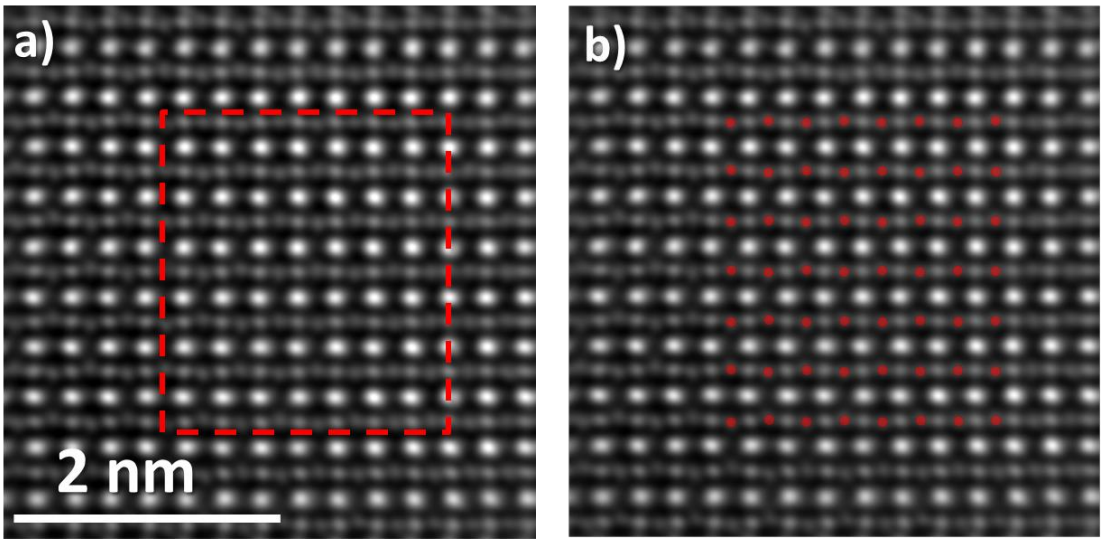

Figure 2.11: a) Inverted filtered ABF image from Figure 2.10b, which has been used to quantify and map the atomic column coordinates. b) Image showing the resulting atomic coordinates for the oxygen columns.

Peak Pairs analysis (PPA)

To study short and long range epitaxial strain effects, such as the ones produced by the different lattice parameters between two different materials or by structural defects, the PPA plug-in for Digital Micrograph has been used (*66*, *67*). This algorithm works in real space and needs a reference lattice from a non-distorted region of the image to calculate the displacement field, which the user defines. First, the procedure locates the local intensity maxima, corresponding to the atomic column positions in the image. For this purpose, we need to use an image filtered in order to reduce the noise and consequently, improve the resolution limit of the technique. The algorithm then uses a 2D interpolation over the image to obtain sub-pixel resolution. After finding the peak positions, we choose two non-collinear basis vectors as the reference for the strain calculations. This procedure can be done either directly on the filtered image or selecting previously two directions in the fast Fourier transformed image. In our example we have selected the first reflections in the (001) and (100) directions to use these vectors as the basis vectors for our strain analysis and also, to extract only the information of the atoms in the A position (Sr, La, Ba) within the ABO_3 perovskite structure (Figure 2.12(b)). The next step consists in the identification of pairs of peaks by looking for the first neighbors of each peak maxima at the distances and in the directions determined by the basis vectors as shown in Figure 2.12(c). Once the pairs of peaks are assigned, the displacements within the material are calculated and a non-distorted region of the image is selected as a reference for the strain calculations. In our example, we have selected as a reference one unit cell of the $SrTiO_3$ substrate, which is the minimal repeating unit in the image. Afterwards, the strain tensor components $(\varepsilon_{xx}, \varepsilon_{yy}, \varepsilon_{xy}, \varepsilon_{yx})$ are obtained at any point in the image resolving the following equations and using a 2D interpolation process:

$$\left.\begin{aligned} u_x &= a_x\varepsilon_{xx} + a_y\varepsilon_{xy} \\ u_y &= a_y\varepsilon_{yy} + a_x\varepsilon_{yx} \\ v_x &= b_x\varepsilon_{xx} + b_y\varepsilon_{xy} \\ v_y &= a_y\varepsilon_{yy} + b_x\varepsilon_{yx} \end{aligned}\right\} \; and \; \varepsilon_{xx} = \frac{\partial u}{\partial x}, \varepsilon_{xy} = \frac{\partial u}{\partial y}, \varepsilon_{yy} = \frac{\partial v}{\partial y}, \varepsilon_{yx} = \frac{\partial v}{\partial x}$$

where (u_x, u_y) and $(v_x, v_y)$are the coordinates of the displacements with respect to the reference base vectors. Figure 2.12(d) exhibits the resulting strain tensor component in the (001) direction using the substrate as a reference. This image shows the difference

between the substrate and the LSMO layer, where the out-of-plane lattice parameter is a 5% smaller than in the $SrTiO_3$. This local real space method has several advantages: the strain around defects can be obtained without the user intervention and the local character of the analysis prevents the propagation of errors around the studied lattice.

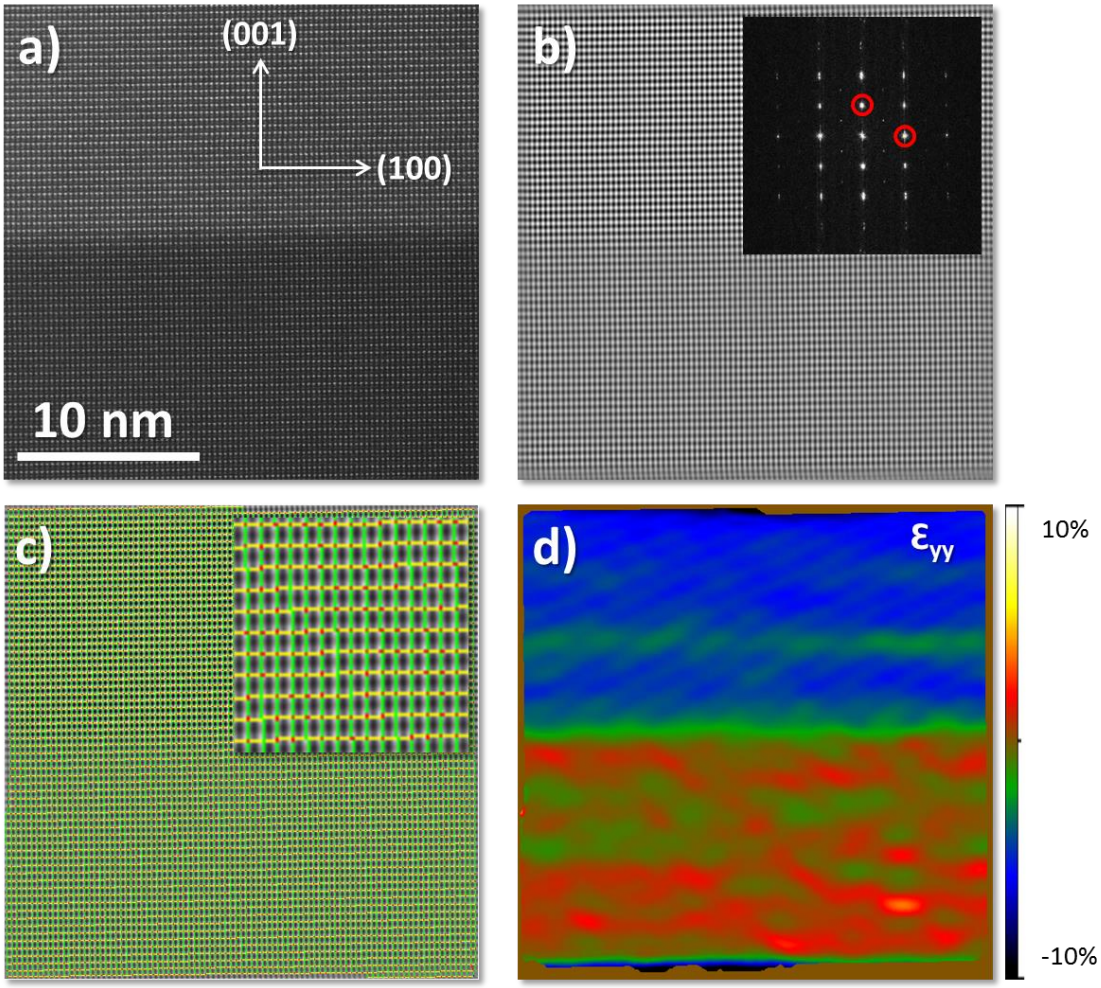

Figure 2.12: a) Original HAADF image of an interface between a $SrTiO_3$ substrate and a $La_{0.7}Sr_{0.3}MnO_3$ thin film, down the [110] zone axis. b) Bragg filtered image obtained using the first two reflections in the (001) and (100) directions as shown in the FFT. c) Peak Pairs image obtained after finding the peak positions. The inset shows a magnified image for better appreciation. d) Strain map of the interface in the (001) direction.

EELS compositional quantification

With EELS it is possible to extract quantitative information about the chemical composition of a material. This capability allows detection of non-stoichiometric areas or chemical segregation in the systems studied. This is possible thanks to the fact that the area under a given ionization edge, I_k, in the spectrum is proportional to the number of atoms of the chemical species per unit area (*28*). Assuming that the electrons contributing to the edge have undergone a single ionization event, the probability, P_k, that a given incident electron will suffer a determined ionization event, k, can be expressed as:

$$P_k = N\sigma_k exp\left(\frac{t}{\lambda_k}\right)$$

where N is the number of atoms per unit area, σ_k is the scattering cross section, t is the specimen thickness and λ_k is the mean free path for ionization losses. This equation assumes that the spectrometer collects the complete angular range $(0 - 4\pi\ sr)$, which is not true. Therefore, we have to modify the equation and if we also assume that the specimen is very thin, we can express the intensity above the background for a determined ionization edge (I_k) as:

$$I_k(\Delta\beta) = N\sigma_k(\Delta\beta)I_T(\Delta\beta)$$

In this equation, I_T is the total transmitted intensity, β is the collection angle, Δ is the integration window and therefore, $\sigma_k(\Delta\beta)$ is the partial ionization cross section. From this equation and if we know how large the investigated volume is and the cross-section of the element of interest, we can determine the absolute number of atoms of a given species. However, in practice, it is usually difficult to know the exact thickness of the specimen and, hence, it is easier to obtain relative concentrations between different species as illustrated in Figure 2.13. For a relative concentration ratio of these two elements, the total transmitted intensity term drops out and the ratio can be written as:

$$\frac{N_A}{N_B} = \frac{I_k^A(\Delta\beta)\sigma_k^B(\Delta\beta)}{I_k^B(\Delta\beta)\sigma_k^A(\Delta\beta)}$$

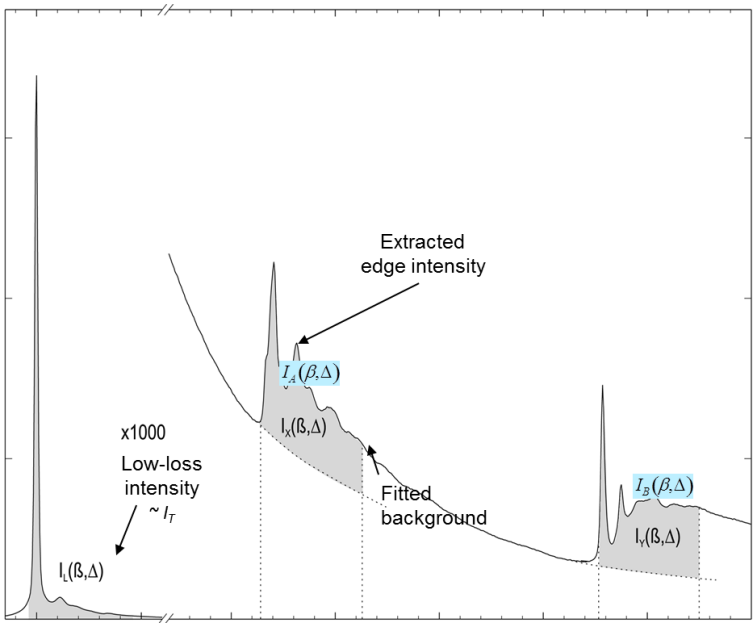

Figure 2.13: Schematic of the EELS quantification showing the low-loss and core-loss regions of the spectrum and the equations to obtain the absolute and the relative concentration of two chemical species in an EEL spectrum.

Multiple linear least-square fitting

The multiple linear least-square fit (MLLS) is a method based on the spatial-difference technique (*68*). This analysis method consists in a fit of the experimental spectrum to two or more reference spectra (*69*, *70*). We can express the experimental EEL spectrum as a linear combination of different components:

$$F(E) = AE^{-r} + B_a S_a(E) + B_b S_b(E) + \ldots$$

where AE^{-r} is the power-law background, $S_a(E)$, $S_b(E)$ ...are the reference spectra and B_a, B_b ... are the scaling coefficients. The fit coefficients obtained with this method give statistical weights associated with each reference spectra. Therefore, these coefficients may be used to quantify changes in the fine structure, separate overlapping edges as shown in Figure 2.14, or even produce better quality elemental maps.

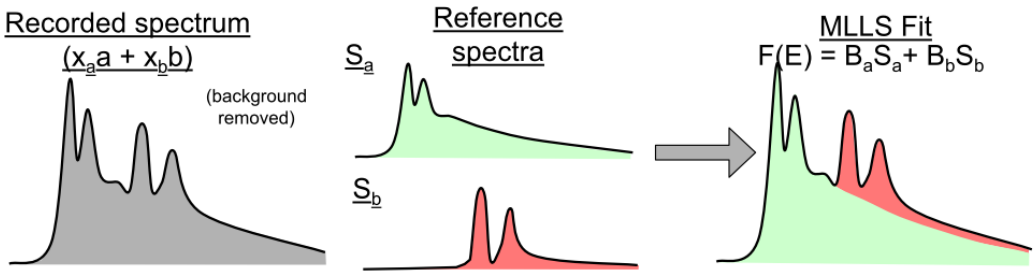

Figure 2.14: Illustration showing how the MLLS fit method can be used to separate overlapping edges. Adapted from the Gatan EELS Imaging and Analysis School materials.

We have used this method to quantify the oxidation states of *3d* metals as titanium. Using reference Ti $L_{2,3}$ edge spectra from well characterized materials where titanium has different valence band occupancies, we can fit our experimental spectrum and obtain the statistical weight for each valence state. For example, for the quantification of the titanium oxidation state in $SrTiO_3$, we have used the reference titanium $L_{2,3}$ edges spectra for $LaTiO_3$ (Ti^{+3}) and $SrTiO_3$ (Ti^{+4}) from the work of J. Garcia-Barriocanal et al. (*29*). We can also use this fitting technique to obtain better quality elemental maps from SIs (*71*). Conventionally, the background removal for core-loss edges is performed using a power law fitting (*28*), where the intensity of the background is given by $I = aE^{-r}$, where E is the energy loss and a and r are fitting constants. This method can be improved, mostly for low energy edges, using a MLLS fitting for the background and the edge signal (*72*, *73*). We use the estimated background and edge signal after background removal obtained with Digital Micrograph as our reference spectra (Figure 2.15). Using this technique, the signal-to-noise ratio for the elemental maps after background subtraction is considerably improved because the background is forced to retain a constant shape for the whole spectrum image. To perform this advanced EELS analysis techniques is important to use data with very high signal to noise ratios and usually, throughout this work, random noise in the EEL spectrum images has been removed using principal-component analysis (*74*).

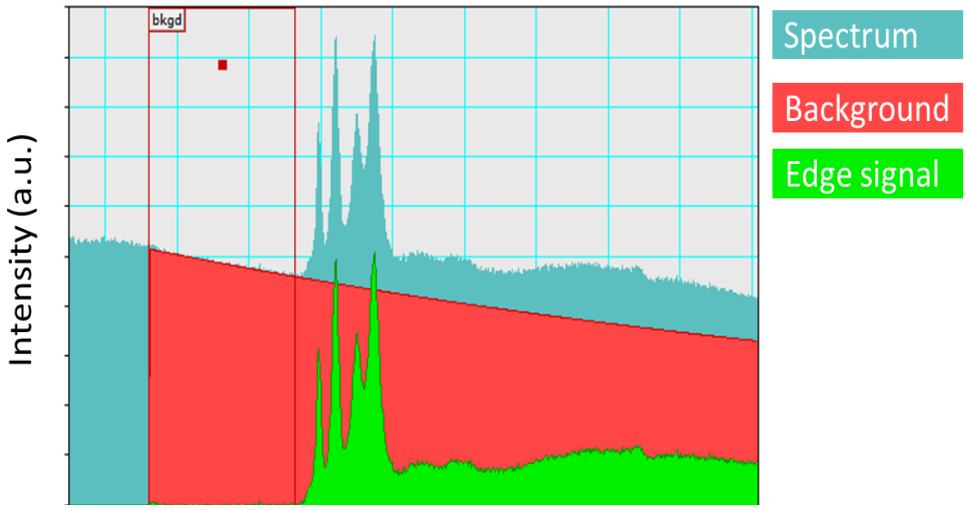

Figure 2.15: estimated background and edge signal after background removal obtained with Digital Micrograph

Principal component analysis (PCA)

As we have seen in this chapter, EELS can be used to extract high resolution information on the compositional and electronic properties of materials. However, not all the information recorded in an EEL spectrum or spectrum image is relevant. And moreover the analysis of the spectral features is not always straightforward due to noise. Thereby, data processing techniques as multivariate statistical analysis (MSA) are often used (*75*). In this thesis we have used the principal component analysis (PCA) routines for Digital Micrograph written by Masashi Watanabe (*74*), which are a useful way of applying MSA to SIs datasets. The purpose of PCA is to reduce the dimensionality of a large dataset to the minimum number of components that describe the original measure without losing any significant information (*76*). PCA decomposes an EEL spectrum image datacube into a two-dimensional matrix, combining the two spatial dimensions in the columns of the data matrix and storing the spectral information in the rows (*75*). Each row of the matrix contains a spectral feature uncorrelated to the other rows, which is called an eigenspectrum. In the other dimension, the columns represent the spatial amplitude of the eigenspectra in the loading matrix. A principal component is hence, the individual product of each row and column. The magnitude of each eigenvalue corresponds to the amount of variance with which the corresponding principal component contributes to the dataset.

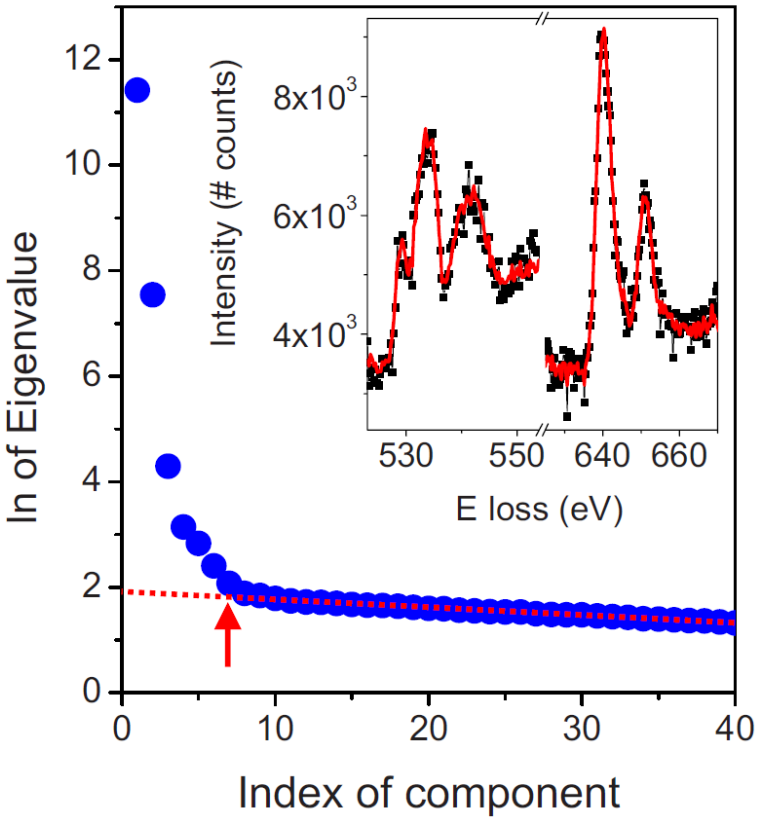

Figure 2.16: Scree plot representing the logarithm of the eigenvalues vs the index of the principal component. A dotted red line highlights the portion of the plot where a flat behavior is observed (characteristic of uncorrelated noise). The red arrow points to the component index (n = 7) where the deviation from this flat behavior is observed. Inset: raw EEL spectrum showing an O *K* edge and a Mn $L_{2,3}$ edge (black dots). The red line is the same spectrum after PCA. Adapted from ref. (*77*).

Typically, the logarithms of the eigenvalues are plotted versus the component number in a scree plot (Figure 2.16). The dominant principal components are closer to the origin and the components containing random noise lie on a straight line at the end. Therefore, experimental noise can be removed in a very reliable way reconstructing the original dataset by selecting the dominant components and discarding the random noise components. The inset in Figure 2.16 shows a comparison between the raw spectrum and the noise reduced spectrum after applying PCA. Nevertheless, PCA should be applied with a great care due to its great sensitivity to artifacts. A high intensity X-ray spike in a single spectrum or a small intensity artifact repeated in several spectra may be recognized as a component. Moreover, other experimental errors such as shifts in the energy, errors in the gain and dark current correction or energy misalignments must be addressed when applying PCA (*78*). Despite these problems, the high sensitivity of PCA and other multivariate analysis techniques makes of them a powerful tool. Slight modulations of the

spectral features with an actual physical meaning can be extracted out of a large SI dataset. For example, various phases in a specimen can be identified displaying the different principal components of the SI (*74*). Moreover, ELNES modulations localized only to an interface between two materials can be found and analyzed (*79*).

Electron Microscopes

We have used three different aberration corrected microscopes during this thesis: the JEOL JEM ARM200CF installed in the "ICTS Centro nacional de microscopía electronica" at Universidad Complutense de Madrid (Spain), and the Nion UltraSTEM100 and UltraSTEM200 both installed at the Oak Ridge National Laboratory, TN, U.S.A.

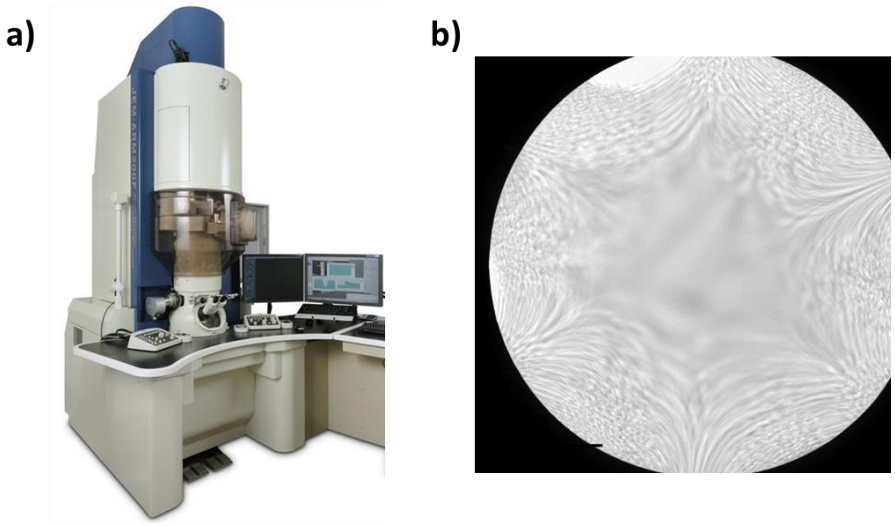

Figure 2.17: a) Photograph of a JEOL JEM ARM200CF. b) Image of a focused aberration corrected ronchigram over an amourphous specimen acquired in a JEOL JEM ARM200CF microscope at ICTS Centro nacional de microscopía electrónica..

The JEOL JEM ARM 200CF electron microscope is equipped with a cFEG capable of working at 80, 100 and 200 KV acceleration voltages and a Gatan Quantum EELS spectrometer. It has a CEOS spherical aberration corrector in the condenser lens with a 6-fold symmetry, as shown in Figure 2.17(b). This microscope is capable of working in both TEM and STEM modes and has the possibility of acquiring ABF images using a beam stopper with an outer radious of 10 mrad on top of the bright field detector.

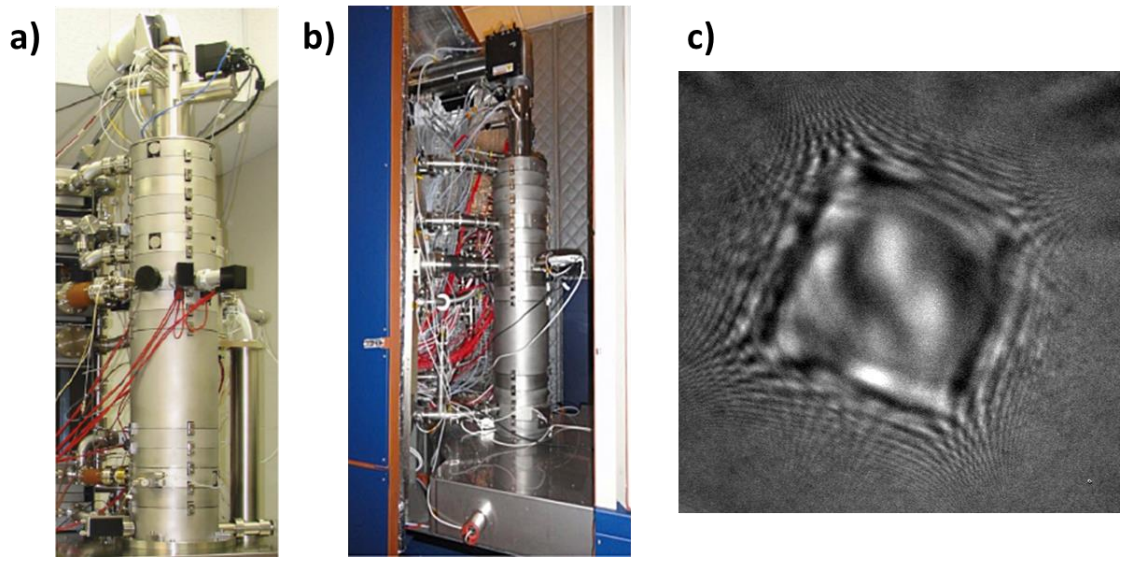

Figure 2.18: a) Photograph of a Nion UltraSTEM 100. b) Photograph of a Nion UltraSTEM 200. c) Image of a focused aberration corrected ronchigram over an amorphous specimen acquired in a VG Microscopes HB603 STEM at ORNL.

The Nion UltraSTEM100 (*80*) uses a cFEG that can operate at 60 and 100 kV acceleration voltages and is equipped with a Gatan Enfina spectrometer. On the other hand, the Nion UltraSTEM200 is equipped with a cFEG that operates at 60, 100 and 200 kV and a Gatan Enfinium spectrometer. This microscope features also a dedicated ABF detector. Both of them are dedicated STEM microscopes equipped with Nion 5th order aberration correctors using a cuadrupole/octupole geometry as shown by the 4-fold symmetry of the focused ronchigram image in Figure 2.18(c).

Sample growth

Most of our samples were grown by high oxygen pressure sputtering deposition within our group, GFMC at UCM (*81*). This method is based on the ballistic impact of atoms against a substrate after being removed from a material source. The sputtered ions come from targets made of the stoichiometric compound while the oxygen plays the role of the sputtering element. In our case, the substrate is placed on a heater plate below the targets. The growth takes place inside a chamber with a high vacuum of about 10^{-6} mbar. Figure 2.19 shows the sputtering chamber. It is connected to a turbo-molecular pump in combination with a membrane pump. A constant oxygen flow is injected and controlled

by a system of needle valves. Since the sputter yield depends on the energy of the incoming oxygen ions and the source atom species, the material removed from the target will deposit on the substrate in a manner which strongly depends on several controllable parameters such as the temperature of the substrate, the applied radio frequency (RF) power and the pressure inside the chamber.

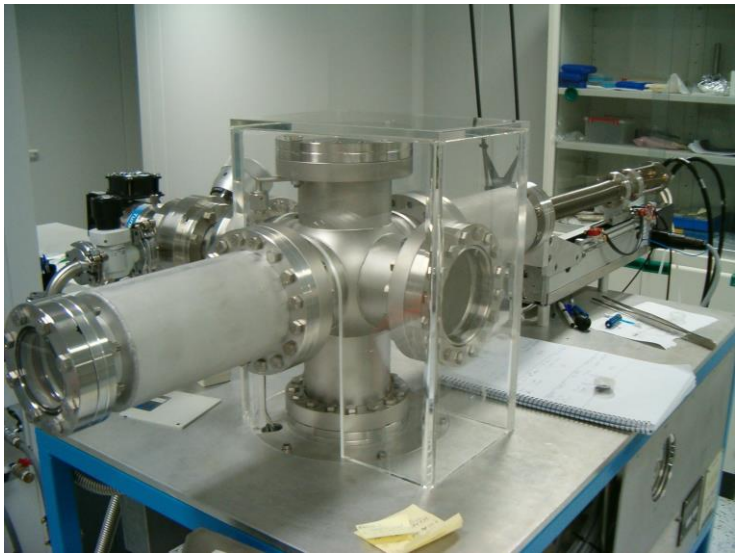

Figure 2.19: View of the sputtering chamber. The targets are mounted on a remote controlled arm to switch between the different materials.

High temperature and pressure are required in order to grow epitaxial oxide heterostructures. Most samples studied in this work have been grown on $SrTiO_3$ (100) substrates. The high oxygen pressure (2-3 mbar) used during the deposition process, favors a complete thermalization of the extracted species and at the same time, prevents them from back-spattering and loss of oxygen in the final crystalline structure. Under these conditions, the material deposition rate is slow and ensures an epitaxial growth of the sample. To preserve the optimal oxygen content of the structure and *in-situ* annealing at 900 mbar oxygen pressure is necessary. The growth conditions depend on the growth material and the substrate.

Specimen preparation

The preparation of high quality specimens for transmission microscopy observation is a critical part of the process. The quality of the specimens affects enormously the results to be obtained. The samples prepared for observation must be undamaged, clean of surface amorphous layers and thin enough in order to measure good, reliable data. Specimens for transmission electron microscopy should be transparent under the electron beam. For this aim, they may have a thickness well below the elastic dispersion mean free path of electrons in the sample's medium, normally around 100 nm. Sample preparation requires special techniques, and it is often a long and tedious process. There are two main possible geometries for TEM sample preparation: planar view, in which the electron beam is orthogonal to the substrate plane; and cross-section, in which the beam is parallel to the substrate plane. In this work, we have mostly used the second method, which is considerably more complex but indispensable for the direct characterization of interfaces and its microstructure. Figure 2.20 shows the different steps of the process:

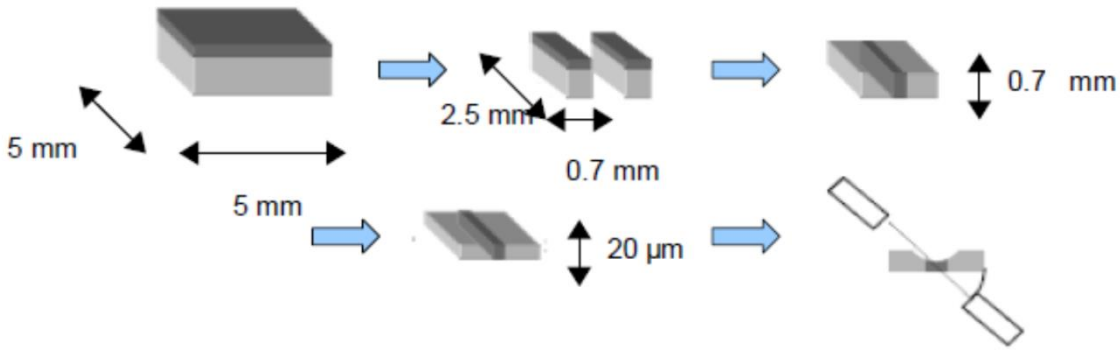

Figure 2.20: Schematic showing the different processes of sample preparation.

1. 5x5x1 mm sized samples are first cut into 0.7 x 2.5 mm pieces approximately. This process is realized with a low speed diamond saw and the pieces must be cleaned in an ultrasound bath with organic solvents.

2. The clean pieces are glued together with an epoxy in order to bring together the treated surfaces of the substrate. The epoxy layer must be thin and cover the whole surface of the substrate. The glued "sandwich" is left in a press at high temperature (150ºC) to cure the resin.

3. The sample is thinned down to 15 microns with a mechanical polishing procedure. First, we polish one side of the sandwich using lapping films with diamond particles of different sizes. Normally, we start with a 30 μm grain film, and then we use several films with decreasing grain size down to a 1 μm size lapping film. This way, we obtain a perfect specular surface in the first side of the sandwich. Then, we measure the thickness of the specimen to have a reference thickness value and we repeat the previous procedure to polish the second side, and thin the sample to approximately 15 μm.

4. The 15 μm specimen is glued to a 3 mm cupper ring, which serves as support.

5. The final thinning of the specimen to electron transparency is performed with a low angle and low voltage ion milling process. The ion mill is equipped with two Ar ion beams that work at 4 or 5 KV voltages and mill the sample until a small hole is made. The edges of this hole are thin enough for TEM observation. After the hole is made, it is advisable to clean the sample by milling it during five more minutes with a lower voltage (0,5 KV) in order to get rid of any deposited amorphous material.

Chapter 3: Irradiation effects on the surface of oxide materials.

In this chapter we turn our attention into the study of relevant materials systems where minor densities of point defects (barely over the detectability threshold) drastically affect the macroscopic properties. We show how new superficial phases can be produced in Ti oxides by low energy ion bombardment. Surface irradiation results in the formation of heavily damaged surface layers which will be studied by atomic resolution Z-contrast images and analyzed by EELS, including depth sensitive studies. These surface treatments can turn an insulating $SrTiO_3$ crystal into a conductor. We discuss the presence of an oxygen vacancy rich area immediately underneath the surface, which results in over population of the Ti *3d* bands and, hence, in the observed metallicity.

Introduction

In the previous years, a vast amount of research has been focused on the study of novel physical effects and functionalities achieved with state-of-the-art fabrication techniques in epitaxial systems. Unexpected results have been reported in oxide interfaces, but the equipment and conditions required to bring this kind of systems into the realm of applications are often very complex and expensive. Therefore, the development of more simple and inexpensive techniques to produce nanostructures with similar functionalities remains a challenge. In this context, there is a growing interest in methods capable of controllably modifying surfaces, such as nanopatterning through irradiation. New phases and nanostructured surfaces have been created by preferential ion-beam etching (*82*, *83*) or ion sputtering treatments (*84–86*) in different materials. In order to harness such processes, probes capable of depth sensitive real space studies of heavily damaged layers with atomic resolution are a must. Combined STEM-EELS analysis is a powerful tool to study both the surface and the bulk of these materials.

In this chapter, we address the effects of Ar^+ ion irradiation on the surface of titanium oxides. In particular, we will focus on explaining the presence of surface metallic states in insulating $SrTiO_3$ (STO) single crystals (*87*). Complex oxide materials, as STO, pose an exciting promise towards the design of electronic devices that could overcome some of the limitations of Si. Recent studies have reported that a 2D surface electron gas can be induced in commercial STO single crystals by Ar^+ plasma irradiation (*82*). This type of irradiation can produce a metallic state with confined 2D transport properties, presumably resulting from oxygen vacancies, generated by ion beam etching (*88–91*). These vacancies provide carriers to the lattice, resulting in an insulator-to-metal phase transition. We will analyze the nature of irradiation effects in STO (discussing also the case of a less complex, binary oxide such as TiO_2 as a reality check) performing a depth dependent compositional analysis of the irradiated layer. Furthermore, the origin of induced surface metallic states will be explained by analyzing the band occupancy of the titanium atoms closer to the surface.

Two paradigmatic titanium oxides: TiO_2 and $SrTiO_3$

Titanium dioxide is a semiconducting material that exhibits different crystalline structures (rutile, anatase and brokite) depending on temperature, doping level or grain size. The most stable configuration is the tetragonal rutile phase with a space group $D_{4h}^{14} - P4_2/mmm$ (*92*). In this phase, TiO_2 has an indirect band gap of 3,05 eV at 300K. The physical properties of rutile depend strongly on the intrinsic defects of the material, consisting mainly on interstitial Ti^{+3} atoms and oxygen vacancies. These defects form donor levels in the TiO_2 gap and produce a n-type semiconductor behavior of the material in normal conditions (*93*, *94*). They are also responsible for the photo-catalytic properties of TiO_2(*95*).

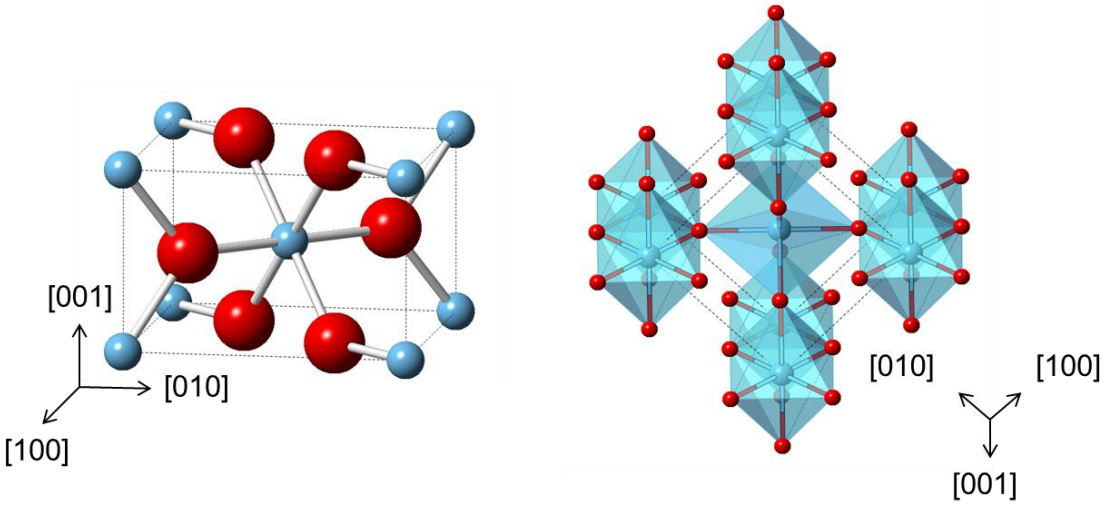

Figure 3.1: Bulk structure of rutile TiO2 with Ti (O) in blue (red). The tetragonal unit cell has the parameters a=b= 4.587 Å, c= 2.953 Å. The stacking of the octahedra is shown on the right.

A more complex oxide, STO, has produced a great interest because of its physical properties and is one of the most widely studied materials for oxide electronics. STO is one of the best candidates to produce heterostructures with other complex oxides. Moreover, the possibility to grow epitaxial STO layers on top of Si substrates (*96*) is an important advantage in the compatibility between devices based on complex oxides and current devices based on Si. STO has a perovskite structure above 106K with a $Pm\bar{3}m$ space group (*97*) and a lattice parameter of 3,905 Å (*98*). In the typical ABO_3 perovskite structure (Figure 3.2), the Sr atoms are positioned at A-sites and Ti atoms at B-sites, leading to a stack of alternating $Sr^{2+}O^{2-}$ and $Ti^{4+}O^{2-}{}_2$ neutral planes. STO has an indirect

band gap of 3.25 eV, which makes it a band insulator and hence, the electronic properties of STO can be easily modulated by doping it with electrons. This can be achieved through substituting La for Sr cations or Nb for Ti atoms, and also by generating O vacancies (*99*). These processes introduce n-type mobile carriers in the STO lattice and reduce some Ti atoms to Ti^{+3}, resulting in a mixed valence system (*100–102*).

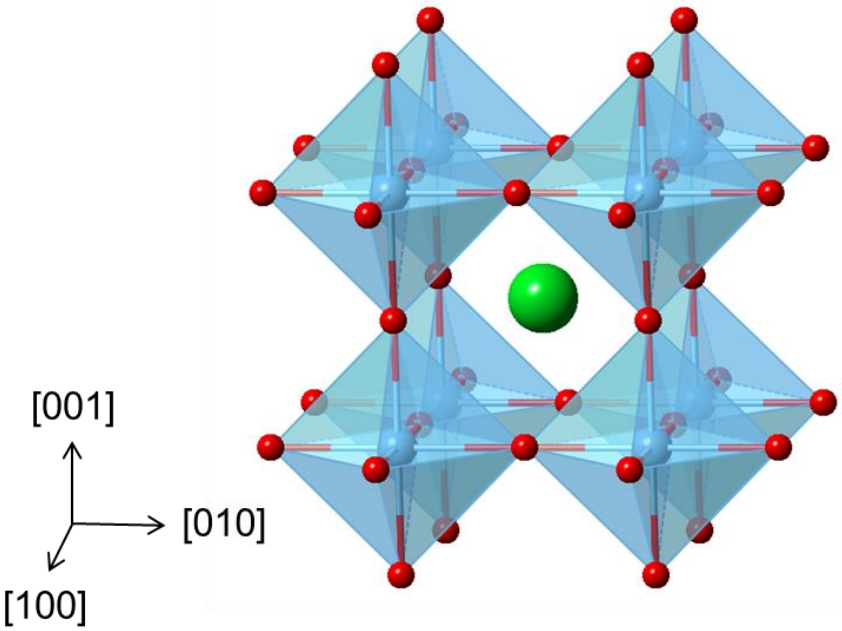

Figure 3.2: Atomic structure of non-reconstructed cubic STO: oxygen atoms (red) surrounding titanium atoms (blue), with strontium atoms (green) outside the octahedron and equidistant from the titanium sites.

Experimental results

Commercial STO single crystals were treated with an ion etching technique. The process consists in the irradiation of the whole sample with an ion plasma in vacuum conditions. The bombardment erodes the surface and may also lead to the implantation of ions producing deformations in the crystalline lattice. The results of the erosion depend on the crystalline direction of the sample subject to the process. This technique may also remove atoms from the specimen surface, process that could be accentuated using chemically reacting gases for the plasma in a technique called reactive ion etching (RIE). For this study, STO (001) single crystals were chemically etched and annealed following the standard recipe to ensure a TiO_2 surface termination (*103*). Samples were irradiated in

an Ar ion milling reactor under a pressure of 2 mTorr and at RF powers between 20 and 40 W for time periods of 5 minutes. The transport measurements were carried out in the van der Paw geometry (*104*) using evaporated Al contacts. *IV* curves were recorded to ensure their Ohmic nature. AFM images were acquired in a Bruker multimode Nanoscope III A, equipped with 1 µm, 15 µm and 150 µm maximum scanning area scanners. The microscopy characterization was carried out in a Nion UltraSTEM100 operated at 100 kV. The specimens were prepared by conventional mechanical grinding and polishing and Ar ion milling.

Transport characterization

STO substrates become conducting after irradiation with RF powers above 25 W. Figure 3.3 shows the temperature dependence of the zero-field sheet resistance of samples irradiated with RF powers between 30 and 40 W. These treated substrates are metallic in the whole measurement range, and a superconducting behavior could be expected for lower temperatures. The resistance decreases as the RF power increases, denoting an enhancement of the irradiation induced damage. A power law behavior characteristic of electron-electron interaction (*105*) is also found below the STO structural transition (*106*) at 105K. Samples become insulating again after a 900 ºC bake in an oxygen atmosphere.

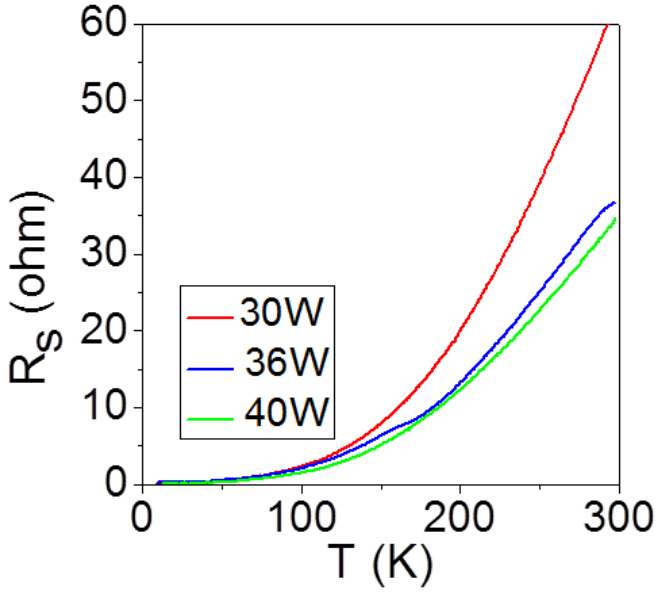

Figure 3.3: Temperature dependence of the sheet resistance of crystals irradiated at RF powers from 30 to 40 W for 5 minutes.

Surface characterization

Atomic force microscopy was used to study the surface of the treated samples in order to characterize the erosion of the STO single crystal surface due to RF irradiation. Before irradiation, well defined, atomically flat terraces are observed (Figure 3.4 (a)). The terraces have 100 nm widths on average. After Ar^+ irradiation, the surface suffers severe damage as denoted by Figure 3.4 (b), (c) and (d), which show the irradiation damage for different RF powers (20W, 36W and 40W respectively). For the lower RF powers, terraces are still observed although their edges are somewhat ragged. Increasing the RF power results in the loss of surface features and enhanced structural damage. For the most damaged samples, the terrace structure typical of the single crystal substrate is lost completely. Incidentally, a gradual change in the color of the samples is also observed. The samples become optically gray as damage increases, as previously observed by Reagor & Butko (*82*).

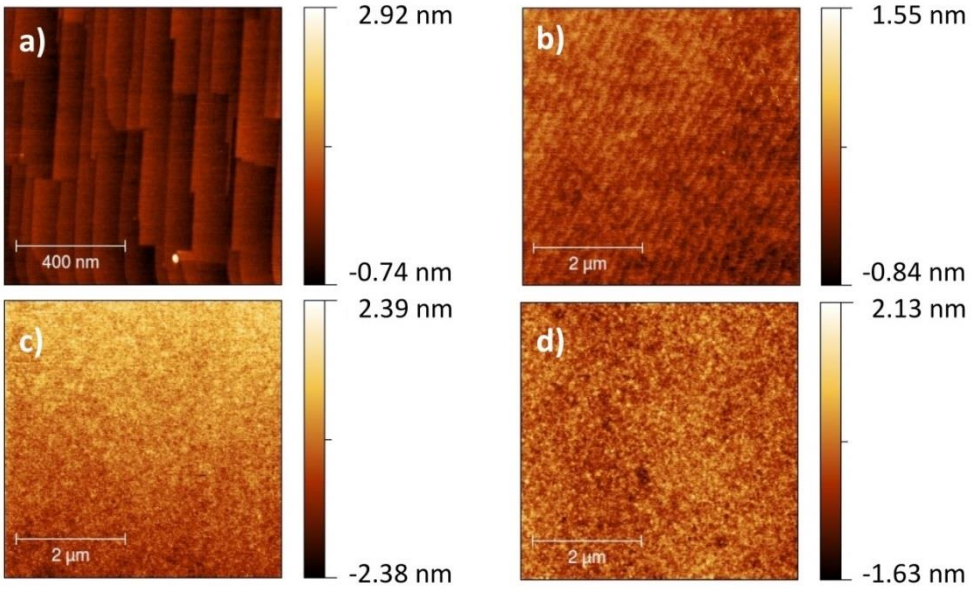

Figure 3.4: AFM images of samples irradiated at different energies: no irradiation (a), 20 W (b), 36 W (c) and 40 W (d).

STEM-EELS characterization

Cross-sectional scanning transmission electron microscopy images in Figure 3.5 show the effects of irradiation at the atomic scale. Simultaneous HAADF and BF images of a sample which was treated in the RIE system at 36W for 5 minutes were acquired in a Nion UltraSTEM 100 aberration-corrected STEM operated at 100KV. The eroded surface layer can be observed clearly. Low magnification images show that this damaged layer is continuous and homogeneous over long lateral distances, of the order of a few microns. The surface region exhibits poor crystalline quality: voids and amorphous areas, down to a depth of 12 nm are present. Such loss of crystalline order is also appreciated in the bright field image in Figure 3.5(d), which is equivalent to conventional high resolution transmission microscopy. Estimated values of the projected damage range of a few nanometers were obtained for the typical 100-200 eV energy range (*107*, *108*) of the irradiation experiments, consistent with our microscopy observations.

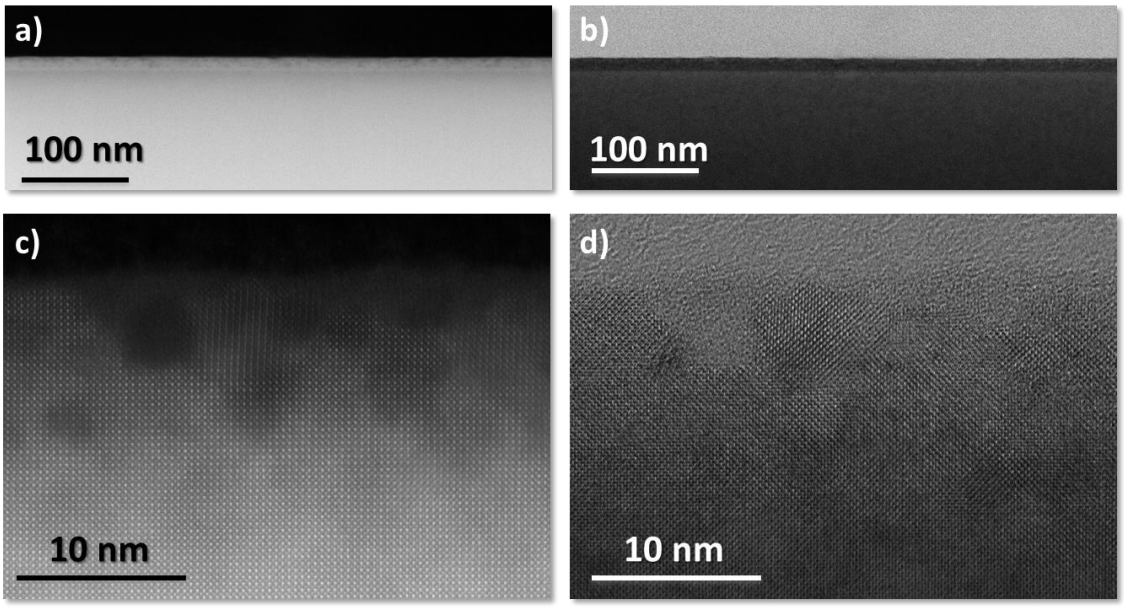

Figure 3.5: STEM images of a sample irradiated at 36 W for 5 minutes. Low magnification HAADF (a) and BF (b) images along with high magnification HAADF (c) and BF (d) images.

We were concerned about the possible damage suffered by the sample during the preparation process, especially in the ion milling step, where the samples are thinned to electron transparency using a low angle and low voltage Ar ion milling process with beams voltages around 4 to 5 KV. To evaluate the possibility of introducing artifacts

resulting from the preparation process, we prepared a STO single crystal without any irradiation treatment using the same process and with the same parameters for the ion milling as the irradiated sample. As Figure 3.6 shows, the non-treated STO single crystal does not display any of the damage features seen in the irradiated specimen, conserving a perfect crystalline structure up to the most superficial atomic planes. Therefore, we can assure that the features observed in Figure 3.5 do not come from the sample preparation process, but from the RF irradiation treatment instead.

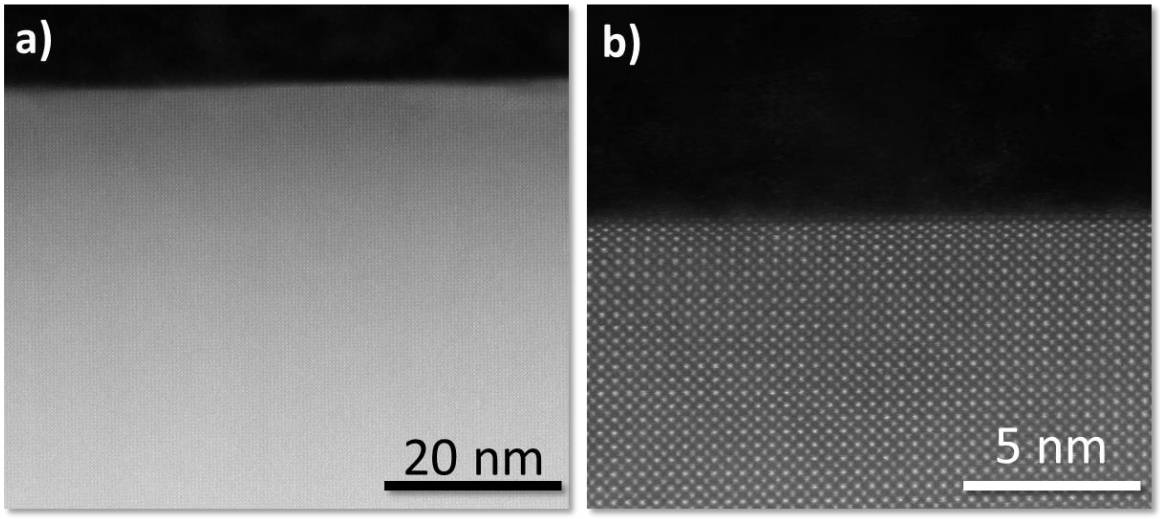

Figure 3.6: Low (a) and high (b) magnification HAADF images of a STO single crystal without the irradiation process. Some spatial drift is observed.

Specimen preparation: damage vs. no damage?

In general, this possibility of damage and/or artifacts actually being induced during preparation is concern that is common to all microscopy, so here we will examine it in detail for a moment. We hope that the discussion will be relevant to the whole work in this thesis. For this aim, we have shifted gears back to a more simple system and irradiated a binary oxide such as rutile TiO_2, where an independent macroscopic characterization that can be used as a reference is available. The irradiated samples were provided by the Surface Science Group at Complutense University. Specimens for microscopy characterization were also prepared with conventional mechanical polishing and Ar ion milling using the cross-section geometry and observed in a JEOL JEMARM 200cF operated at 200 kV. Low magnification HAADF and ABF images in Figure 3.7 show the irradiated layer on the surface of the TiO_2 single crystal. The layer has a

homogeneous thickness of approximately 10 nm and is flat and continuous over long lateral distances. The high magnification images in the [001] orientation show the structure of the irradiated layer and its interface with the crystal. The interface, although not atomically sharp, is flat as depicted in the magnified filtered image in Figure 3.7(c) (yellow dashed line). The bombarded layer exhibits crystallinity with a well-defined orientation relative to the substrate. The fast Fourier transform (FFT) obtained from the whole image in Figure 3.7(c) shows the substrate and the film reflections (marked with yellow arrows), which hint that the crystalline structure of the irradiated layer is different from the substrate. Macroscopically averaged XRD and LEED measurements (*109*) have also detected this phase on the surface of the irradiated substrates before the preparation for the STEM observation. Therefore, any effects observed in these images are not an artifact resulting from sample preparation but actual consequences of the irradiation process.

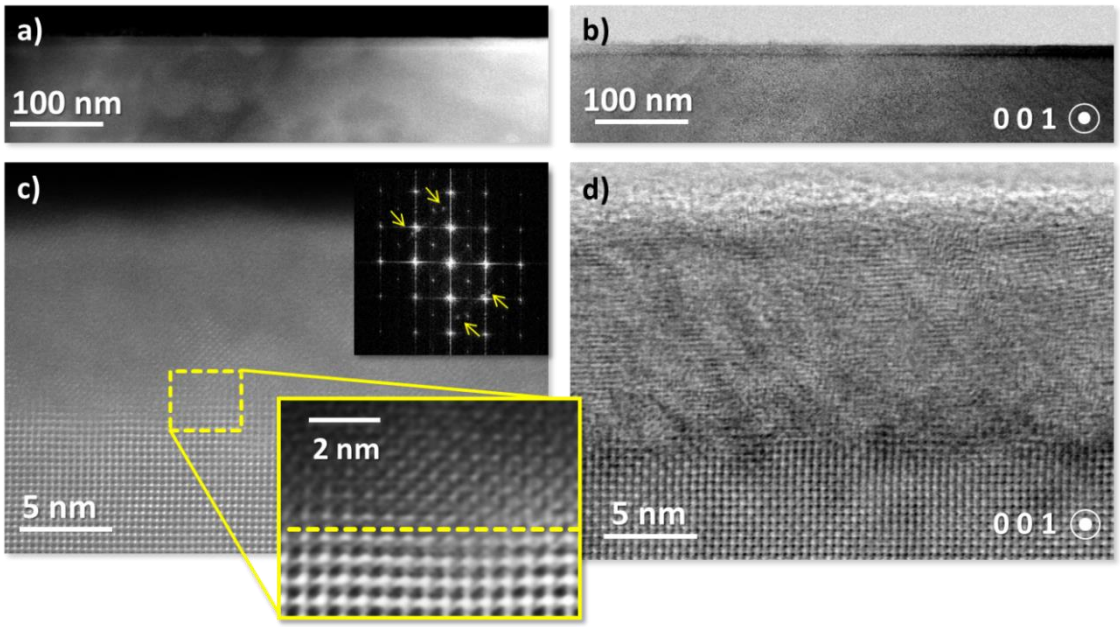

Figure 3.7: HAADF (a) and ABF (b) low magnification images of the irradiated layer down the [0 0 1] direction. High magnification HAADF (c) and ABF (d) images for the same orientation. The lower inset in (c) shows the partially coherent interfaces between the TiO_2 substrate and the irradiated layer. A horizontal dashed yellow line marks the position of the interface. The upper inset in (c) shows the FFT extracted from the whole image. Yellow arrows point at the film reflections. The ABF images were acquired using an inner angle of 11 mrad and an outer angle of 20 mrad.

As for the nature of the surface layer in this case, we have used an EEL spectrum image and the routines explained in the experimental techniques chapter to obtain a

chemical relative quantification of Ti and O. Figure 3.8 shows the results from the quantification analysis. The substrate presents a relative composition (atomic percent) of 66% O and 34% Ti, as expected for TiO_2. The irradiated layer, however, exhibits a strong variation in composition with a reduction of the oxygen concentration to below 60% and a Ti concentration larger than a 40% within 10 nm from the surface, which is consistent with the observations in the HAADF and ABF images. Interestingly, these values are closer to the TiO nominal composition.

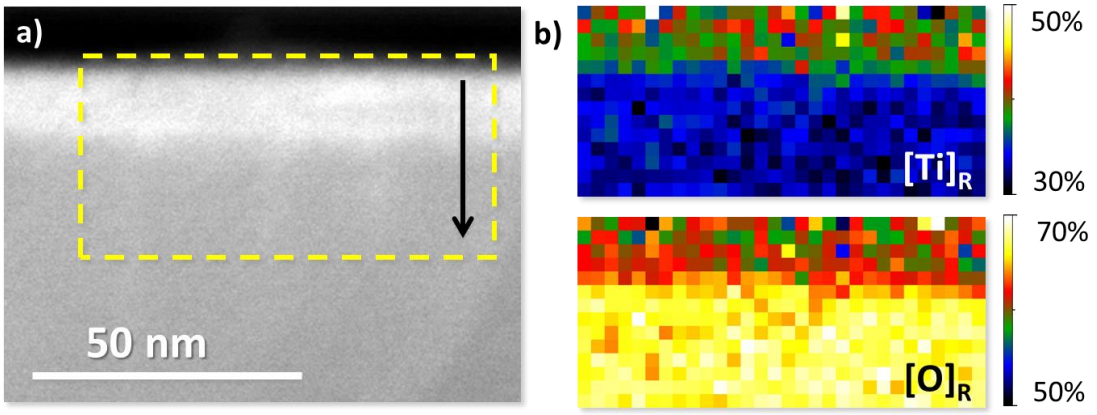

Figure 3.8: Low magnification high angle ADF image of the irradiated layer (a). The yellow rectangle marks the region where a spectrum image was acquired with an exposure time of 0.2 s/pixel. b) Relative O and Ti concentrations (atomic %), obtained from the quantification of the O *K* and the Ti $L_{2,3}$ absorption edges (false color scale). For the EEL acquisition, a 5 mm aperture was used with a camera length of 3 cm, giving a collection semi-angle of 20.8 mrad and a convergence semi-angle of 35 mrad. The exposure time was of 0.2 s/pixel. Spectrum images were acquired using the sub-pixel scanning mode, where the beam is scanned across each pixel while acquiring an averaged spectrum

These findings suggest that the surface of the oxide is not simply a reduced and defective layer, but a different TiO-like oxide phase resulting from recrystallization after bombardment. In what follows, we will see how treatments like this in more complex materials can induce new surface phases with different physical properties than the original crystal.

Surface phases in $SrTiO_3$

Back to our analysis of irradiation effects on STO, EELS was also used in order to assess the irradiation effects on the electronic and compositional properties of the

samples. It is known that ion bombardment of titanium oxides produces a reduction of Ti in the regions closer to the surface (*110*). Line-scans were produced by scanning the electron beam along a line perpendicular to the surface while an EEL spectrum is measured in each pixel. The raw spectra were treated with principal component analysis (*77*) to reduce random noise from spectroscopic images. In order to obtain the oxidation state of titanium and study the oxygen concentration profiles, the fine structure of Ti $L_{2,3}$ and O *K* edges was analyzed. According to the dipole selection rule, the Ti $L_{2,3}$ edge of the transition metals results from the excitation of *2p* electrons to unoccupied states of *3d* nature. These edges show two characteristic white lines, originated by transitions from the $2p_{3/2}$ (L_3) and $2p_{1/2}$ (L_2) levels (split by the spin-orbit interaction) to empty levels of the *3d* band. The Ti L_2 and L_3 lines are further split in two, as observed by x-ray absorption (*111*) and EELS (*112*), due to the crystal-field splitting of the threefold t_{2g} (d_{xy}, d_{yz} and d_{xz} orbitals) and twofold e_g (d_z^2 and $d_{x^2-y^2}$ orbitals) states. The L_3 first peak shows transitions from the $2p_{3/2}$ Ti level to the $2t_{2g}$ level, and the L_3 second peak, from $2p_{3/2}$ to the $3e_g$ level (*113*). This splitting is strongly affected by changes in the occupation of the Ti *3d* band. On the other hand, the O *K* edge (around 530 eV), gives us information on excitations of oxygen *1s* electrons to *2p* bands, which are hybridized with empty Ti *3d* orbitals (*114*). The near edge fine structure suffers significant changes with the occupancy of *3d* states in Ti and therefore it also provides information about the Ti oxidation state. This edge shows two peaks at the onset around 530 eV, due to the Ti *3d* t_{2g} - e_g splitting and is highly sensitive to bonding features (*115*). Hence, the analysis of the O *K* edge pre-peak will also provide information about the Ti *3d* band occupancy and the Ti oxidation state. O *K* spectra exhibit another set of bands around 537-546 eV. These features originate from interactions between oxygen *2p* states, and Ti *4s* and *4p* states (*116*).

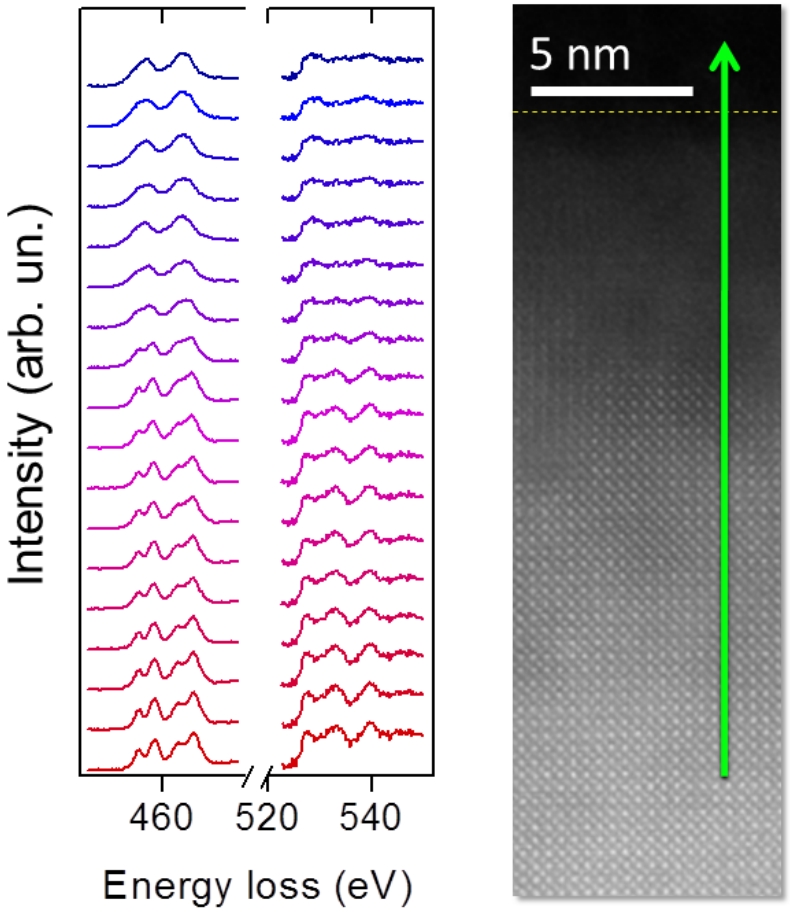

Figure 3.9: EEL spectra of Ti $L_{2,3}$ and O *K* edges obtained along the green arrow marked in the HAADF image with an exposure time of 1s/pixel of a sample irradiated at 36 W for 5 minutes. The EELS intensity has been normalized in order to show clearly the variation of the peaks along the spectrum image, and the spectra have been shifted vertically for clarity. A yellow dotted line on the HAADF image marks the position of the surface.

In Figure 3.9, we show the variation of the Ti $L_{2,3}$ and O *K* edges when the electron beam is placed on the surface and scanned into the material. The Ti $L_{2,3}$ edge away from the surface shows features typical of the bulk Ti^{+4}, with a noticeable crystal field splitting. But closer to the surface it looks more like a Ti^{+3} state, where only two peaks are present. The *3d* orbital, unoccupied in the bulk ($3d^0$), would become partially filled in the surface ($3d^1$) as Ti changes from a +4 to a +3 oxidation state. The $L_{2,3}$ onset also exhibits a chemical shift and moves to lower energies near the surface, which also indicates an oxidation state variance (*116*). These changes are consistent with a decrease in the oxidation state of Ti atoms (*117*), although some smearing of the fine structure due to amorphization may be possible.

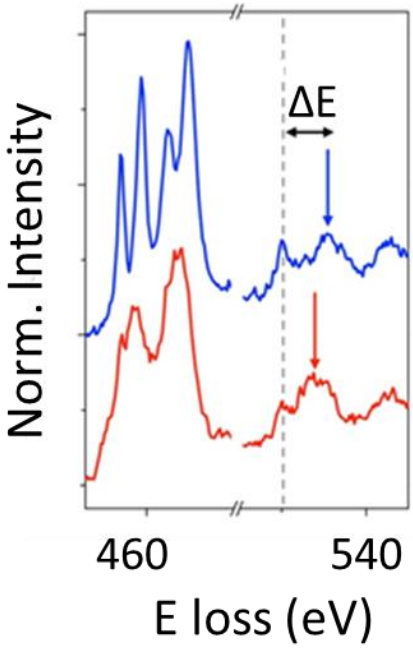

Figure 3.10: EELS reference spectra showing the Ti $L_{2,3}$ and the O *K* edges for bulk STO (blue) and LTO (red). The spectra have been displaced vertically for clarity. The ΔE peak separation is marked. Adapted from ref. (*29*).

The Ti oxidation state can be quantified through the analysis of the Ti $L_{2,3}$ edge. In order to do so, a MLLS fitting was performed using as references the spectra of $LaTiO_3$ (Ti^{+3}) and $SrTiO_3$ (Ti^{+4}) shown in Figure 3.10. As explained in chapter 2, the fit coefficients give the statistical weights associated with Ti^{+3} and Ti^{+4} components, providing a way to obtain the Ti valence.

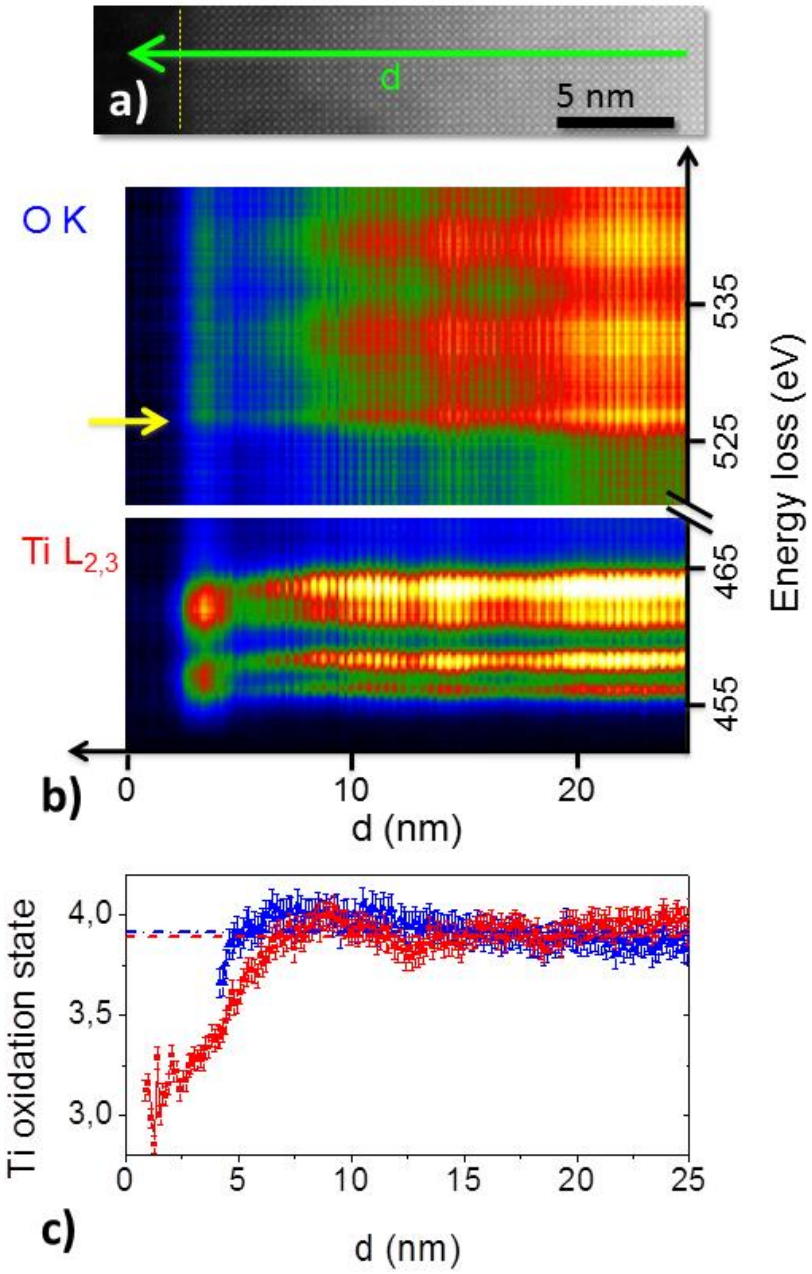

Figure 3.11: EELS line-scan along with Ti oxidation state quantification of the sample irradiated at 36 W for 5 minutes. (a) HAADF image showing the direction of the scan (green arrow). The surface is marked with a yellow dashed line. (b) EELS data, showing the O *K* and the Ti $L_{2,3}$ edges acquired with an exposure time of 1s per pixel. A yellow arrow marks the onset (pre-peak feature) of the O *K* edge. (c) Ti oxidation state profiles along the direction of the green arrow in (a), on a matching scale: the oxidation state profile calculated from the O *K* (Ti $L_{2,3}$) edge is shown in blue (red).

Figure 3.11 shows another line-scan from the same specimen, with the O *K* and Ti $L_{2,3}$ edges (Figure 3.11(b)). For this data set, Figure 3.11(c) shows the result of the MLLS

fitting analysis (in red). The topmost surface layer, heavily damaged, exhibits a drastically reduced Ti, with oxidation states near +3. As the electron beam moves into the material, a more bulk-like Ti valence is recovered, about 10 nm into the substrate. The average value for the Ti oxidation state below the damaged layer is +3.89 ± 0.11 (red dotted line on Figure 3.11(c)). This value is maintained as deep into the substrate as the whole measurement range, tens of nm. The value of the Ti oxidation state can also be extracted from the analysis of the O *K* edge, where a clear evolution can also be seen in Figure 3.9. The edge onset shifts to higher energy losses near the surface (the onset is marked with a yellow arrow on Figure 3.11(b)), characteristic of a reduction of the Ti valence state (*117*). The separation between the first and the second peak decreases significantly, and the intensity of the pre-peak is also reduced. A way to quantify these changes consists on measuring the difference in energy between the peak positions of the pre-peak and the adjacent main peak (ΔE) of the oxygen *K* edge (*29, 77*). Gaussians curves are fitted to both the pre-peak and the main peak, and the difference in positions for the centers of both Gaussians is extracted along the line spectra shown in Figure 3.11. Assuming that there is a linear correlation between the ΔE and Ti oxidation state (*118*) and using the values of ΔE from bulk STO (ΔE=5,61 eV) and LTO (ΔE=3,73 eV) thick film as a reference (*29*), the Ti oxidation state can be extracted. However, since the O *K* fine structure is so smeared out near the surface, the method renders artifacts for the first few atomic layers, so these points have not been included here. For the rest of the scan, the quantification is reliable and shown in blue on Figure 3.11(c). We obtain a titanium +3.6 oxidation state near the surface. Again, within a length scale of 10 nm the Ti oxidation state increases and reaches a value of +3.92 ± 0.06.

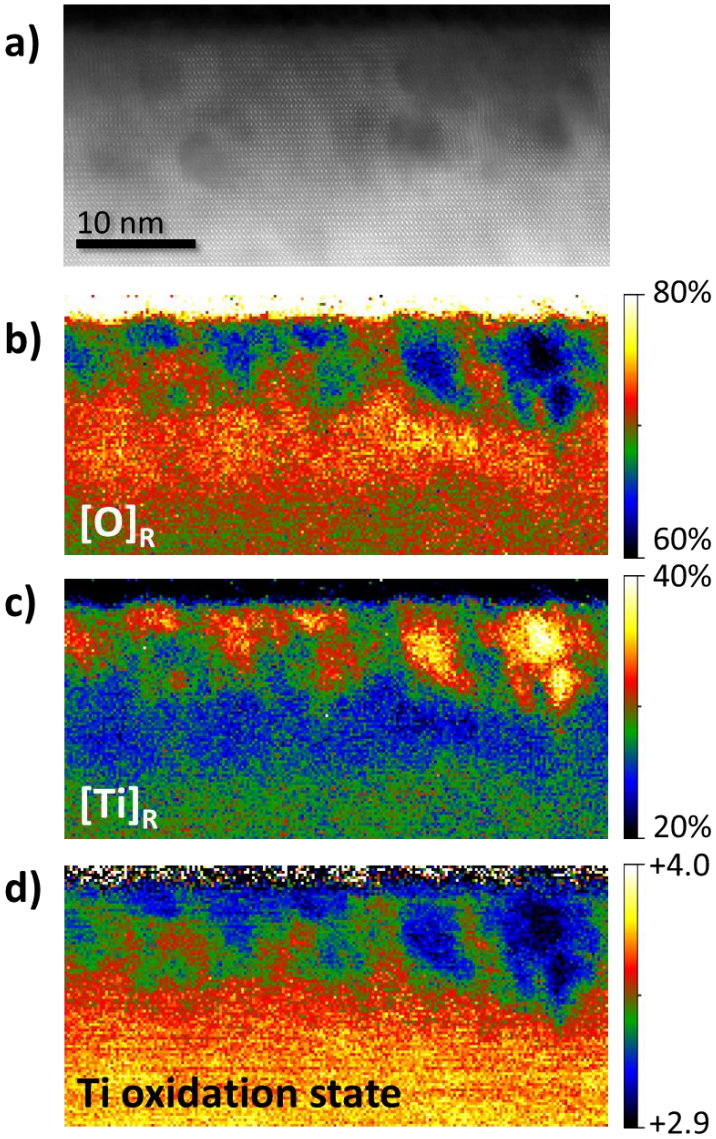

Figure 3.12: EELS spectrum-image along with relative compositional maps and Ti oxidation state quantification of a sample irradiated at 36 W for 5 minutes (a) HAADF image of the damaged surface area acquired simultaneously with the spectrum image. Relative compositional maps for oxygen (b) and titanium (c) obtained from the quantification of the O *K* and Ti $L_{2,3}$ edges, respectively. (d) Ti oxidation state map obtained with the MLLS method applying to the Ti $L_{2,3}$ edge. The dark blue zones correspond to Ti $^{+3}$ state and the light yellow zones are close to Ti $^{+4}$ state. On the dark blobs the residual of the MLLS fit is large enough that some presence of Ti^{+2} cannot be disregarded. The top few pixels correspond in all cases to the glue line. These pixels have been ignored for quantification purposes.

The values obtained from both methods employed agree well within error bars, and they clearly denote a mixed distribution of Ti^{+3} and Ti^{+4} in the heavily damaged layer near the surface. As we go deeper in the material, the concentration of Ti^{+4} increases but the oxidation state does not reach +4 completely within the measurement range.

Unfortunately, in our experiments we are limited to surface studies: the specimen thickness increases as we move deeper into the material preventing high quality EELS data acquisition. The estimated thickness of the confinement zone suggested by magnetotransport data is 260 nm (*87*), a depth range that can hardly be probed in our STEM specimens. Nevertheless, two distinct regimes near the surface layer are observed, so in order to gain lateral statistics, 2D spectrum images were acquired. Figure 3.12(a) shows a high resolution HAADF image of the damaged surface area. Heavily damaged zones, where the crystalline contrast is lost, appear darker in the image. The O and Ti relative concentration maps quantified using the routines available in the Gatan Digital Micrograph software are shown in Figure 3.12(b) and (c), respectively. These routines may not be completely accurate in the presence of dechanneling, but we can comment on general trends and qualitative changes observed in relation to the features observed in the HAADF images. The layer is not homogeneous in the lateral length scale, as these maps show an intense decrease of the O concentration in these damaged nano-regions. In Figure 3.12(d), we show the calculated Ti oxidation state from the MLLS analysis of Ti $L_{2,3}$ edge. Within the most damaged O deficient areas the oxidation state is close to +3. As we go deeper in the bulk, over 10 nm far from the surface, the oxidation state reaches a value close to +3.9 but it does not achieve the full +4 value of the bulk.

Discussion

We have studied the effects of irradiation procedures on the surface of titanium oxides in high quality STEM specimens. In both cases the irradiation modifies the composition of a superficial layer, producing new crystalline phases or even affecting the material enough to produce an insulator-to-metal transition. The ion bombardment of TiO_2 substrates induces a TiO-like layer, which exhibits a crystalline order and a defined orientation relative to the TiO_2 substrate. On the other hand, the irradiation of STO single crystals with Ar^+ plasma with a reactive ion etching process generates a highly damaged area within 10-12 nm of the surface, as observed by STEM images. We find a correlation between the metallic behavior and the degree of surface damage, where the most defective samples are the ones that present lower resistance values. The irradiation produces a heavy amorphization of the surface, along with significant O displacements in

a highly O deficient layer. EELS analysis demonstrates that these damaged regions show a dramatic reduction of the oxidation state of Ti atoms, which is near +3 at the very top layers. Within 10 nm of the surface, approximately, the high structural quality is recovered and the Ti/O ratio values approach those of the bulk. Nevertheless, the Ti ions remain slightly reduced.

These results can be interpreted to explain the conduction properties of the irradiated STO single crystals. One would think that electron doping ensuing from the O vacancies may be directly responsible for the metallic behavior. Indeed, it is well known that doping STO with oxygen vacancies affects drastically its electronic structure and density of states. These changes lead to a variation in the electronic properties of the material, as previous theoretical studies proof (*119*).

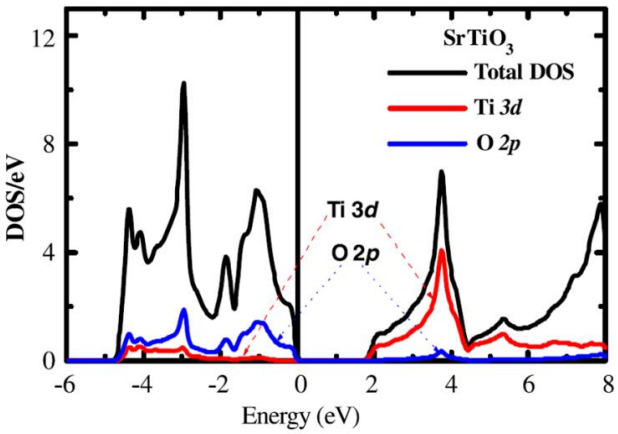

Figure 3.13: STO total and partial density of states calculated with FLAPW (Full-potential linearized augmented plane wave method). Adapted from ref. (*119*)

For example, Figure 3.13 shows the total and partial density of states (DOS) of bulk STO calculated with the FLAPW (Full-potential linearized augmented plane wave) method. The graphic displays how the minimum of the conduction band ($E\sim+2eV$) is dominated by Ti *3d* states with very small contribution from O *2p* levels. The maxima of the valence bands are dominated by the O *2p* levels, with a small contribution from Ti *3d* levels. Therefore, the Ti-O_6 octahedron is the main component of the valence band maximum and the conduction band minimum states. The Sr levels barely contribute because the Sr^{2+} ions have a nearly full ionic character. The strontium titanate bond structure is then, a combination between the covalent bond Ti-O_2 and the ionic Sr^{2+}-O^{2-}. This situation entails a tendency in STO to trap the two electrons associated with an

oxygen vacancy, transferring them into the Ti *3d* levels (*120*). The next figure shows the diagrams for the DOS of STO when introducing an oxygen mono-vacancy and a di-vacancy. Figure 3.14(a) displays how the Fermi level moves into the conduction band, giving rise to an insulator-to-metal transition when introducing a mono-vacancy. The conduction band minimum energy shifts to lower energies, reducing the gap of the material. Occupied states in the minimum of the conduction band originate from Ti *3d* levels. Thus, the two electrons produced by the introduction of the oxygen vacancy would relocate into empty Ti *3d* levels in the conduction band, producing a neutral charge-state at the vacancy.

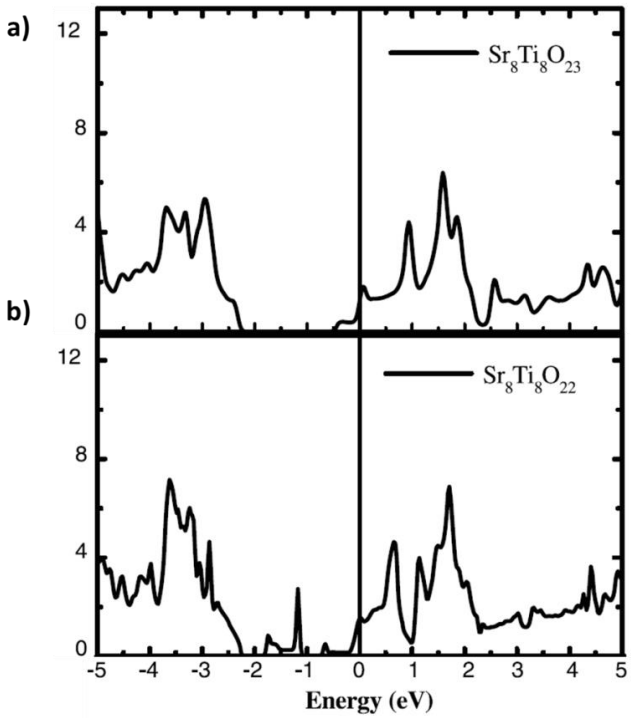

Figure 3.14: STO total density of states with a) oxygen mono-vacancies and b) oxygen di-vacancies. Adapted from ref. (*119*).

Figure 3.14(b) shows the DOS in when introducing a di-vacancy. In this case, there is a distortion close to the conduction band minimum, and the electronic configuration of STO presents a metallic ground state. There are states separated from the bottom of the conduction band, below the Fermi energy, showing that some of the electrons associated with the removing of two oxygen atoms are localized in the vacancy, forming a negative charge-state. Both cases show how introducing oxygen vacancies in STO leads to an

insulator-to-metal transition. The excess of electrons gets trapped within the Ti *3d* band, reducing the Ti oxidation state from +4 (with an electronic configuration $3d^0$) to +3 ($3d^1$ configuration). Such reduction is responsible for the measured insulator-to-metal transition (*87*). It is also important to note that the thickness of the conducting layer exceeds the ion range by orders of magnitude, probably due to thermal diffusion of oxygen vacancies into the bulk (*89*) or to electrons delocalized over long distance due to screening by the large dielectric constant (*121*).

In conclusion, the results in this chapter highlight the relevance of irradiation as a path towards novel routes to produce heterostructures and interfaces between oxides. Such controlled surface treatments may produce new phases on the surface of oxide crystals with distinct physical properties. These techniques may result in a new route in the development of devices based on oxide interfaces. In the next chapter, we shift gears towards systems where oxygen vacancies are responsible for the bulk functionality, such as ionic conductors.

Chapter 4: Origin of ionic conductivity barriers at Y_2O_3 stabilized ZrO_2 grain boundaries

Ion blocking at grain boundaries in polycrystalline ionic conducting electrolytes is one of the main obstacles we need to outpace to improve the performance of solid state fuel cells and batteries. Understanding the origin of these ionic conductivity barriers at grain boundaries is therefore a matter of great interest. In this chapter, we study a single grain boundary in a symmetric Y_2O_3 stabilized ZrO_2 (YSZ) bi-crystal by dielectric spectroscopy, advanced electron microscopy techniques and density functional theory. We use strain analysis in the Z-contrast images to study the structural distortions around the grain boundary dislocation cores, atomic resolution EELS quantification measurements to analyze the compositional changes, and DFT calculations to study the electronic consequences of these changes at the grain boundary region. We find that important chemical and electronic alterations take place within one nm from the grain boundary plane, where extra electrons originated by the presence of oxygen vacancies give rise to an electrostatic potential dip. We will present these results as the explanation for ionic conductivity blocking at grain boundaries in oxygen ionic conductors, a view that is opposed to previous knowledge.

Introduction

In the past years, there has been a growing interest in ionic conducting materials, principally motivated by their wide range of applications in solid state devices. The possibility of using these systems as electrolytes in solid oxide fuel cells (SOFC) makes them one of the most promising materials for designing alternatives to the contemporary energy production technologies (*122–124*). SOFC are devices capable of converting chemical energy in electrical energy using just hydrogen, methane or carbon monoxide as fuel with a high efficiency and without generating any polluting emission (*125*). The largest limitation of these devices is the high operational temperature needed to achieve the required ionic conductivity. For YSZ, the most popular ionic conductor used as electrolyte, this temperature is close to 800°C (*123*, *124*). These materials are conventionally used in a polycrystalline form, and hence, their performance is strongly limited by the presence of grain boundaries, which affect significantly the macroscopic mechanical and electrical properties of the material (*126–128*). It has been reported, that the ionic conductivity is reduced at grain boundaries, where the resistivity is at least one order of magnitude higher than in the bulk (*129*). This resistance usually dominates the overall ionic conductivity due to the structural and chemical changes present within the grain boundaries (*130–132*). Surprisingly, the explanation to this ionic conductivity barrier is still a subject of controversy (*126*, *131*, *133–140*).

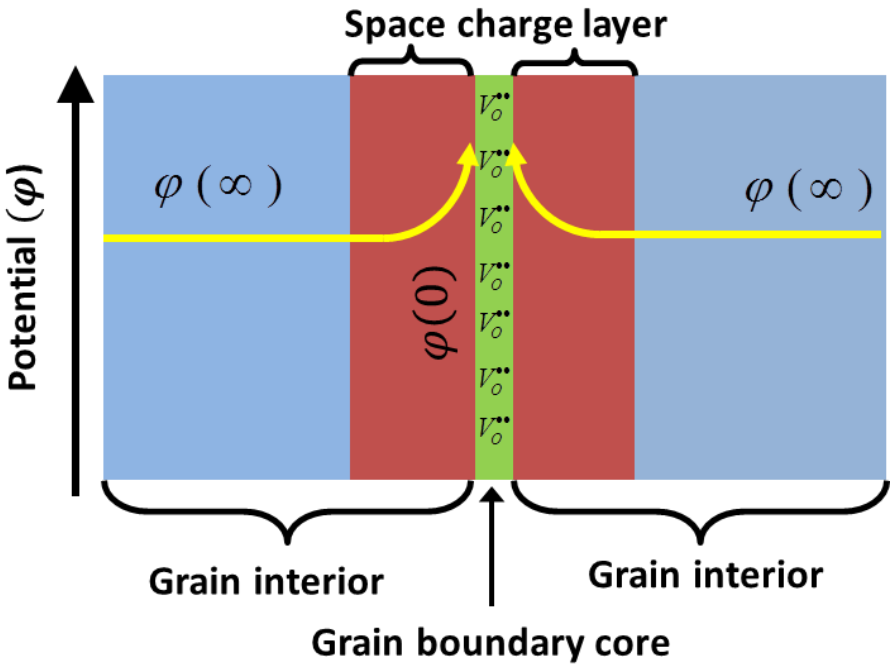

Figure 4.1: Sketch showing the current space charge layer model. The presence of oxygen vacancies at the grain boundary produces a long range space charge layer (λ^*) shown in red, at both sides of the grain boundary.

The current belief is based on the presence of a space charge layer produced by an oxygen vacancy depletion region that screens a positive charge localized at the grain boundary (Figure 4.1). If a space-charge region is associated with each side of the grain boundary, when the frequency of the ac electric field is low enough positive and negative charge alternately accumulates at each side of the grain boundary (separated by a distance $2\lambda^*$) due to the blocking of mobile ions. λ^* would be the thickness of the space charge layer at each side of the grain boundary. The thickness of the space charge layer λ^* is determined by the Debye screening length L_D, and can be estimated from experimental data using the Mott-Schottky model (*141*). A recent study from our group (*142*) found a value of 1 nm for the space charge layer thickness of a single grain boundary in a YSZ bi-crystal using dielectric spectroscopy measurements (*143, 144*). Surprisingly, this value is one order of magnitude thinner than found on previous reports (*141*). Here we will show these dielectric spectroscopy measurements and by combining STEM-EELS and density functional theory calculations we will shed some light into the origin of ionic conducting barriers in oxygen ionic conductors.

Ytrium stabilized zirconia (Y_2O_3 stabilized ZrO_2)

Oxides with fluorite structure, as zirconium oxide or zirconia, have a general chemical formula AO_2, with a face-centered-cubic structure where A is a tetravalent cation and the oxygen anions are placed in the tetrahedral sites, as illustrated in Figure 4.2. Some of these materials tend to have vacancies in the oxygen anion lattice sites, which makes them good candidates for conducting oxygen ions. Undoped zirconia can be stabilized into three different crystal structures depending on temperature (*145*). At temperatures superior than 2600ºC, it exhibits a fluorite cubic structure. However, substituting the Zr^{4+} cation with a larger species with lower valence number, such as Y^{3+}, makes it stabilize in the cubic fluorite structure at room temperature. Figure 4.2 represents the doping process of ZrO_2 with Y_2O_3, which is called yttrium stabilized zirconia (YSZ). YSZ has a Fm3m space group and a lattice parameter of 5.14 Å.

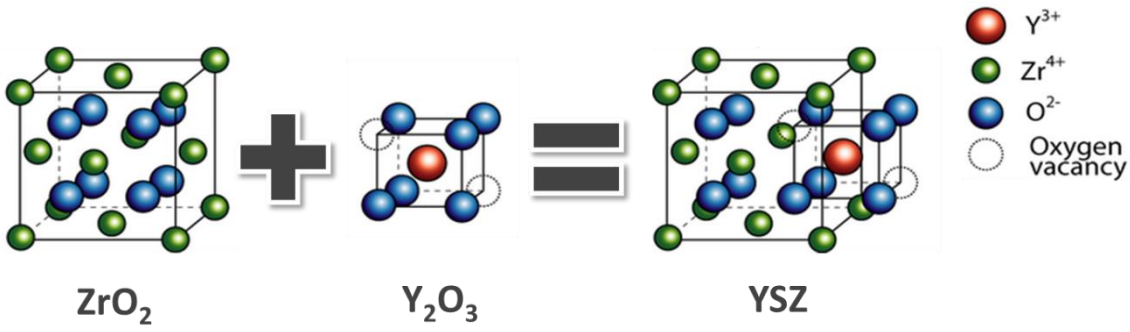

Figure 4.2: Simple model of the doping process where Y_2O_3 dopes the ZrO_2

Furthermore, when doping ZrO_2 with a compound like Y_2O_3, where yttrium has a lower oxidation state and a bigger ionic radius, oxygen vacancies are introduced into the zirconia structure (*146*, *147*). More specifically, introducing one Y_2O_3 molecule into the ZrO_2 lattice produces one oxygen vacancy by the following equation:

$$Y_2O_3 \rightarrow 2Y_{Zr} + 3O + V_o$$

where Y_{Zr} represents the Y ions replacing the Zr cations, O is the regular oxygen ion on the anionic site and V_o is the oxygen vacancy. This relation lets us know the concentration of oxygen vacancies from the concentration of Y ions. Several studies on YSZ have shown that the highest ionic conductivity for all the temperature range ($0{,}1\ Scm^{-1}$ a

1000°C) is obtained for a doping level of 8-9 mol% of Y_2O_3 in ZrO_2 (*148*, *149*). Higher dopant concentration causes the conductivity to decrease. This occurs because the ionic conductivity does not depend only on the concentration of oxygen vacancies, but also on the mobility of these vacancies. The ionic conductors are singular materials, where the conduction process is produced by the diffusion of charged ions through the material. This diffusion is thermally activated and the dependence of the ionic conductivity with the temperature is given by:

$$\sigma \sim exp\left(\frac{-E_a}{KT}\right)$$

Here, σ is the ionic conductivity, K is the Boltzmann constant, T the temperature and E_a is the activation energy for ion migration. From the conductivity description, we can obtain the mobility through the following equation:

$$\mu = \frac{e\sigma}{n(Ze)^2}$$

In ionic conductors, the charge carriers are much bigger and heavier than electrons, therefore their velocity is smaller and the conductivity values are also smaller than in metallic materials. Moreover, these charge carriers are constituents of the material structure and need available positions to move through the crystalline lattice, which are called vacancies. Then, the mobility depends on the vacancy concentration, the ionic radius of the dopants and the microstructure of the material. The ionic charge carrier will move from one vacancy position to the next, producing the ionic conduction process (as illustrated in Figure 4.3).

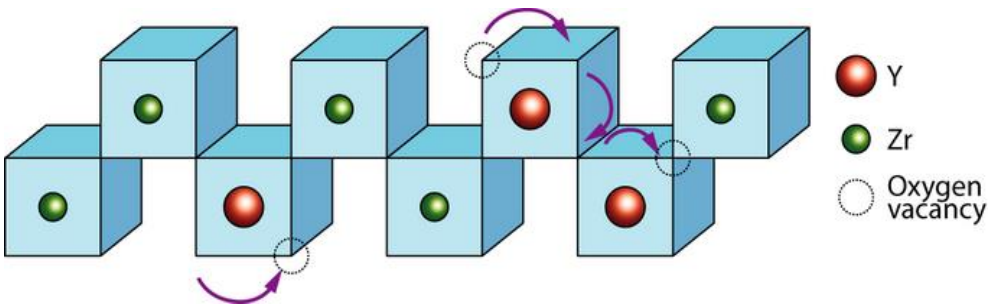

Figure 4.3: Model illustrating the oxygen ionic conduction in YSZ

Overall, YSZ exhibits many characteristics that make it a most valuable material in different application areas. Thanks to the high ionic and low electronic conductivities, it can be used in chemical sensors or as electrolyte in solid oxide fuel cells. Moreover, YSZ has a high chemical stability and hardness, even at elevated temperatures, which also makes it a good option for fuel cells, which operate at very high temperatures.

Experimental results

YSZ bi-crystals were made by means of solid phase intergrowth. In order to produce a bi-crystal, two single crystals are cut to obtain the surface in the desired orientations, and then, aligned together and annealed under pressure in an ultra-high vacuum environment. The result is a smooth grain boundary at the atomic scale, free from impurities and deformation dislocations. The sample studied is a commercial 9% mol yttria content YSZ bi-crystal with a symmetrical 33° [001] tilt grain boundary acquired from MaTeck GmbH. The bi-crystal was cut and polished in the (001) orientation. The bicrystal grain boundary was characterized by dielectric spectroscopy measurements conducted using a Novocontrol BDS-80 system. Measurements were carried out in the frequency range 10^{-3} – 10^{7} Hz and at temperatures between 240 – 300 ºC. For electron microscopy characterization, the specimen was prepared for a planar view observation with conventional mechanical polishing and Ar ion milling. In order to prevent charging effects, as the material is highly insulating, the specimen was coated with a one nm thick iridium layer. Low-loss EELS spectrum images were acquired in a Nion UltraSTEM100 operated at 100 kV. The HAADF images and the high-loss EELS spectrum images were obtained in a Nion UltraSTEM200 operated at 200 kV.

Transport measurements

We analyzed the ion transport across the bi-crystal grain boundary using dielectric spectroscopy measurements. The impedance data have been fitted to an equivalent circuit shown in the inset of Figure 4.4. In this circuit, the contributions from the bulk and the grain boundary are modeled using a parallel resistor-capacitor combination (*143*) and afterwards, added in series. In order to account for the universal Jonscher's response, that

is commonly observed in ionic conductors (*150–152*), the ideal capacitor has been replaced by a constant phase element in the model. Figure 4.4 shows the complex impedance at several temperatures where the contributions from the bulk, grain boundary and electrodes can be separated and are observed at the highest, intermediate and lowest frequencies respectively. The experimental measurements are displayed in Figure 4.4 as open symbols and the results from the fit to the model are presented as solid lines in the same plot. The lowest frequency data is affected by blocking effects at the electrodes and has been excluded from the fits.

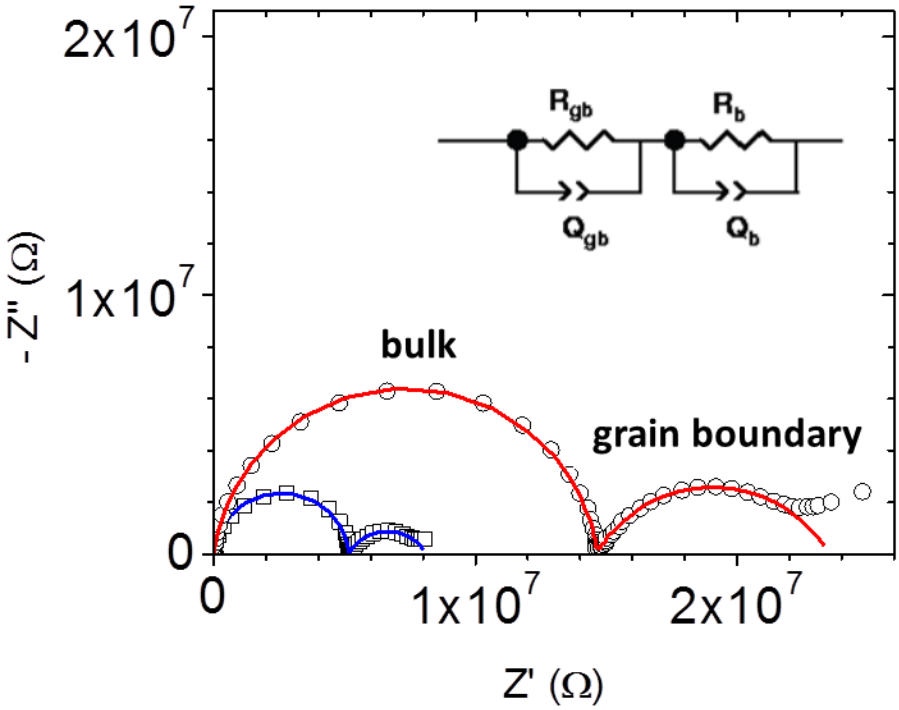

Figure 4.4: a) Complex impedance plots at 275 ºC (red) and 300 ºC (blue) showing the contributions to ionic transport due to the bulk (left semicircle) and to the grain boundary (right semicircle) in YSZ bicrystals with electrodes separated *d*=10 µm. Solid lines are fits to the equivalent circuit shown in the sketch.

In order to make the contribution from the grain boundary comparable to that of the bulk, as seen in Figure 4.4, we deposited two electrodes separated just a few microns at both sides of the grain boundary. We used electron beam lithography and sputtering techniques to pattern these electrodes, shown in Figure 4.5(a). From the dielectric spectroscopy measurements, we can give an estimate of the space-charge region thickness. Following the sketch in Figure 4.5(b) and assuming: first, that the thickness of

the YSZ substrates is infinite as compared to the width of the electrodes (W) and the distance between them (d), second, that the electric field lines are perpendicular to the grain boundary within the space charge region, and last, that the dielectric permittivity in the grain boundary is similar to the bulk value (*153*, *154*), then λ^* can be extracted from:

$$\frac{C_b}{C_{gb}} \approx \frac{2\lambda^*}{d_e}$$

where C_b and C_{gb} are the bulk and the grain boundary capacitance values and d_e is the effective distance between the electrodes. We obtain a value of $\lambda^* \approx 4 \pm 1$ Å, which is in the order of only one unit cell and about one order of magnitude smaller than previous reports (*141*).

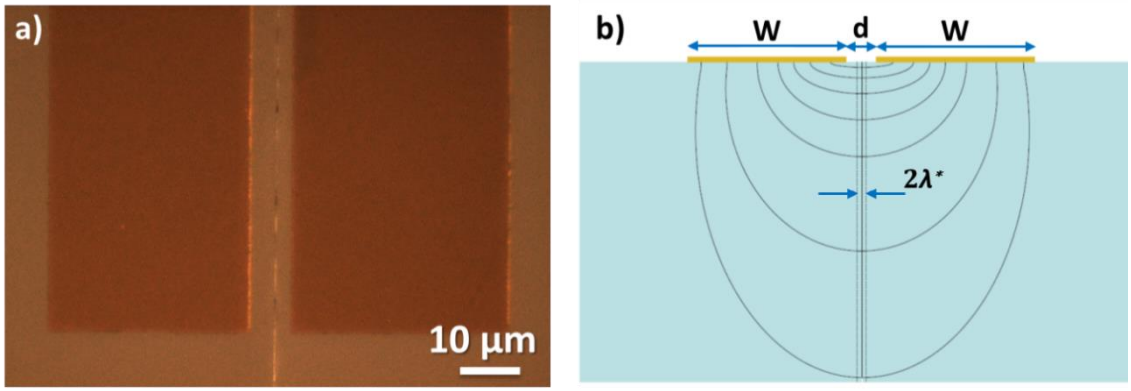

Figure 4.5: a) Optical microscopy image of the bi-crystalline boundary between the two gold electrodes. b) Sketch of the electrode geometry used and the inhomogeneous electric field created in the YSZ bicrystal. Solid lines represent electric field lines which are approximately perpendicular to the grain boundary plane within the space charge layers.

Structural characterization

We studied the structure of the dislocation cores at the grain boundary under the electron microscope. Depending on the directions and the angles of grain boundaries, bi-crystals may exhibit very different dislocation cores geometries. Therefore, resolving the atomic structure of the dislocation cores is a key task in order to understand the properties of the grain boundary (*155*). Figure 4.6 shows low and high magnification atomic resolution Z-contrast images of the YSZ 33° [001] symmetric bi-crystal grain boundary,

where a perfect array of dislocation cores can be observed. Neither disordered nor amorphous structures are present in the sample, which indicates that the boundary is successfully joined at the atomic level. White arrows indicate the (100) direction in each side of the grain boundary. The actual angle between the arrows is 65°, which means that actual the angle between the two sides of the symmetric bi-crystal is 32,5°. The right panel shows an amplified image of the dislocation cores, where the Zr/Y atomic columns are arranged in a symmetric manner with respect to the boundary plane. The boundary dislocation cores can be described by a repetition of a symmetric structural unit, marked with yellow lines in the image.

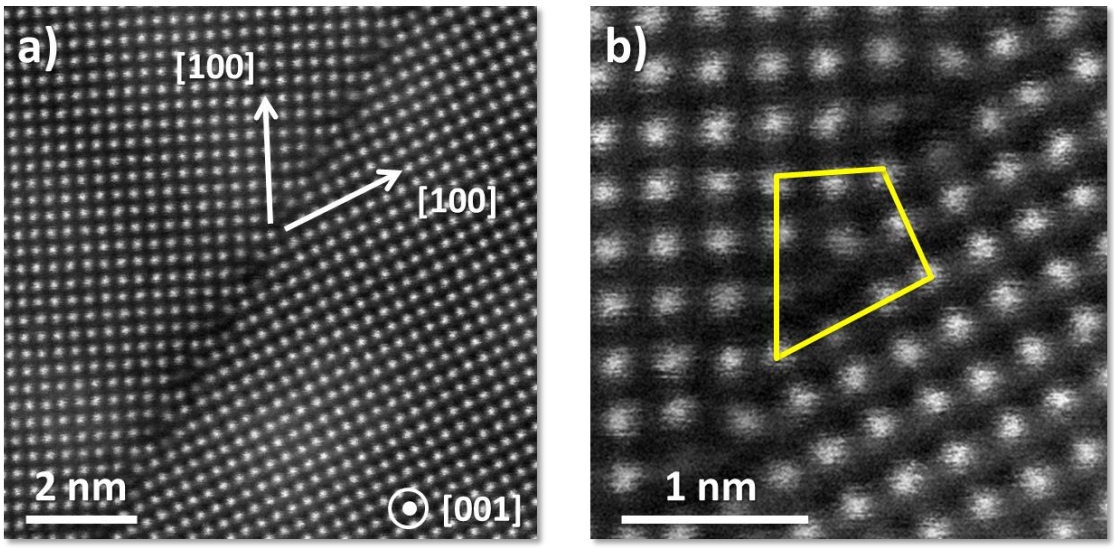

Figure 4.6: a) HAADF image of a YSZ symmetric 33° [001] bi-crystal showing the [100] directions in each side of the grain boundary. b) High magnification HAADF image with the grain boundary dislocation cores structural unit marked with yellow lines.

The crystalline structure of the grain boundaries has strong implications in the cation segregation or the presence of point defects as oxygen vacancies, thus, we carried out a quantitative strain analysis to better understand the structural changes close to the grain boundary plane.

Strain analysis

Large strain fields develop around dislocation cores that may have an impact on the physical properties of these systems. In order to measure the strain around the grain

boundary dislocation cores, we have used the "Peak Pairs Analysis" (PPA) suite for Digital Micrograph (*66*, *67*), as explained in chapter 2. Figure 4.7 shows images of different steps of the process: in Figure 4.7(a) we show a HAADF image of the grain boundary region, with the Fast Fourier transforms (FFT) for each side of the grain boundary. The directions (010) for both sides have been chosen as the reference base vectors for the strain analysis. On the right panel, we show the peak pairs map obtained from the image (a). The inset shows an amplified image of the peak pairs map. The structure of the dislocation cores is well resolved by the PPA plug-in.

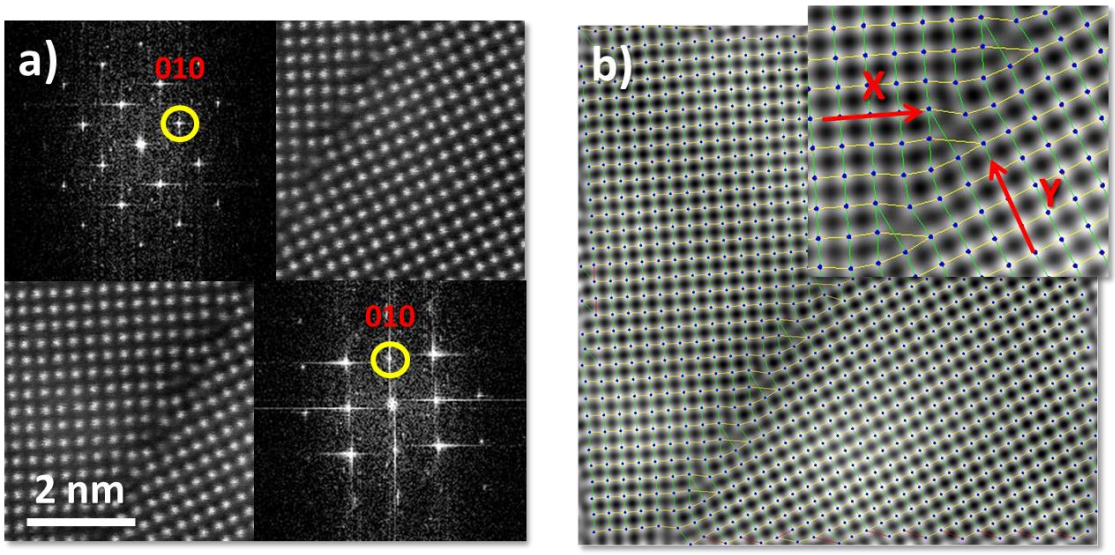

Figure 4.7: a) HAADF image of the YSZ grain boundary with the FFT of each side of the grain boundaries superimposed. The yellow circles mark the reflexions used as base vectors for the "Peak Pairs Analysis". b) Peak Pairs map from the image in (a). The inset shows the structure of the dislocation cores.

The maps of the rotation angle and the mean dilatation obtained from the PPA strain analysis are shown in Figure 4.8. The rotation angle shows a tilt of 22° between both sides of the grain boundary, which is the expected value for the symmetric 32,5° [100] bi-crystal. The second map shows the mean dilatation, $d_{xy} = \sqrt{\varepsilon_{xx} + \varepsilon_{yy}}$, around the grain boundary dislocation cores. The strain is localized around the dislocation cores, with a value of nearly 60% on the expansive sites of the dislocation cores. The expansive and compressive sites structure, typical of a grain boundary core, is well resolved in this analysis. The homogeneous green-brown color of the rest of the image shows how there are no appreciable long range structural distortions.

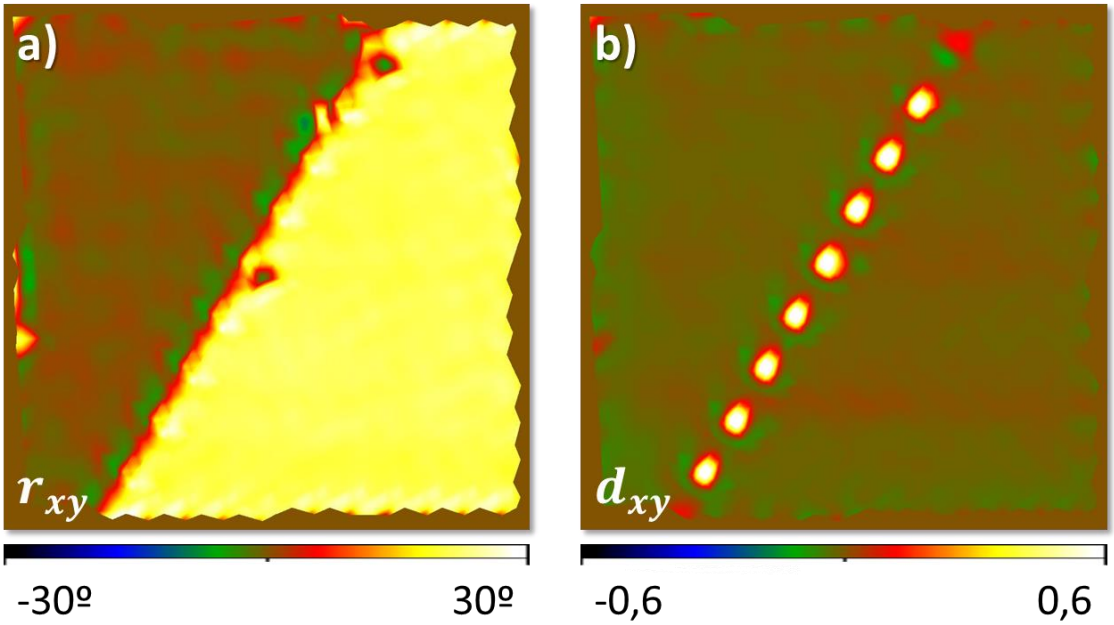

Figure 4.8: a) Rotation angle map between the (010) directions in each side of the grain boundary, having taken the left side as reference. b) Mean dilatation map of the grain boundary, showing the dislocation cores.

If we superimpose the mean dilatation (d_{xy}) map on top of the original HAADF image, it can be noticed that the expansive strain is localized to three atomic columns within the grain boundary dislocation cores, as shown in Figure 4.9 (a) and (b). Interestingly, there is an appreciable reduction of the image intensity for these three atomic columns. This intensity variation may be produced by two different factors: as the HAADF images show a contrast proportional to Z^2, this effect could be produced by changes in the average Z number of these atomic columns. Secondly, a partial occupancy of these columns could also produce a similar effect (*156*). We will use atomic resolution EELS studies to evaluate these possibilities.

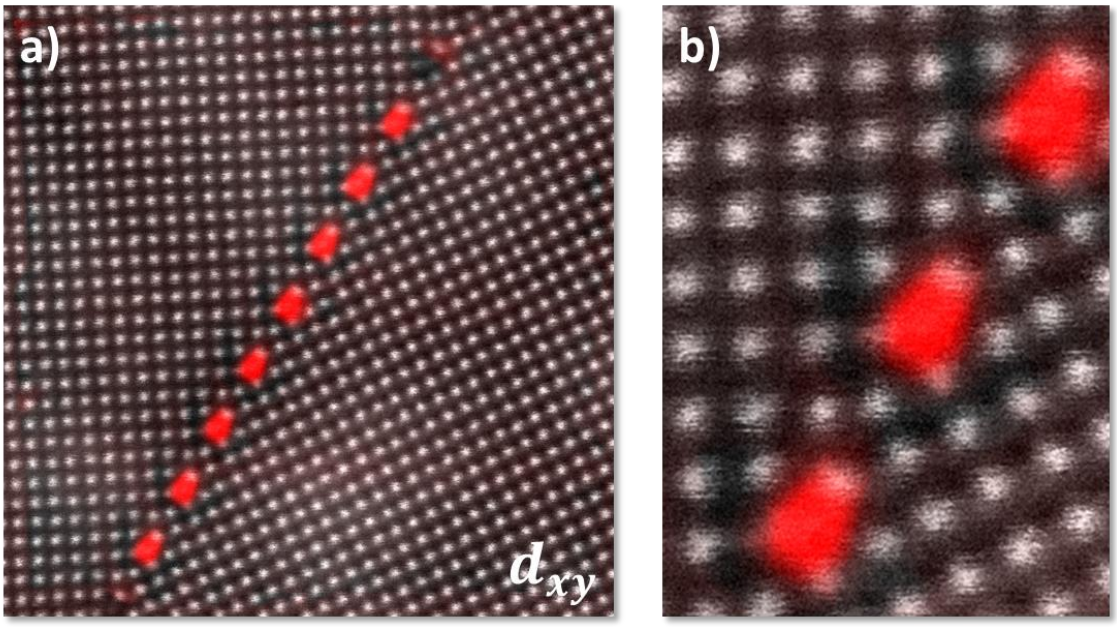

Figure 4.9: a) Mean dilatation map superimposed on a HAADF image of the grain boundary. b) Magnified region from image (a) where the mean dilatation map shows the three expansive positions in the grain boundary dislocation cores.

EELS characterization

To study the compositional properties of the grain boundary, which could help finding the origin of the ionic conductivity barrier in these systems, we used the EELS. Several EEL spectrum images were acquired in different regions of the bi-crystal specimen. The study of Zr and Y elements by EEL spectrometry entails a significant difficulty. There are minor *M* edges in the 300-400 eV range, but the signal-to-noise ratio and the localization of the signal is very low for these edges. Other option is acquiring the signal from the $L_{2,3}$ edges which have very high energy losses (2080 eV and 2200 eV for Y and Zr, respectively). However, long exposure times or very high beam intensities are needed to acquire spectrum images using these high energy edges.

With these issues in mind, we have examined both the low and the high loss edges. First, we acquired EEL spectrums of the *M* edges in the 300-600 eV range using a Nion UltraSTEM 100 operated at 100KV and equipped with an Enfina Gatan spectrometer. We used a convergence semi-angle of 30 mrad and an EELS collection semi-angle of 50 mrad and a beam current of 10-20 pA. The spectrum image was acquired using an energy dispersion of 0.5 eV/ch and with an exposure time of 0.05 s/pixel. Random noise was

reduced using principal component analysis (*74*). Figure 4.10 shows normalized integrated signal maps corresponding to the Zr $M_{4,5}$, Y $M_{4,5}$, and O *K* edges, the spectrum image was acquired in the area marked with a yellow box in Figure 4.10(a). Although the *M* edges have a relative low energy and the signal is poorly localized, from the analysis of these maps we can see large compositional changes with the periodicity of the grain boundary dislocation cores, as previously reported for grain boundaries (*137*, *155*, *157–159*). There is a depletion of the oxygen content in the vicinity of the grain boundary plane, accompanied by a reduction of Zr and a strong increase of the Y signal, which could be explained by a segregation of Y cations into the dislocation cores, as have been reported previously for grain boundaries in YSZ (*126*, *136*, *160*, *161*).

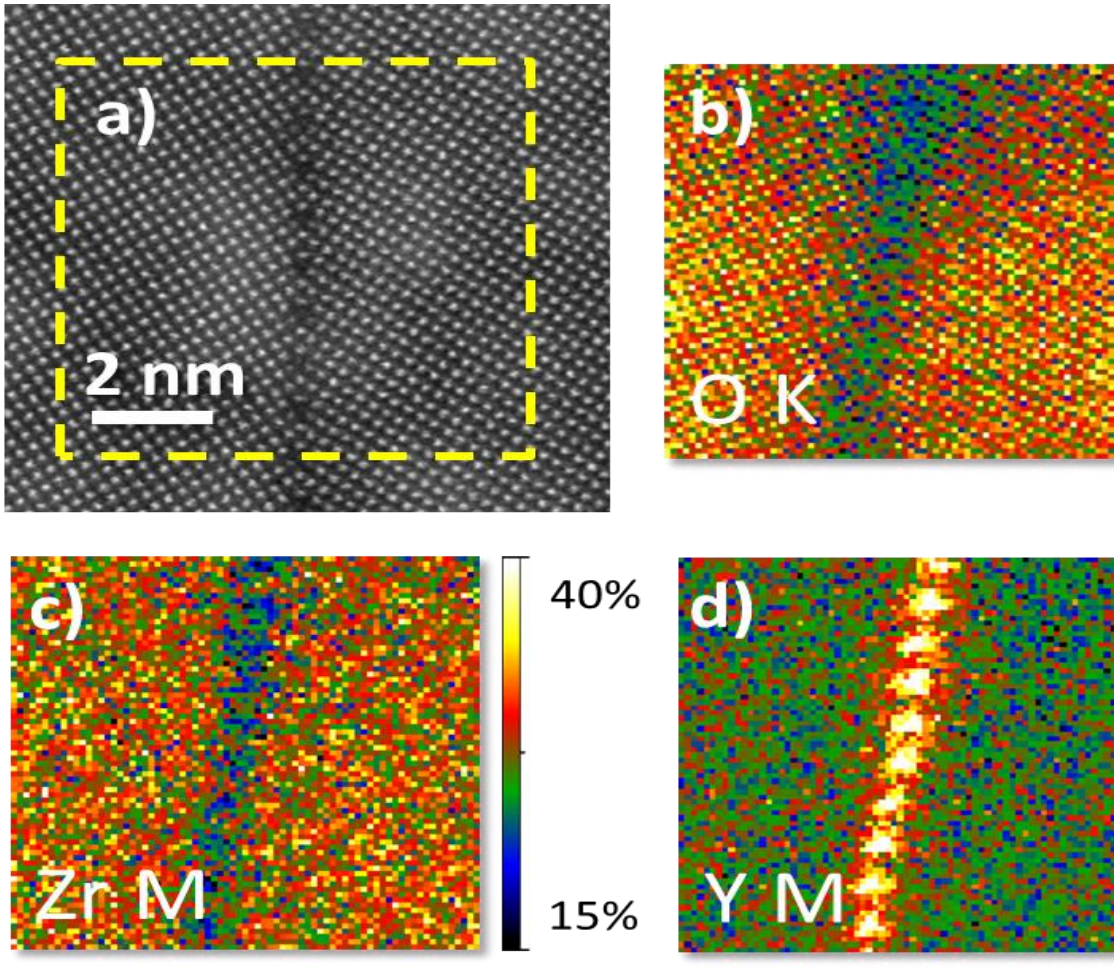

Figure 4.10: a) Z-contrast image of the grain boundary region obtained in a Nion UltraSTEM 100 operated at 100kV (a), the yellow dashed box marks the area where an EEL spectrum image was acquired. (b), (c) and (d): Atomic resolution, integrated signal maps of the Zr $M_{4,5}$, Y $M_{4,5}$ and O *K* edges, respectively, normalized to the nominal bulk concentration. The exposure time is 0.05 s per pixel. Some spatial drift is observed.

We also studied the same specimen in a Nion UltraSTEM 200, operated at 200KV and equipped with an Enfinium Gatan spectrometer. The Enfinium is capable of much faster acquisition times and has a 2048 channels CCD permitting same time acquisition of low (O *K* edge) and high (Zr and Y $L_{2,3}$ edges) energy loss edges using an energy dispersion small enough to measure the fine structure features. The probe forming aperture was 30 mrad and the EELS collection semi-angle was 36 mrad. The EEL spectra in Figure 4.11 show averaged Zr and Y $L_{2,3}$ edges from the grain boundary core region and the bulk. The Y signal increases on the grain boundary cores, with respect to the bulk. At the same time, the Zr signal decreases on the grain boundary. These results are consistent with the analysis of the previously shown low-loss energy *M* edges.

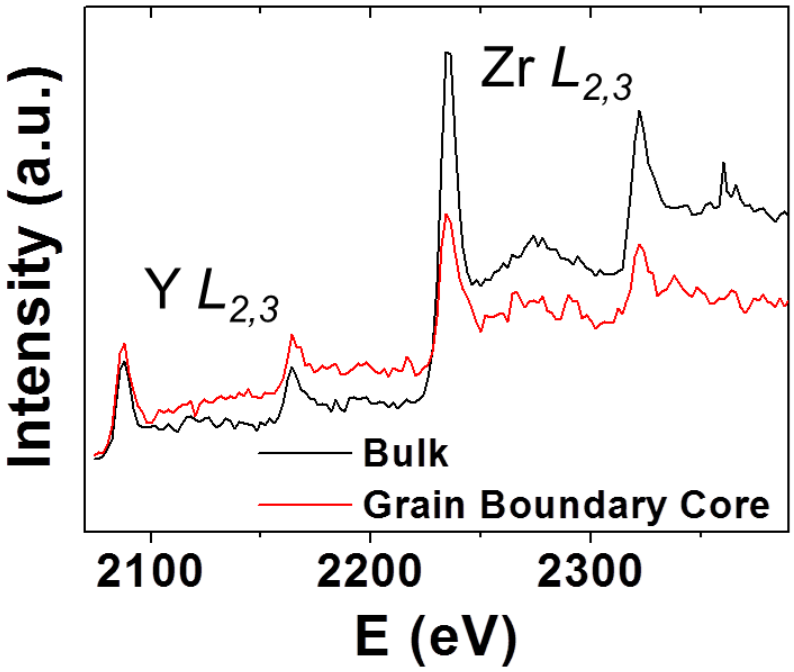

Figure 4.11: Averaged Y $L_{2,3}$ and Zr $L_{2,3}$ EEL spectra from the bulk crystal (black) and the dislocation core (red).

Thanks to the high signal localization of the *L* edges for Zr and Y, we can resolve the question that we proposed earlier in the chapter about the intensity decrease in the expansive sites of the GB dislocation cores. In order to asses this study, reducing as possible the experimental errors, the quantification was done in averaged spectrums from the regions marked with yellow boxes in the Figure 4.12(a). These areas correspond to the bulk of the specimen and the three different expansive sites spotted in the strain analysis.

We used the compositional quantification routines available in Digital Micrograph for this study. The results, shown in the table in Figure 4.12(b), exhibit a clear difference between the three atomic columns analyzed. In column 1, we measure a very strong Y segregation, more than doubling the bulk value, while the Zr concentration stays closely to the bulk. In contrary, columns 2 and 3 have a bulk-like Y concentration, but in this case, the Zr is highly reduced. Therefore, we suggest that the intensity reduction in column 1 is produced by a different chemical composition with respect to the bulk. As Y is a lighter element that Zr, it appears darker in Z-contrast images. On the other hand, the lower intensity of columns 2 and 3 is explained by a partial occupancy of these columns, as suggested previously by E. C. Dickey et. al (*162*) for grain boundary cores. It is worth noting that the concentration of oxygen locally grows to a 70% in positions 2 and 3. However, the oxygen decreases on average in the grain boundary region, as we see in the normalized intensity results.

a)

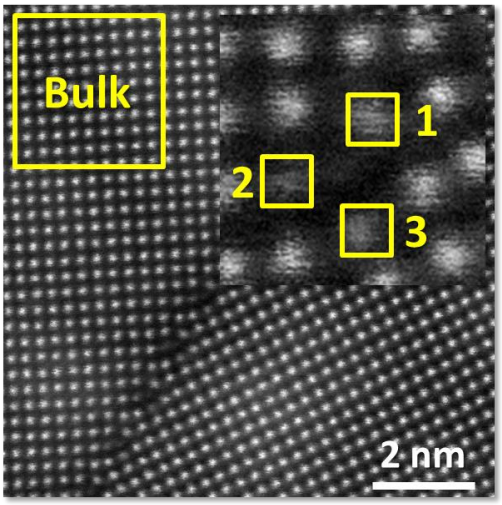

b)

Region	$[Y]_R$	$[Zr]_R$	$[O]_R$
1	12,4	27,4	60,2
2	6,3	23,4	70,3
3	6,0	22,8	71,2
Bulk	5,9	27,9	66,2

Figure 4.12: a) HAADF image of the YSZ bi-crystal grain boundary, the inset shows an amplified image of a dislocation core. The yellow squares denote the region where averaged EEL spectra were acquired. b) Table with the relative concentration values for Y, Zr and O in the regions marked in (a).

We map again the normalized intensity for zirconium, yttrium and oxygen using the high-loss *L* edges. Figure 4.13(a) shows an atomic resolution HAADF image of the region where an EEL spectrum image was acquired with a beam current of 20-30 pA, using a dispersion of 1 eV/ch and an exposure time of 0.04 seconds/pixel. The sample was tilted until both sides of the grain boundary where “on axis” to obtain atomic

resolution maps, although some channeling effect might be present. Concentration (normalized integrated signal) maps corresponding to Zr $L_{2,3}$, Y $L_{2,3}$, and O *K* edges are shown in panels (b)-(d). The maps show again compositional changes within the dislocation cores, we can appreciate that the changes are much more localized in the maps obtained using the high energy-loss *L* edges.

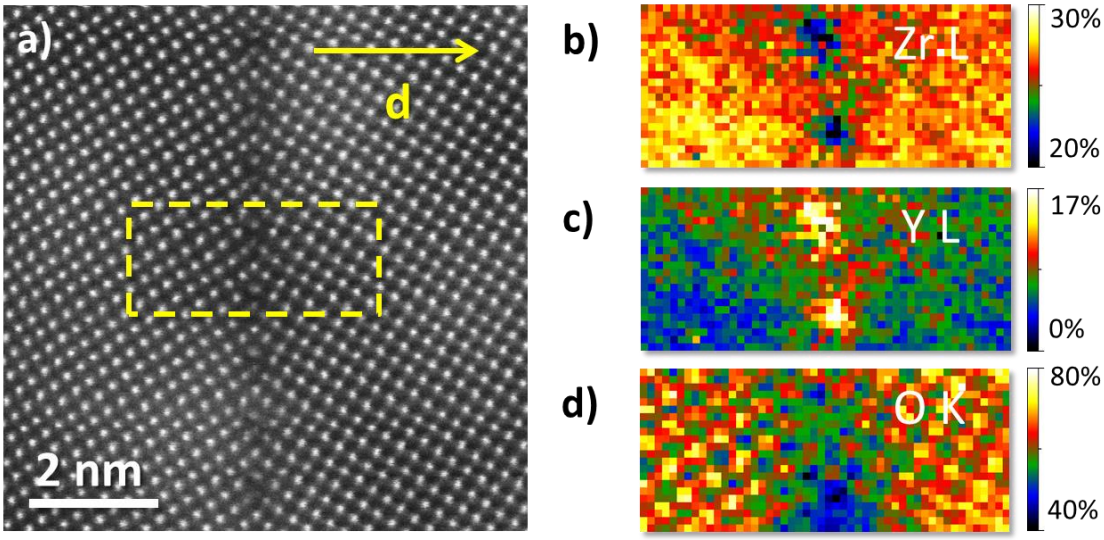

Figure 4.13: a) Z-contrast image of the grain boundary region obtained in a Nion UltraSTEM 200 operated at 200kV (a), the yellow dashed box marks the area where an EEL spectrum image was acquired. (b), (c) and (d): Atomic resolution, integrated signal maps of Zr $L_{2,3}$, Y $L_{2,3}$ and O *K* edges, respectively, normalized to the nominal bulk concentration. The exposure time is 0.1 s per pixel.

The profiles in Figure 4.14 show the concentration changes of each atomic species as a function of the distance to the boundary plane, obtained averaging the maps from Figure 4.10 and Figure 4.13. The full symbol profiles correspond to the relative quantification produced with the low-loss *M* edges, and the open symbols correspond to the high-loss *L* edges quantification. The EELS maps show a compositional non-stoichiometry around the grain boundary. More specifically, and as hinted from the images, there is an intense segregation of Y to the dislocation cores, nearly doubling the concentration in the bulk regions. There is also a strong reduction in the oxygen concentration close to the grain boundary, much more than expected from the stoichiometric value calculated from the changes in the cation concentrations (black line in the image). The length scales of these changes, especially in the case of the high-loss quantification, are in the range of 5 Å (one unit cell), as obtained from the FWHM of the EELS oxygen and yttrium compositional profiles, which agrees with the results from the dielectric spectroscopy measurements.

This finding implies that the oxygen vacancies are intrinsic to the grain boundary (structural) and result in non-stoichiometric composition. Moreover, and opposed to previous studies (*160*, *163*), there is no sign of a nanometers wide oxygen vacancy depleted space charge region, which should behave like the dark-green dashed line in Figure 4.14.

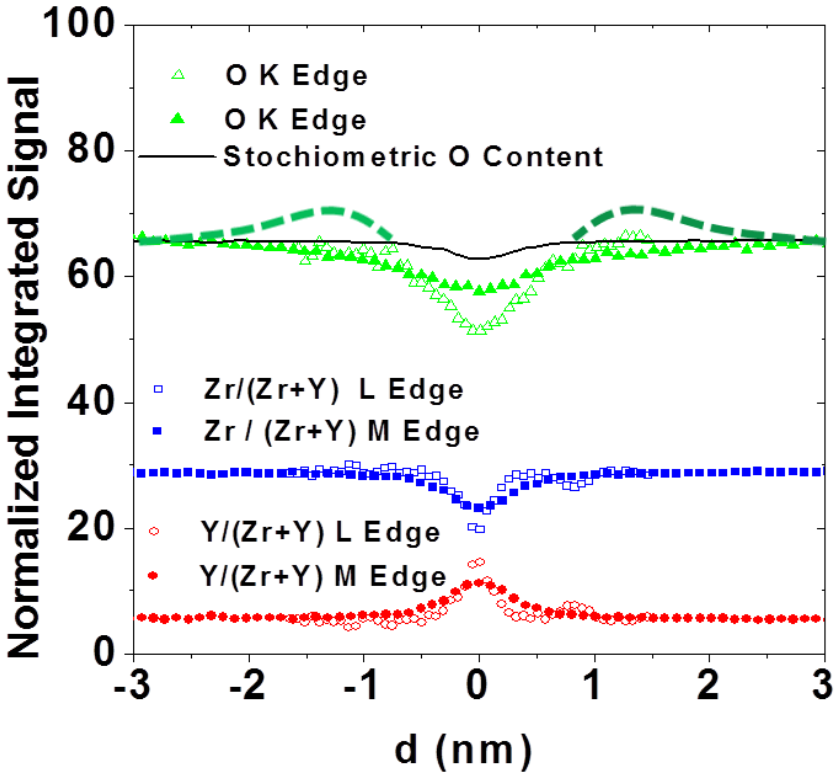

Figure 4.14: Normalized integrated signal profiles across the direction marked with an arrow in Figure 4.10(a) and Figure 4.13(a). Open symbols correspond to the analysis of the *L* edges quantification, while solid symbols result from the *M* edges. Zr and Y profiles have been normalized to the total cation concentration. The black line is the stoichiometric O content that would be expected from the measured Zr and Y signals alone. The dashed line is a guide to the eye for the excess O content to attain charge neutrality from depletion of O vacancies as expected in the conventional view.

Density functional theory calculations

Density functional theory calculations were carried out to better understand the results obtained by the ionic transport measurements and the electron microscopy characterization and provide additional information about the formation of ionic conductivity barriers at grain boundaries. For the calculations, the projector augmented-

wave method (PAW) (*164*, *165*) as implemented in the VASP code (*166*, *167*) was used. The supercell used for the calculations was an ideal fluorite ZrO_2 bicrystal with two symmetric grain boundaries. The lattice parameter chosen was 5.13 Å and the supercell total dimensions were 37.01 Å, 18.50 Å and 5.13 Å (or integer multiples of them). After removing the atomic columns inconsistent with the HAADF images, the chemical formula for the supercell was $Zr_{100}O_{200}$. We made the assumption that all the atomic columns have a full occupancy for this analysis.

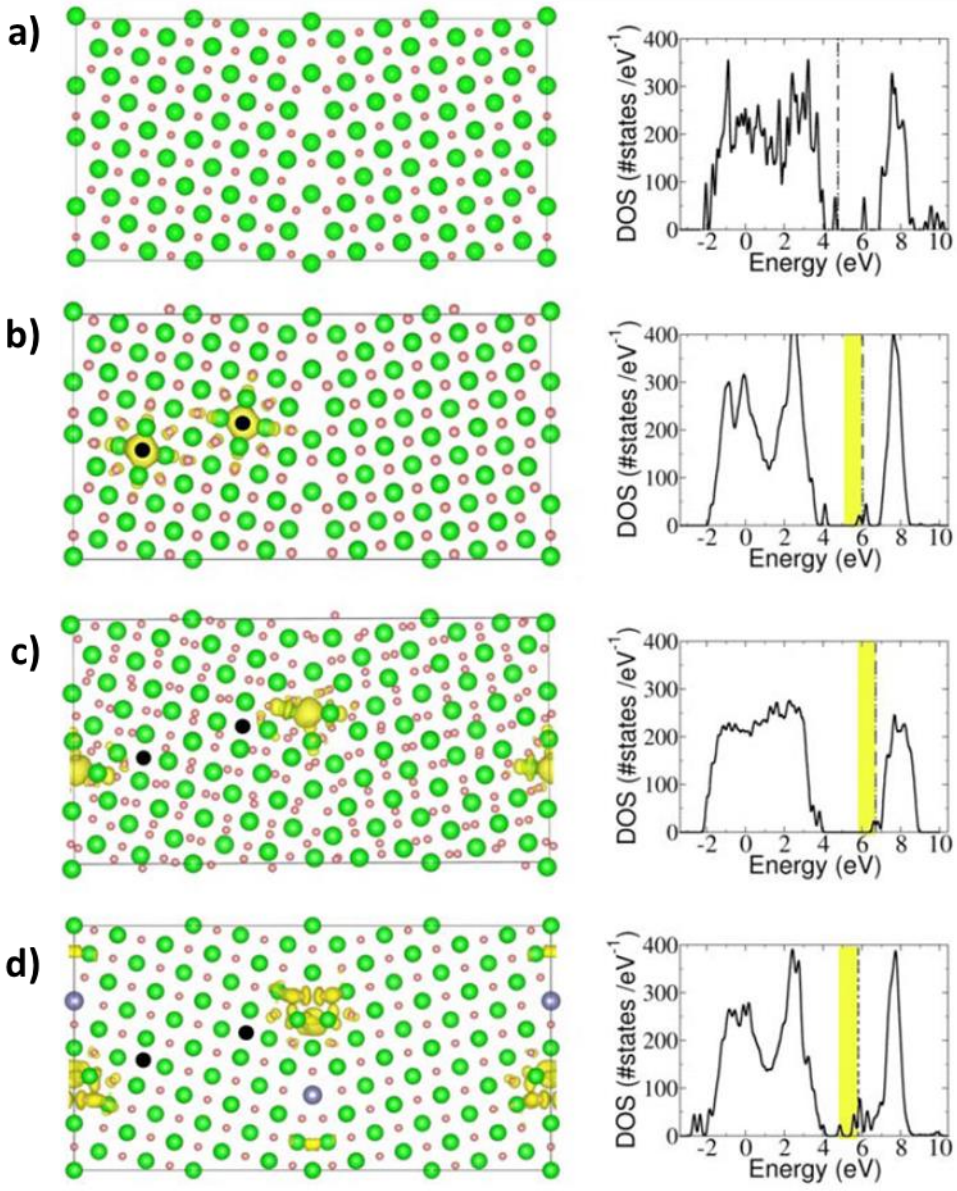

Figure 4.15: a) Model of the stoichiometric grain boundary along with the density of states (DOS). Zr atoms are represented in green and O atoms in red. The vertical line in the DOS denotes the position of the Fermi level. b) Model and DOS for a grain boundary with oxygen vacancies (black). The charge density corresponding to the electrons ceded by the oxygen vacancies is marked in yellow in both the atomic

structure and the DOS. c) Atomic structure and DOS with the same oxygen vacancies after structural relaxation. d) Same as (b) but including Y (in purple) enrichment in the crystallographic position consistent with the microscopy images.

We estimated the formation energy of oxygen vacancies in the GB region and we found that, even in the absence of Y, the presence of oxygen vacancies lowers the energy of the GB by more than 0.1 eV/Å^2 (Figure 4.15(b)). This result proves that the increase of oxygen vacancies found in the STEM-EELS results is intrinsic to the GB. Our findings show that the oxygen vacancy electrons are captured in empty electronic states in the energy gap of the grain boundary (Figure 4.15(c)), which produces a charging of the grain boundary. The charge density is represented by an isosurface of the square of the modulus of the occupied wave function with energies marked by the yellow shaded area in the left panels of Figure 4.15. The energy formation of oxygen vacancies is reduced because the extra electrons generated by the vacancy go to the energetically favorable empty states in the grain boundary, as shown in Figure 4.15(c). Further calculations show how Y segregates to the dislocation cores, as found by the STEM-EELS characterization, and moreover, probably due to the relative negative charge of Y, this segregation lowers the energy formation for oxygen vacancies and hence, enhances their concentration. It is important to note that the positive charge generated by the oxygen vacancies is not fully compensated by the segregation of yttrium ions to the grain boundary. The Y ions found by the STEM-EELS characterization act as acceptor for the extra electrons produced by the oxygen vacancies and hence, enhances the localization of the electrons in the grain boundary region (Figure 4.15(d)).

Discussion

Encouraged by the surprising dielectric spectroscopy results found by the dielectric spectroscopy analysis (*142*), we have used advanced electron microscopy techniques combined with density functional theory calculations to study the structural, chemical and electronic properties of a symmetric grain boundary in an YSZ bi-crystal. We have presented the ionic transport results, where thanks to the measurements of a single grain boundary, we can estimate the thickness of the space-charge region with great precision. We have been able to characterize the structure of the grain boundary dislocation cores at

the atomic level using high angle annular dark field images. From the strain analysis we can localize the grain boundary dislocation cores and we can disregard the presence of long range structural distortions. We have also performed a quantitative compositional analysis of the grain boundary using EELS, and we find no evidence of a nanometer thick region depleted of oxygen vacancies which would result in a space charge layer to screen a positive charge accumulation at the grain boundary, as previously believed (*129*, *141*, *151*, *152*, *168*, *169*). Quite the opposite, we find the presence of structural oxygen vacancies in a region of one unit cell at each side of the grain boundary, ensuing in a non-stoichiometric composition.

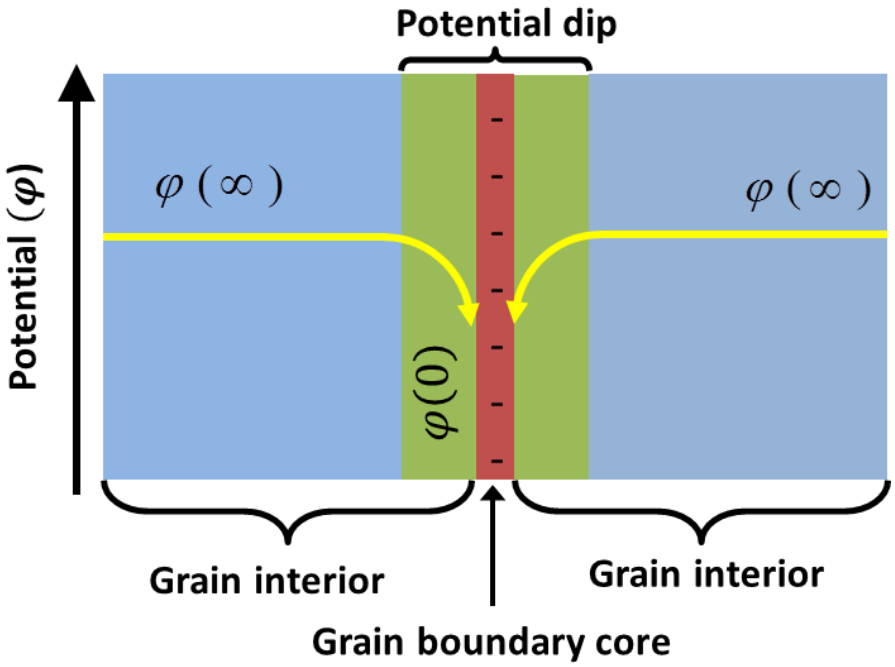

Figure 4.16: Sketch illustrating the potential dip model. The charge associated with intrinsic oxygen vacancies at the grain boundary produces a potential dip within a region of one unit cell.

From the DFT calculations, we obtain that charge neutrality is achieved when the extra electrons produced by the oxygen vacancies go to unoccupied electronic states in the energy gap at the grain boundary. They generate an electrostatic potential dip, which acts as a barrier for the ionic conductivity as shown in Figure 4.16. The oxygen vacancies arriving to the grain boundary sense an attractive potential, due to the negatively charged GB, which they have to overcome to go through, resulting in a reduction of the ionic conductivity. This study results in a step further in the understanding of ionic blocking at grain boundaries, which will serve to improve the functional properties of polycrystalline ionically conducting materials used in energy related applications. So far, we have studied

the presence and effects of small amounts of point defects, such as oxygen vacancies, almost within the detectability limits. In the next chapters, we go a step further and we will study fluctuations of the atomic columns per se. In particular, we will try to detect and analyze minor oxygen displacements in complex oxides.

Chapter 5: Oxygen Octahedral rotations in $LaMnO_3/SrTiO_3$ superlattices

This chapter shows the study of interfaces between two different materials in a heterostructure. The interfaces between the Mott insulator $LaMnO_3$ (LMO) and the band insulator $SrTiO_3$ (STO) are analyzed in epitaxially grown superlattices with different thickness ratios and different transport and magnetic behaviors. Using atomic resolution electron energy-loss spectrum imaging, we map simultaneously the structural and chemical properties of these interfaces. In previous chapters we aimed at detecting defects such as oxygen vacancies from indirect methods, such as EELS quantification. Here, we will directly image O columns using atomic resolution EELS spectrum images. We will show changes in the oxygen octahedral rotations within the $LaMnO_3$ layers when the thickness ratio between the manganite and the titanate layers is varied. Superlattices with thick LMO and ultrathin STO layers present unexpected octahedral tilts in the STO, along with a small amount of oxygen vacancies. On the other hand, thick STO layers exhibit an undistorted oxygen octahedron while the LMO layers present reduced O octahedral distortions near the interfaces. These findings will be discussed in view of the transport and magnetic differences found in previous studies.

Introduction

The physical behavior of complex oxides heterostructures is directly related to the crystal and electronic structures present at the interfaces (*17, 170*). Particularly, subtle distortions from the perfect ABO_3 perovskite structure lead to drastic changes in the behavior of these materials (*171*). Here, we study the deformations in the BO_6 oxygen octahedron around the cations and the collective tilts of this octahedral network. These distortions play an important role in the electronic functionalities of perovskite materials (*172–174*). Oxygen octahedral rotations are strongly coupled with Jahn-Teller distortions and it has been reported recently (*175*) that they may serve to tailor the functional properties in epitaxially-strained orthorhombic $LaMnO_3$. We will take advantage of a recent study in the interface between the Mott insulator $LaMnO_3$ (LMO) and the band insulator $SrTiO_3$ (STO) (*29*), and use it as a base to analyze the relation of these oxygen octahedral structural distortions and the already studied electronic and magnetic properties of this system.

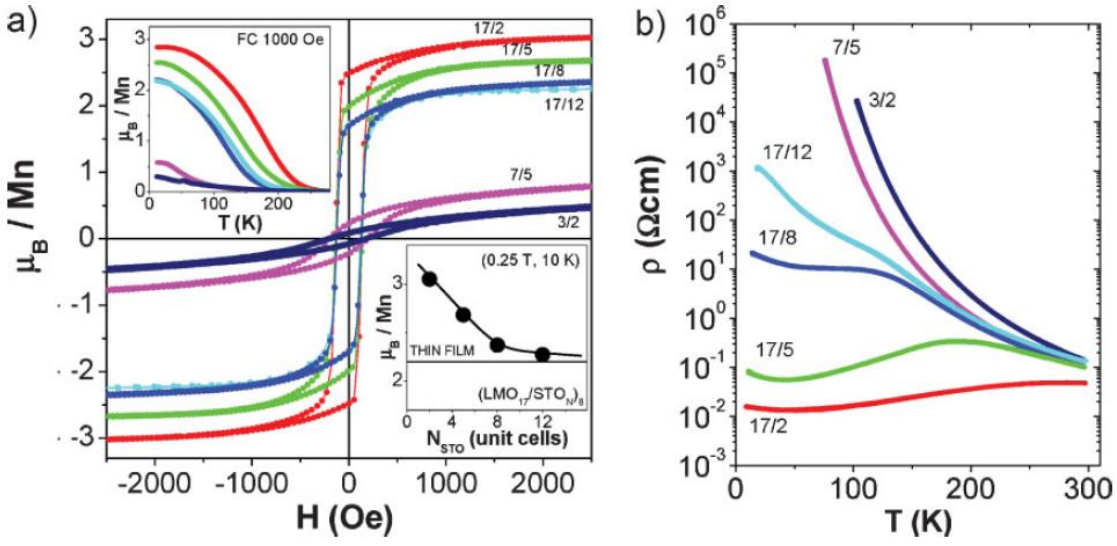

Figure 5.1: a) Hysteresis loops measured at 10 K. The n/m labels correspond to the LMO/STO layer thicknesses in unit cells. Top inset: field cooled magnetization versus temperature with an applied magnetic field of 1000 Oe. Bottom inset: Magnetization versus STO thickness of the $(LMO_{17}/STO_n)x8$ series measured at 10K and 0.25 T. The line represents the magnetization of the 22-unit-cell LMO thin film measured under the same conditions. b) Logarithmic resistivity curves of the same samples. The same label nomenclature and color code has been used in both panels. Adapted from Garcia-Barriocanal et al. (*29*)

In previous work by Garcia-Barriocanal and co-workers (*29*), it was reported that the physical properties of STO/LMO superlattices were related to structural changes driven by an epitaxial mismatch of near 2%. The epitaxial strain can be controlled by the relative thickness ratio between LMO and STO layers of the superlattice heterostructure. It was found that by varying the STO spacer thickness, and hence the epitaxial strain, the electronic and magnetic properties of the manganite layers changed, as shown in Figure 5.1. When the STO layer in STO/LMO superlattices is really thin, the LMO is relaxed and displays a ferromagnetic and conducting state. In contrast, LMO layers are partially strained when grown on top of thicker STO layers. Furthermore, they present an insulating behavior and display depressed ferromagnetism. Intriguingly, the oxidation state of the Mn, as measured by EELS (*29*), is in all cases close to +3. These findings suggest that the crystal structure changes due to epitaxial strain in $LaMnO_3$, affecting the Jahn-Teller distortion or the oxygen octahedral rotations, may be coupled with the magnetic ordering (*175*). These structural variations may explain the electronic and magnetic properties of these samples.

Here we will examine the oxygen sublattice behavior in the interfaces between LMO and STO. Since the bonds between the transition metal and the oxygen atoms control the electronic properties of these oxides, we aim to shed some light on how the details of the structural reconstruction, induced by epitaxial strain at the interface, may have an effect on the electronic coupling. To do so, we use aberration-corrected STEM and EELS to study the samples at the atomic level, focusing on the structural differences at the interfaces between LMO and STO layers in superlattices with very different thickness ratios.

$LaMnO_3$ crystalline structure

Research on manganese oxides, also known as manganites, is one of the main areas of study within strongly correlated electron systems. The interest in manganites started with the report of ferromagnetism by Jonker & van Santen (*176*) in mixed crystals of $LaMnO_3$-$CaMnO_3$, $LaMnO_3$-$SrMnO_3$ and $LaMnO_3$-$BaMnO_3$. These materials crystallize in the perovskite structure ABO_3 with the A ions (La) at the corners of the unit cell, the B ions

(Mn) occupying the center of the cube while the oxygen ions are placed at the center of the faces, as shown in Figure 5.2.

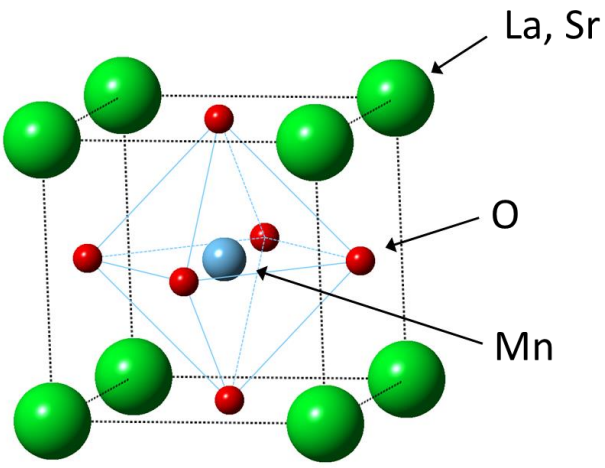

Figure 5.2: Arrangement of ions in the perovskite structure of manganites. Adapted from Dagotto et al. (*5*)

The interest in manganites reemerges in the 1990s with the experimental observation of large magnetoresistance effects (*177*, *178*) and more recently with the discovery of the so-called "colossal" magnetoresistance effect. In this chapter, we have studied the end-member compound ($LaMnO_3$) of this manganite family, while next chapter will examine other composition. At room temperature, LMO presents an orthorhombic A-type antiferromagnetic (A-AFM) and insulating *Pbnm* structure produced by the rotation of the oxygen octahedral network from the ideal perovskite structure (*179*, *180*) and a large cooperative coupling of Jahn-Teller distortion. There are two factors producing this symmetry lowering from the ideal cubic perovskite where the Mn-O-Mn angle is 180°. In LMO, lanthanum has 12 nearest oxygen neighbors at a distance of $a/\sqrt{2}$. By lowering the symmetry to trigonal, the Mn-O-Mn angle can be diverted from 180°, and lanthanum becomes irregularly 12-coordinated. The oxygen octahedra have equal Mn-O distances and are almost regular but rotated around the three-fold axis. Moreover, the Jahn-Teller distortion of the MnO_6 octahedra lowers the symmetry further to orthorhombic, where the Mn-O distances are allowed to vary (Figure 5.3). Then, it is believed that the A-AFM phase is favored by the Jahn-Teller distortion and therefore, the strong coupling between the oxygen octahedral rotations and the Jahn-Teller distortion is responsible for the stabilization of the A-AFM insulator phase.

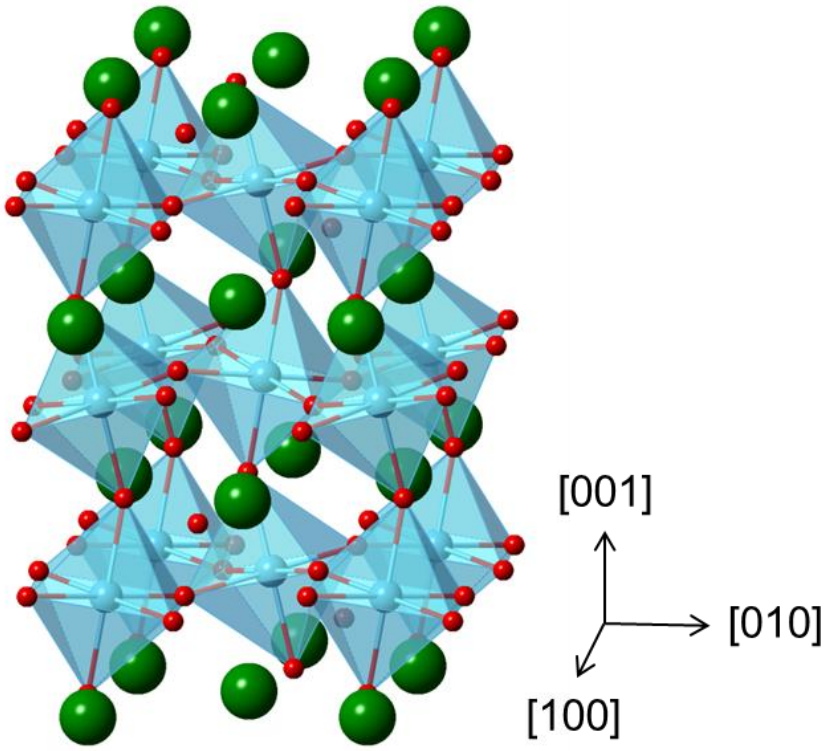

Figure 5.3: Schematic orthorhombic modification of the perovskite structure in bulk $LaMnO_3$

Epitaxial strain due to coherent matching to a crystalline substrate can change the stability of the orthorhombic A-AFM phase and favor a metallic ferromagnetic (FM-M) state, since they are energetically very close. In our case, we will consider the pseudo cubic lattice parameter of LMO as the cube root of the volume per formula unit of the relaxed A-AFM *Pbnm* structure (*175*) ($a_{LMO} = 3.976$ Å). Epitaxial growth on STO ($a_{STO} = 3.905$Å) produces a relatively large compressive strain of -1.78%. Theoretical studies show how compressive strain favors the less-orthorhombic FM-M phase with an insulator-to-metal transition at a critical strain close to -1% (*175*), thus, the metallic behavior of the superlattices studied in previous work by Garcia-Barriocanal (*29*).

Furthermore, in STO (100)-oriented layers, ($Sr^{2+}O$) planes alternate with ($Ti^{4+}O_2$) planes, which define an empty t_{2g} valence band of a band-insulating compound. In the LMO perovskite with the trivalent A-site element, ($La^{+3}O$) atomic planes alternate with ($Mn^{+3}O_2$) planes to define a half-filled e_g conduction band with carriers localized by on-site Coulomb repulsion (Mott-Hubbard insulator). Therefore, there is a breakdown in the BO_6 octahedral network at the interfaces with polar (charge) and orbital discontinuities

among different orbital symmetries which may be responsible for the sensitivity of the electronic structure to the relative layer thicknesses (*29*).

Experimental results

In this chapter we studied three different samples: we analyze a bulk LMO powder sample to obtain a reference of the oxygen octahedral rotations and compare them with the values measured in the samples of interest. These samples are epitaxial LMO/STO superlattices grown on top of STO (100) substrates with a high pressure and high-temperature (810 °C) sputtering deposition system (*81*). Two superlattices with different nominal thickness ratios were studied: LMO_{17}/STO_2 and LMO_{17}/STO_{12} unit cells (u.c.), 8 bilayer repetitions each. The characterization of the LSMO/STO superlattices was carried out using a Nion UltraSTEM100 (*80*) operated at 60 and 100kV. The probe forming aperture was 30 mrad while the EELS collection angle was 35 mrad. The EEL spectrum images were acquired with an exposure time of 0.05 seconds/pixel and a beam current around 20 pA. After acquisition, random noise in the EEL spectrum images was removed using principal-component analysis (*74*). The specimens were prepared by conventional mechanical grinding and polishing and Ar ion milling.

Structural analysis

As hinted by Garcia-Barriocanal et al. (*29*), changing the relative thickness of the STO and LMO layers in the superlattices affects the epitaxial strain in the heterostructure and consequently, it may modify the properties of the system. In order to asses this possibility, we carried out a strain analysis of the superlattices using the "Peak pairs analysis" (PPA) (*66*, *67*) algorithm available for Digital Micrograph. Figure 5.4 shows both low (a) and high (b) magnification HAADF images of a $(LMO_{17u.c.}/STO_{2u.c.})$ x 8 superlattice, the images show an epitaxial growth in all the layers. Both LMO and STO layers are flat and continuous over long lateral distances. LMO appears brighter than STO due to the higher average Z number giving rise to an enhanced Z-contrast signal in the HAADF detector.

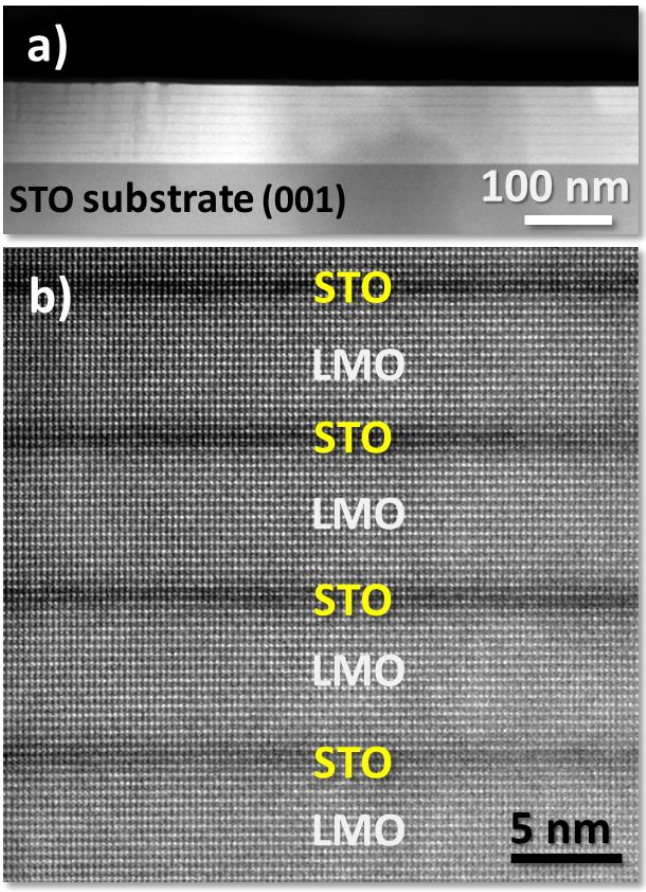

Figure 5.4: a) Low and b) high magnification high angle annular dark field images of a (LMO_{17uc}/STO_{2uc}) x 8 superlattice grown on STO (001) at 100 kV. STO layers exhibit a darker contrast, while LMO layers appear brighter.

The high magnification HAADF image used for the strain analysis of the LMO_{17}/STO_2 superlattice is shown in Figure 5.5(a). In (b) we show a map of the out-of-plane component of the strain tensor (ε_{yy}), we have used the unit cell of LMO as a reference to calculate the strain values. This map exhibits the changes in the out-of-plane lattice parameters for the different layers in the heterostructure. We can see a blue color in the regions corresponding to the STO layers, indicating a compressive strain. We observe how different layers are not strained homogeneously and some regions of the STO layers present a smaller reduction in the lattice parameter in relation to the LMO layers. It is worth noting that the values obtained for the regions close to the top and bottom borders of the image are due to an artifact of the PPA. We can overlay the strain map on top of the original HAADF image to see the strain values for each individual atomic column, as shown in Figure 5.5 (c) and (d). If we look carefully to the magnified image in (d) we observe negative values for the out-of-plane lattice parameter in the STO layer. This

compressive strain is present only in the STO layers and there is no evidence of long range strain effects along the growth direction between the LMO and the STO layers.

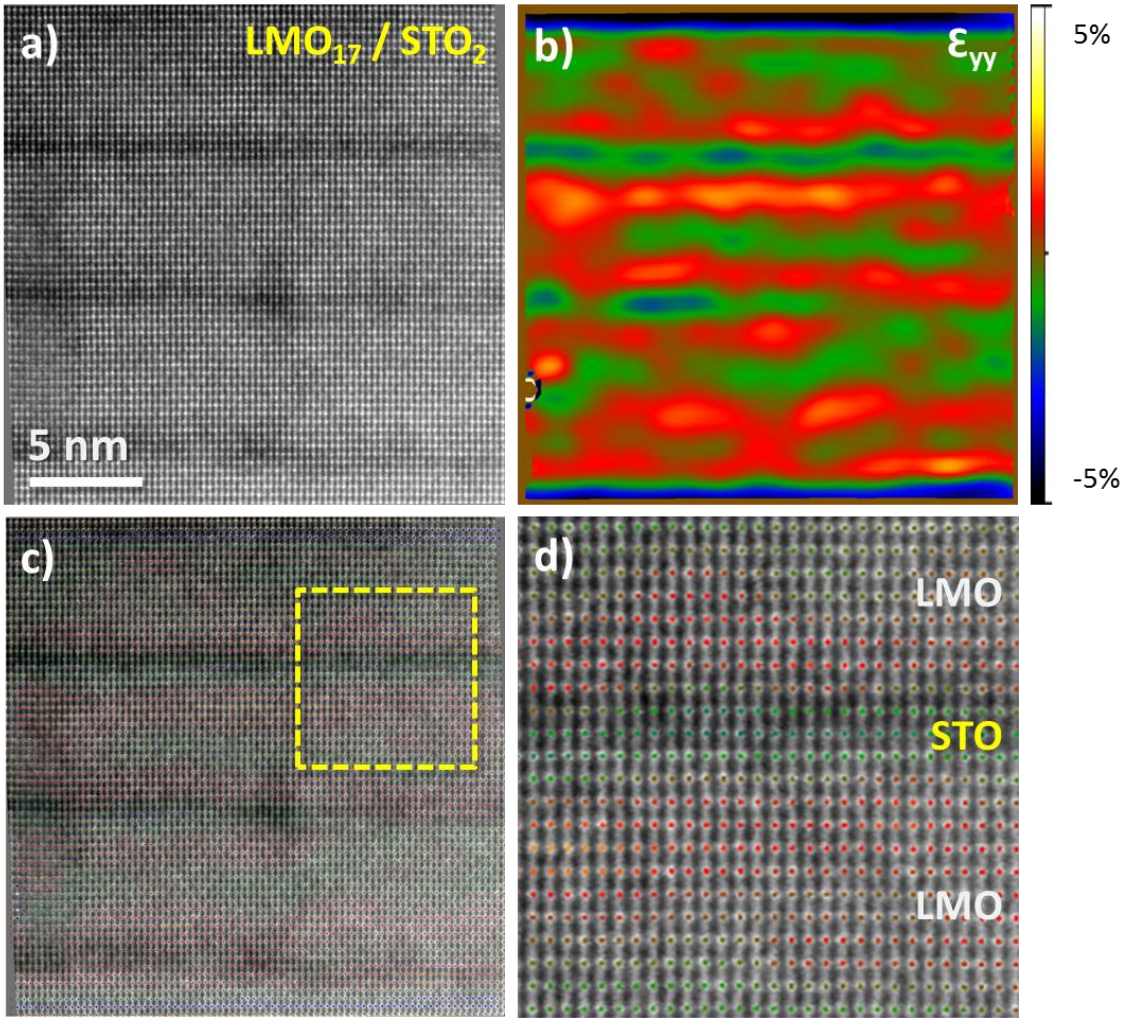

Figure 5.5: a) HAADF image of a (LMO_{17uc}/STO_{2uc}) x 8 superlattice used for the strain analysis. b) False color map of the strain tensor component in the "c" direction (ε_{yy}) from the image in (a). c) ε_{yy} map overlaid on the original HAADF image. d) Amplified image from the region marked with a yellow square in image (c) showing more clearly the strain values for each individual atomic column.

Next, we studied a superlattice with a quite distinct thickness ratio: 17 LMO u.c. and 12 STO u.c., which is still ferromagnetic but in this case, an insulating sample (*29*). Figure 5.6 shows low (a) and high (b) magnification HAADF images of a ($LMO_{17u.c.}/STO_{12u.c.}$) x 8 superlattice. The image shows an epitaxial growth in all the layers with flat and coherent interfaces over long lateral distances.

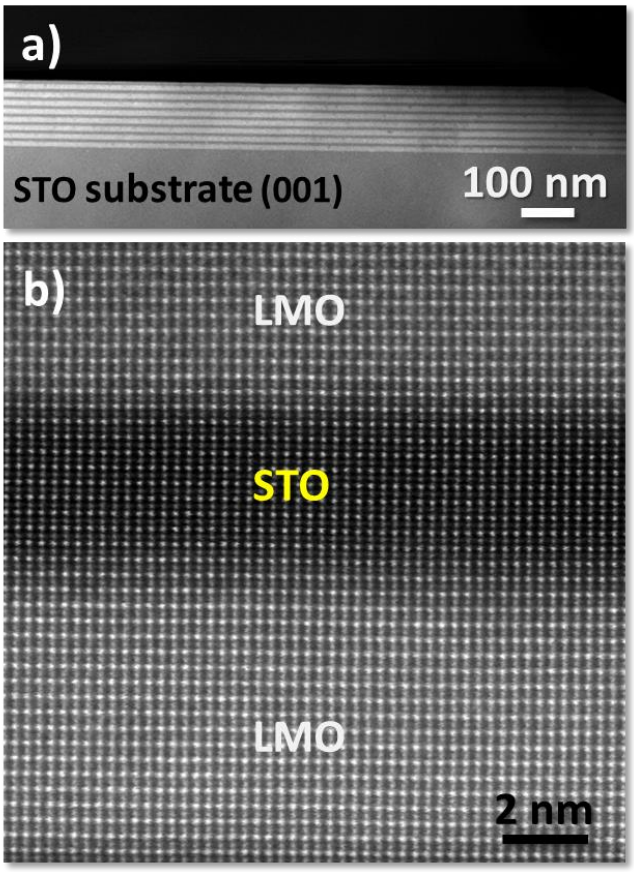

Figure 5.6: a) Low and b) high magnification high angle annular dark field (HAADF) images of a (LMO_{17uc}/STO_{12uc}) x 8 superlattice grown on STO(001), obtained at 100 kV. STO layers exhibit a darker contrast, while LMO layers appear brighter. Sample oriented down the [110] zone axis.

We performed again a strain analysis of the LMO_{17}/STO_{12} superlattice using the PPA algorithm for Digital Micrograph (*66*, *67*). As in the previous analysis, we used the LMO unit cell as a reference for the strain analysis. In Figure 5.7(b) we show the ε_{yy} strain component map, where the different colors (strain values) for the LMO and the STO layers are appreciable. If we overlay the strain map to the original HAADF image as shown in (c), we can notice that the regions with different contrast colors (green/red) do not match exactly with the interfaces between the different layers (LMO/STO), meaning that there is an inhomogeneous strain propagation from one layer to the other. The first atomic planes of the STO layers present a tensile strain, matching the out-of-plane lattice parameter of the LMO layer. This strain is released through the layer, and the top atomic planes exhibit a reduction in the lattice parameter and a relaxation of the tensile strain coming from the LMO layer. Moreover, the LMO layer exhibits a similar behavior: the 3 – 4 first atomic planes on top of the STO layer are strained to the STO lattice parameter

(presenting a green color), and the LMO lattice parameter is recovered after these atomic planes.

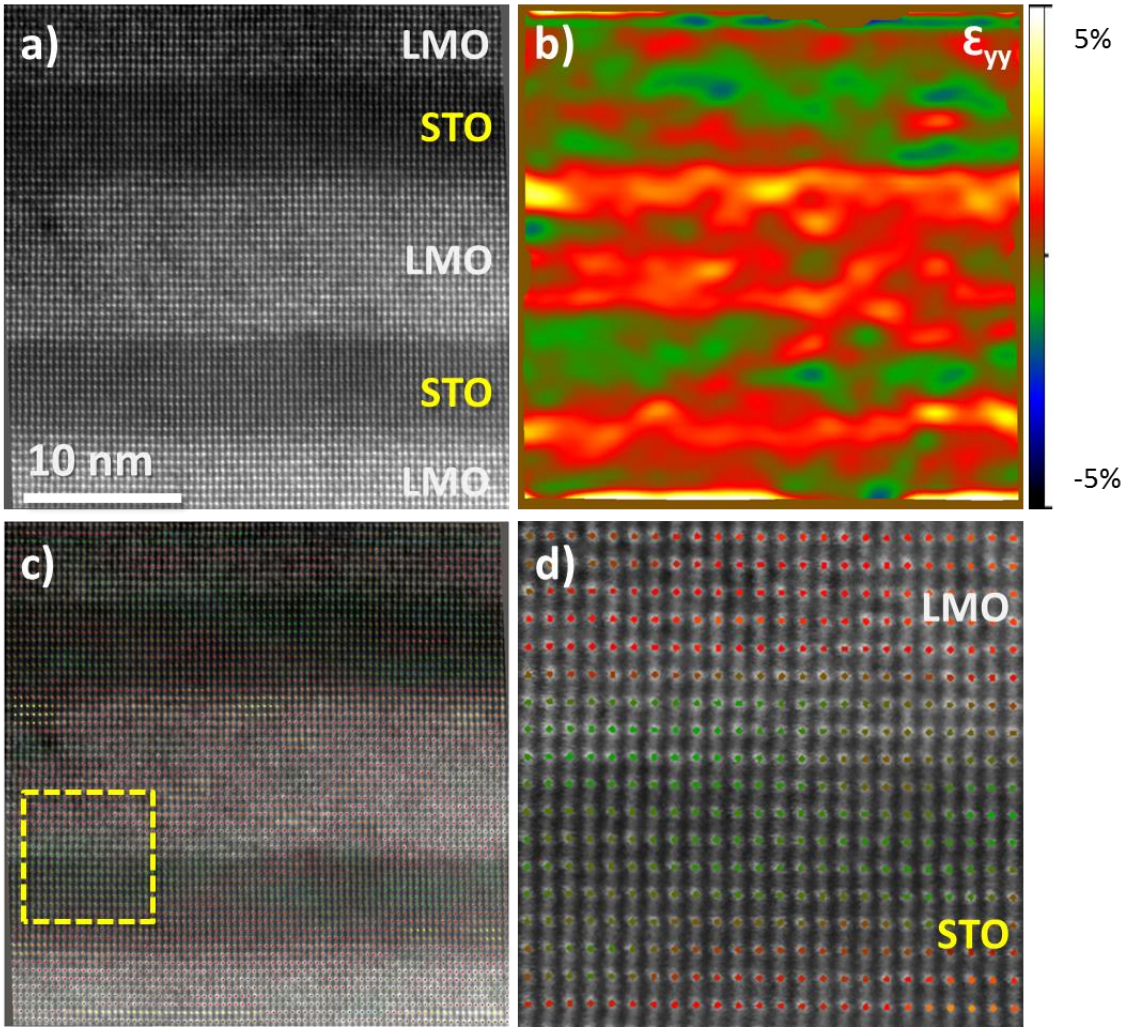

Figure 5.7: a) HAADF image of a (LMO_{17uc}/STO_{12uc}) x 8 superlattice used for the strain analysis. b) Map of the strain tensor component in the "c" direction (ε_{yy}) from the image in (a). c) ε_{yy} map overlaid on the original HAADF image. d) Amplified image from the region marked with a yellow square in image (c) showing more clearly the strain values for each individual atomic column. Sample oriented down the [110] zone axis.

We have confirmed the existence of different behaviors in structural trends resulting from epitaxial strain for the two chosen thicknesses ratios, as was suggested by Garcia-Barriocanal et al. (*29*). In the case of the LMO_{17}/STO_2 superlattice, we find no evidence of a structural distortion produced by strain in neither the LMO nor STO layers. However, the superlattice with thicker STO layers exhibits some degree of propagation of the strains from the STO into the LMO layer. This difference may be responsible for the

measured transport and magnetic properties in these samples. In order to further study the extent in the structural differences between these samples we will study the local crystal structure in the form of the oxygen octahedral rotations in both specimens.

Oxygen octahedral rotations in $LaMnO_3$ bulk

In order to carry out our analysis, we need a reference of the oxygen octahedral distortions in LMO. For this aim, we studied the structure of bulk LMO crystals, and measured the oxygen octahedral rotations in the bulk material. We used a Nion UltraSTEM200 operated at 200 KV to study the bulk sample. This microscope is equipped with an annular bright field detector with an angle detector range from 10-20 mrad, which is very sensitive to light atoms as oxygen (*44*) and give us the precision needed for this reference study. A LMO single crystal was crushed in ethanol. The resulting solution was placed in a carbon grid and loaded in the microscope.

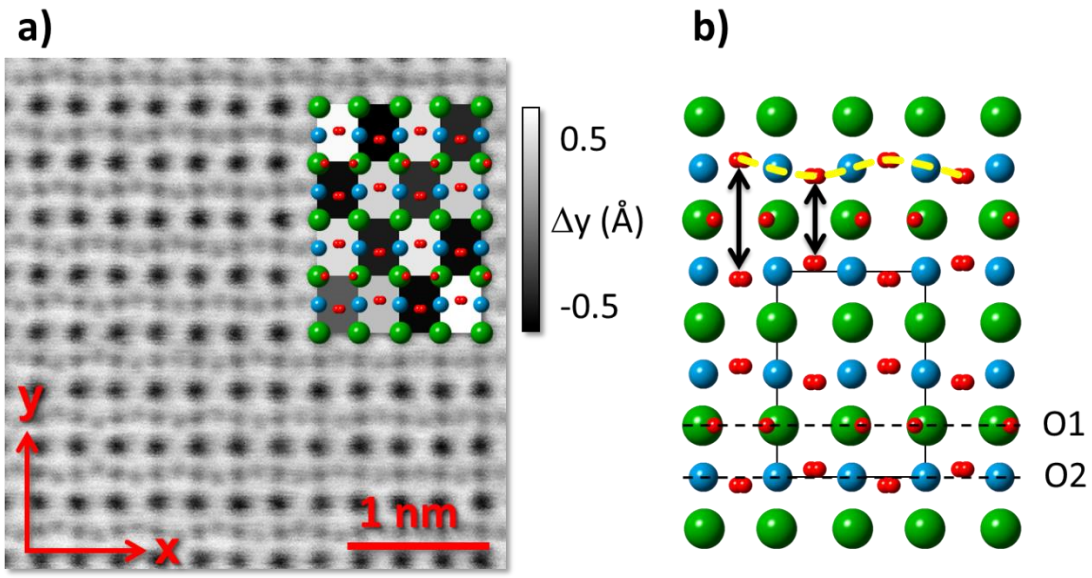

Figure 5.8: a) ABF image of a bulk $LaMnO_3$ crystal down the [110] direction. The inset shows the oxygen octahedral tilt map in Å. Each pixel corresponds to the difference in vertical displacements from a given O atom and the adjacent O first neighbor within the O2 plane. b) $LaMnO_3$ crystal structure from neutron scattering data (*181*) showing La (green), Mn (blue) and O (red) atom positions. Black dashed lines show the different oxygen planes (labeled O1 and O2). A yellow line highlights the ripple in the O2 plane, for visual clarity. Adapted from ref. (*182*).

Figure 5.8(a) shows an ABF image of a bulk LMO sample down the pseudo-cubic [110] direction. Figure 5.8(b) shows a model of the LMO structure from neutron scattering data (*181*). We have labeled the O atoms in the LaO plane as O1, while O2 atoms will be the O atoms in the MnO_2 plane (both planes are marked with black dashed lines). A yellow dashed line highlights the ripple within the O2 plane due to the octahedral tilts, for clarity. The arrows placed in the model highlight the noticeable difference in the distances along the vertical *(y)* direction between O2 atoms in adjacent planes, due to the octahedral rotations. The ripple can be quantified from the images by assigning a pair of coordinates (x_i, y_i) to each O column within every O2 plane. To obtain these values, we map the oxygen atomic positions from the ABF image with an iterative process locating the center-of-mass of every column (*62*, *64*), as explained in the experimental techniques chapter. Through this procedure, adjacent O atoms within a given O2 plane will exhibit a relative vertical offset of $\Delta y = (y_{i+1}-y_i)$. The inset in Figure 5.8(a) shows the calculated Δy differences for an area of the ABF image. Each pixel corresponds to one unit cell, and the crystal structure is drawn on the Δy image for clarity. The results exhibit a familiar "checkerboard" pattern, previously reported in other oxides (*63*), which illustrates the antiphase behavior of the in-plane tilts in LMO. In the model from neutron scattering data, this difference is close to 0.6 Å, similar to the values obtained from the bulk LMO ABF image (around 0.5 ± 0.1 Å). Previous studies of bulk LMO samples in the [110] direction already showed the "ripple" distortion in the oxygen sub-lattice (*183*). Once we have obtained the reference values from the analysis of the ABF images for the oxygen octahedral tilts in bulk LMO, we now use EELS atomic resolution imaging to study the samples of interest. EEL spectrum imaging is a more powerful technique since it allows simultaneous studies of chemistry and electronic properties through fine structure analysis.

Octahedral rotations in $LMO_{17\ u.c.}$ / $STO_{2\ u.c.}$ superlattices

Figure 5.9 shows a HAADF image of the superlattice with 17 u.c. of LMO and 2 u.c. of STO, which is both ferromagnetic and metallic (*29*). The layers are fully epitaxial and the interfaces are flat and coherent, as reported previously by Garcia-Barriocanal and coworkers. The yellow square marks the area where an EEL spectrum image was acquired with an exposure time of 0.05 seconds/pixel and a beam current around 20 pA.

In Figure 5.9(b), we show the O *K* edge integrated signal, where the oxygen atomic lattice from the LMO/STO/LMO interfaces region is resolved. Some spatial drift is present. It is worth mentioning that only the pure O columns in the MnO_2 plane are visible. O atoms on the heavy La-O or Sr-O atomic columns are invisible due to dynamical diffraction (*77*). We also perform a quantification of the O concentration relative to the *3d* metals (Mn, Ti) from the EELS data using the routines available in the Gatan Digital Micrograph software. These routines may not be completely accurate in the presence of dechanneling, but we can comment on general trends and qualitative changes observed in relation to the structural distortions measured. This quantification process yields a slight O depletion around 3% in the atomic plane in the middle of the STO layer (very likely, this value is slightly underestimated due to the reduced ADF signal on the STO layers). This deficit points to the presence of a small amount of O vacancies.

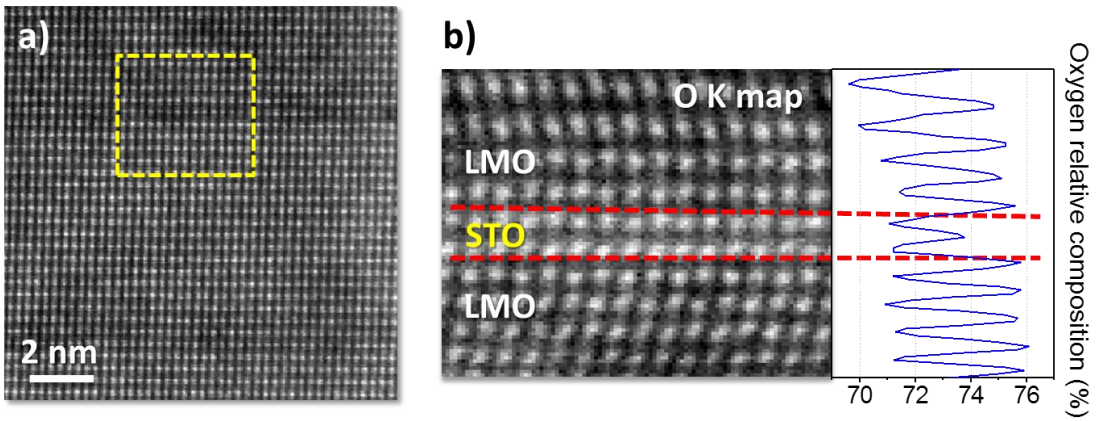

Figure 5.9: a) HAADF image of a LMO_{17}/STO_2 superlattice. The yellow square shows the region where the spectrum image was acquired. b) Oxygen *K* edge map obtained from the area marked in (a) showing the STO thin layer, obtained through integration of the edge signal after background subtraction using a power law. The interfaces are marked with red lines. Some spatial drift is present. The oxygen relative composition profile is presented on the right end, in a matching scale. This concentration has been calculated relative to the 3d metals (Mn and Ti) using the Digital Micrograph quantification routines.

To measure the oxygen octahedral tilts, we mapped the atomic column positions from the O *K* edge map in Figure 5.10(a) with the same process used in the ABF image from Figure 5.8. For an accurate calibration of the spectrum images, we used the annular dark field (ADF) image acquired simultaneously with our EEL spectra. The resulting oxygen atomic column coordinates are represented in Figure 5.10(b) with red crosses. Figure 5.10(c) shows a map for the oxygen sublattice ripple within the O2 plane, the values

measured fluctuate slightly around 0.35 – 0.55 Å with maximum absolute values close to 0.6 Å in the LMO layers, in good agreement with the ABF image analysis and the structure deduced from neutron scattering (*181*) in bulk LMO samples. We have averaged the absolute values from Figure 5.10(c) for each atomic plane in Figure 5.10(d) (error bars correspond to the standard deviation within each atomic plane) to show more clearly the behavior along the different layers: in both top and bottom LMO layers, the average ripple value (around 0.5 Å), is close to the bulk value. Interestingly, in the STO layer (region marked in red) instead of finding the flatness expected for a cubic material, we observe that the oxygen octahedra are also tilted, with an average vertical ripple value of $\Delta y = 0.2$ Å.

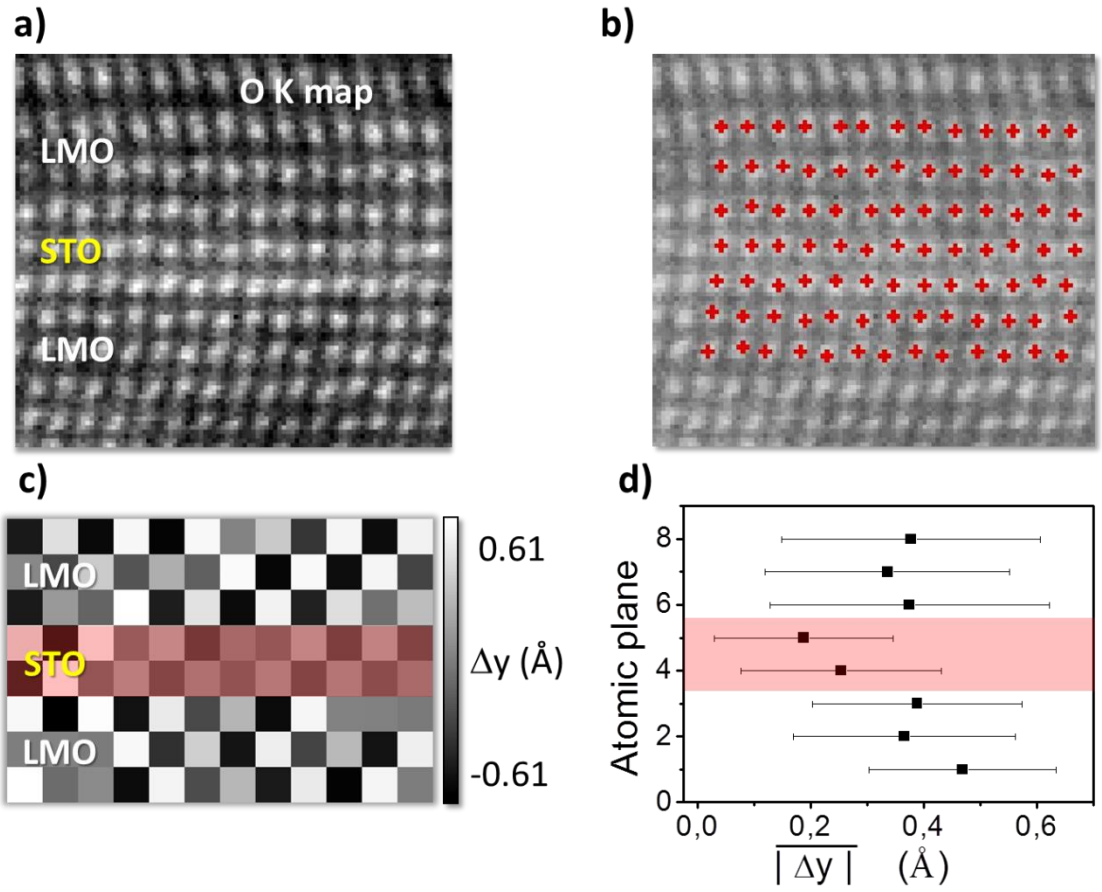

Figure 5.10: a) Oxygen *K* edge map obtained from the area marked in Figure 5.9 showing the STO thin layer, obtained through integration of the edge signal after background subtraction using a power law. The interfaces are marked with red lines. Some spatial drift is present. b) Oxygen columns positions measure from the O *K* edge map in image (a). c) Oxygen octahedral tilt map in Å, from the area marked in (b). Each pixel corresponds to the difference in vertical displacements from a given O atom and the adjacent O atom within the O2 plane. The red shadowed region corresponds to the STO layer d) Averaged oxygen distortion values from (c) along the LMO/STO/LMO layers. A red rectangle marks the location of the STO layer.

These relatively large octahedral tilts imposed in the STO layer by the proximity of LMO may be possible due to the presence of the oxygen vacancies found by EELS relative composition quantification. Indeed, it has been reported that oxygen vacancies may induce oxygen octahedral rotations in STO (*184*). This result agrees also with the findings from (*29*) where a reduction of the Ti oxidation state was measured in the LMO/STO superlattices with thinner STO spacers, which could also imply the presence of oxygen vacancies.

Octahedral rotations in $LMO_{17\ u.c.}$ / $STO_{12\ u.c.}$ superlattices

In Figure 5.11 we show an STO/LMO interface region. In the HAADF image of Figure 5.11(a), STO and LMO layers are clearly distinguished thanks to the Z-contrast, where the STO layer appears darker and the LMO layers are brighter. The yellow square indicates the acquisition region for the EEL spectrum image. Figure 5.11(b) shows the O *K* edge integrated intensity map from the STO/LMO interface, which is marked with a red dashed line. The spectrum image was acquired with 0.05 seconds/pixel acquisition time and some spatial drift is observed. In this case, the quantification of oxygen concentration (relative to Ti/Mn) results in a relatively flat oxygen content across the interfaces (Figure 5.11(b)). Only a slightly higher O concentration can be detected within the STO layer (1-2%). This finding is an artifact due to the reduced scattering to high angles in the lighter STO material (ensuing in a higher intensity going forward into the spectrometer than when the electron probe is placed on the heavier LMO layer).

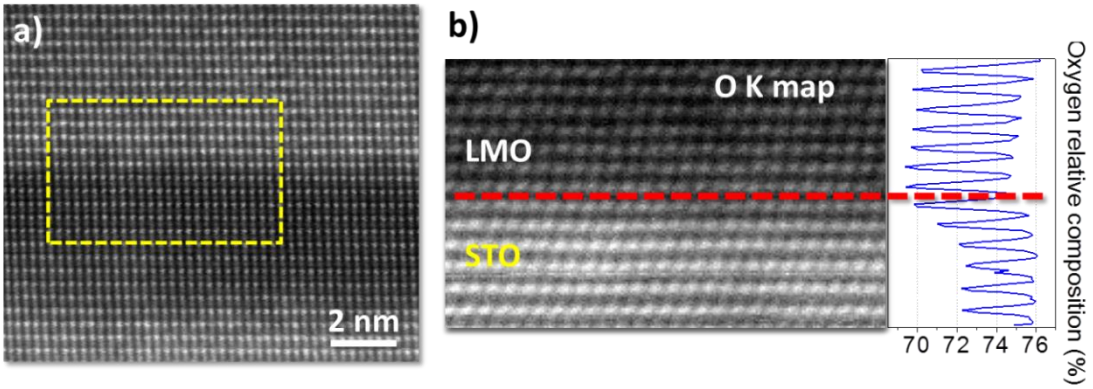

Figure 5.11: a) HAADF image of an interface in a LMO_{17}/STO_{12} superlattice. The yellow square shows the region where the spectrum image was acquired. b) Oxygen *K* edge map obtained from the area marked in (a) showing the STO/LMO interface, marked with a red line. The oxygen relative composition profile is presented on the right end, in a matching scale. This concentration has been calculated relative to the 3d metals (Mn and Ti) using the Digital Micrograph quantification routines.

Figure 5.12 shows the oxygen octahedral tilts analysis for the oxygen map in Figure 5.11(b). Figure 5.12(c) shows how in the STO layer there is no appreciable contrast between different unit cells (pixels). However, the "checkerboard" pattern, associated with tilted octahedra, is recovered again in the LMO layer. The average ripple is plotted in Figure 5.12(d). This figure confirms how towards the middle of the LMO layer (top) the structure is bulk-like, with values similar to those in the LMO_{17}/STO_2 superlattice. However, the O ripple values decrease to around 0.2 Å within the four LMO planes right on top of the thick STO layer (shadowed in red), indicating a depression of the octahedral tilts. Interestingly, these atomic planes from the LMO layer presenting a reduced tilting of the oxygen octahedral rotations coincide with the atomic planes that exhibit a compressive strain, as shown in Figure 5.7. This change could be related to the difference in the transport and magnetic properties of these samples. No distortion is found in the STO layer (within the noise), as one would expect in a cubic system.

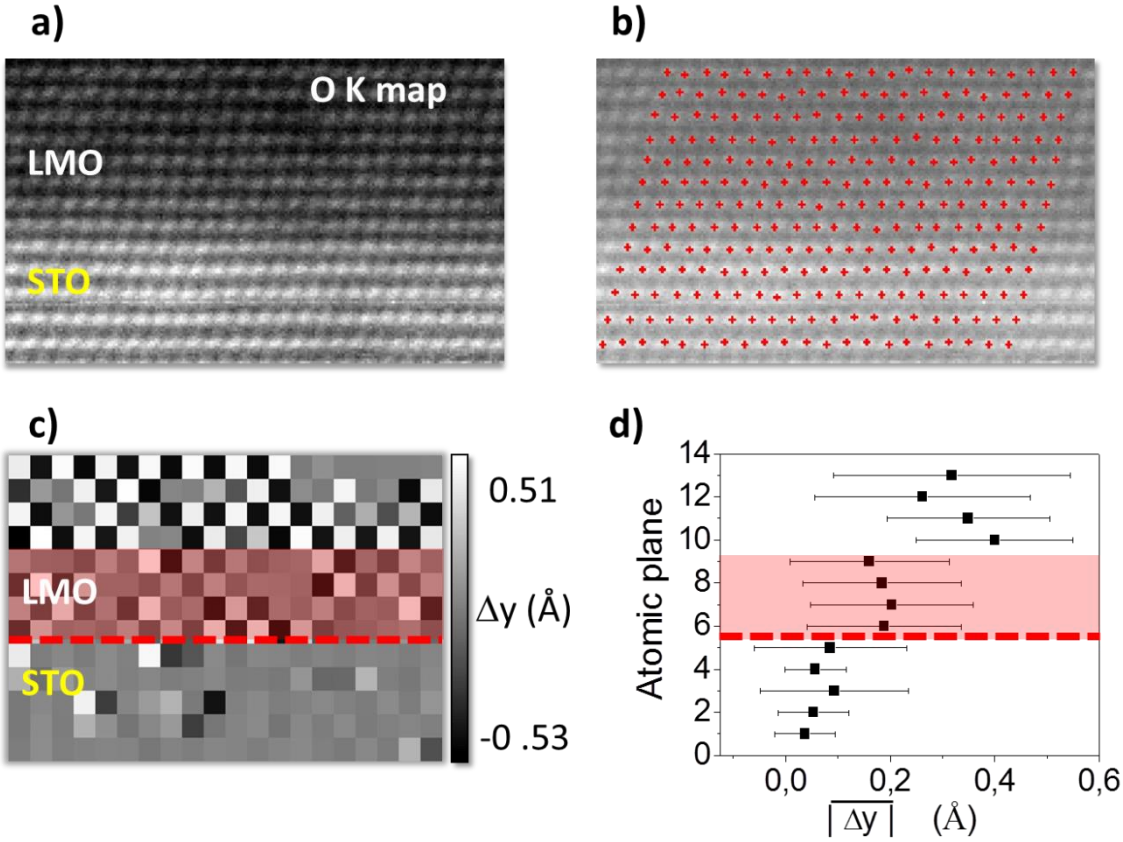

Figure 5.12: a) Oxygen *K* edge map obtained from the area marked in Figure 5.11 showing the STO/LMO interface. b) Oxygen column positions measured from the O *K* edge map in image (a). c) Oxygen octahedral tilt map in Å extracted from the O *K* edge map in (b). Each pixel corresponds to the difference in vertical displacements between any given O atom and the adjacent O atom within the O2 plane. d) Averaged oxygen distortion values from (c) along the STO/LMO interface showing a decreased octahedral rotation in the first four planes of the LMO layer (marked in red).

Discussion

By means of aberration-corrected STEM-EELS we have studied two LMO/STO superlattices with different thickness ratios (17/2 and 17/12), which present different transport and magnetic properties. From the electron microscopy results, we can relate the different oxygen octahedral tilts maps obtained by EELS in our samples with their electronic properties. From the results in (*29*), we know that the samples have completely different magnetic and electrical properties: the superlattice with the thinner STO spacer (2 unit cells) is conducting and strongly ferromagnetic, while the sample with thicker STO layers (12 unit cells) is insulating and shows a reduced magnetic moment. Conductivity in the superlattices with ultrathin STO layers may be related to a small

amount of oxygen vacancies (≈3%) and also the presence of "charge leakage" in these symmetric systems (*29*). The results from the EEL spectrum imaging and the strain analysis point to a possible relation between the oxygen octahedral rotations and the strain found in the layers. In the LMO_{17}/STO_2 superlattice, the LMO layers (with a relaxed structural state) exhibit pronounced, bulk-like octahedral tilts and the STO layer presents a distorted structure with oxygen octahedral rotations. On the other hand, in the LMO_{17}/STO_{12} superlattice, we find no oxygen ripple in the STO layers. Instead we detect that the LMO atomic planes closer to the interface exhibit smaller octahedral tilts and a compressive strain produced by the thicker STO spacers. These differences in the structural distortions of relaxed and strained LMO layers may play a role in the different magnetic and transport behaviors of these samples. There have been several studies on the effects of strain and structural distortions on the electronic and magnetic properties of LMO thin films. In some of them relaxed LMO thin films are found to be metallic and ferromagnetic (*185, 186*), while strain may drive a phase transition to an insulating state with residual ferromagnetism, which is consistent with our results. It has also been predicted theoretically (*175*) that compressive strain favors the less orthorhombic FM-M phase, where the oxygen octahedral rotations are depressed, which is at odds with our findings. Therefore, further studies are still needed to fully understand the effects of structural distortions in the electronic and magnetic properties of LMO thin films. We have shown in this chapter how atomic resolution STEM-EELS is a powerful technique when it aims to mapping minor atomic displacements, imaging light atoms and simultaneously studying composition. In the next section these techniques will be applied together with the analysis of the electronic state to the study of a most relevant system: multiferroic tunnel junctions.

Chapter 6: Resonant tunneling transport through confined electronic states in multiferroic heterostructures

Ferroelectric thin films hold the key to future non-volatile memories, logic elements or energy-related devices. Success of future applications relies on harnessing ferroelectric domains under applied electric and magnetic fields. In this chapter, we study the interfaces between two materials with different ferroic orders in a multiferroic tunnel junction. We measure the magnetotransport properties of the junctions, finding a novel behavior: oscillations in the differential tunneling conductance. Using aberration corrected electron microscopy we study the structural and electronic properties of the system which will explain the origin of these features. We use the HAADF and ABF detectors to analyze the structural properties of the samples, measuring the ferroelectric displacements unit cell by unit cell. The structural study is combined with the analysis of the electronic state in the ferroelectric layer provided by EELS. Our findings will explain how the oscillations in the tunneling conductance appear due to a resonant tunneling transport through discrete unoccupied states in a charged ferroelectric domain wall.

Introduction

One of the most promising research lines in complex oxides stems from the possibility to grow high quality heterostructures combining materials with very different physical properties, such as different ferroic orders (ferroelectrics, ferromagnets, flexoelectrics). For example, ultrathin ferroelectric layers can be used as active tunneling barriers in magnetic tunnel junctions, allowing the coupling between these two different order parameters. This kind of heterostructure is referred to as a multiferroic tunnel junction, in which four resistance states result from the (in plane) parallel or antiparallel relative alignment of magnetization vectors of the magnetic electrodes for each (out of plane) direction of the polarization vector in the ferroelectric barrier (*187*). This coupling could expand the possibilities for data storage or enable complex logic operations (*188–191*). The incomplete screening of polarization charges by metallic electrodes sandwiching a thin ferroelectric layer can stabilize a ferroelectric state down to the sub-nanometer thickness range (*192*). Furthermore, electronic asymmetries at both interfaces can yield large changes of the tunneling electroresistance upon polarization switching (*191*, *193*, *194*) of small ferroelectric domains with polarization vectors parallel to the (uncharged) domain walls. In this chapter we show that charged domain walls (with polarization vectors perpendicular to the wall) in ultrathin ferroelectric barriers within multiferroic tunnel junctions provide a path for a novel form of resonant transport through confined electronic states. This result is an experimental realization of the visionary concept of domain walls as an active part of future electronic devices (*195–197*) extending their functionalities to the design and control of novel forms of confined electronic transport. G. Catalan et. al. (*195*) introduced recently this concept of the domain wall serving as the actual device, suggesting that the local physical properties and dynamics of the domain walls themselves can provide an additional degree of freedom in order to tune the properties of future devices.

The presence of unexpected charged domain walls has already been proposed to explain the ferroelectric properties of oxide heterostructures (*198*). Here, we report a novel ferroelectric state associated with charged domain walls in ultrathin $BaTiO_3$ layers in multiferroic tunnel junctions. We show how the wall itself provides confined electronic states which give rise to resonant tunneling between the metallic electrodes. Our aim in

this chapter is to study the local polarization in combination with the electronic and chemical properties in a series of multiferroic heterostructures composed of ferromagnetic $La_{0.7}Sr_{0.3}MnO_3$ and ferroelectric $BaTiO_3$. We have made use of the ABF detector in the electron microscope to measure the local polarization in every unit cell of our ferroelectric layer, identifying the position of all atomic species, including light atoms as oxygen. Combining these structural displacements with the electronic properties found by EELS and DFT calculations we have expanded our study of the system, understanding the origin of the head-to-head charge domain wall and its correlation with the resonant tunneling transport across the ferroelectric barrier.

$La_{0.7}Sr_{0.3}MnO_3$

During the 1990s, there was a renaissance in the study of manganites due to the discovery of the giant magnetoresistance effect (*177*). Considerable emphasis was given to the analysis of $La_{1-x}Sr_xMnO_3$ compounds since the Curie temperature may be above room temperature with the proper doping level. This characteristic drastically increases the chances for the practical applications of this family of complex oxides. The phase diagram and resistivity vs. temperature for this compound at several dopings are shown in Figure 6.1 (a) and (b) respectively (*199*). In this chapter we have used the $La_{0.7}Sr_{0.3}MnO_3$ (LSMO) compound. For this doping level, the bulk Curie temperature is T_C = 369 K, the material is metallic, the saturation magnetization is M_S = 3.7μB/at_{Mn} and the low temperature resistivity is $\rho = 8 \times 10^{-5}$ Ω cm. Another important property of LSMO is that it is a half-metallic ferromagnet as demonstrated by spin-resolved photoemission experiments (*200*). The minority spin conduction band is empty, so the material has 100% spin polarization at low temperature. This property is also related to the magnetization saturation of LSMO at low temperatures since it matches well the spin value expected from all *3d* electrons present in manganese ions: $M_S = 0.7 \times Mn^{3+}(S = 4/2) + 0.3 \times Mn^{4+}(S = 3/2) = 0.7 \times 4\mu_B + 0.3 \times 3\mu_B = 3.7\ \mu_B$ (*201*).

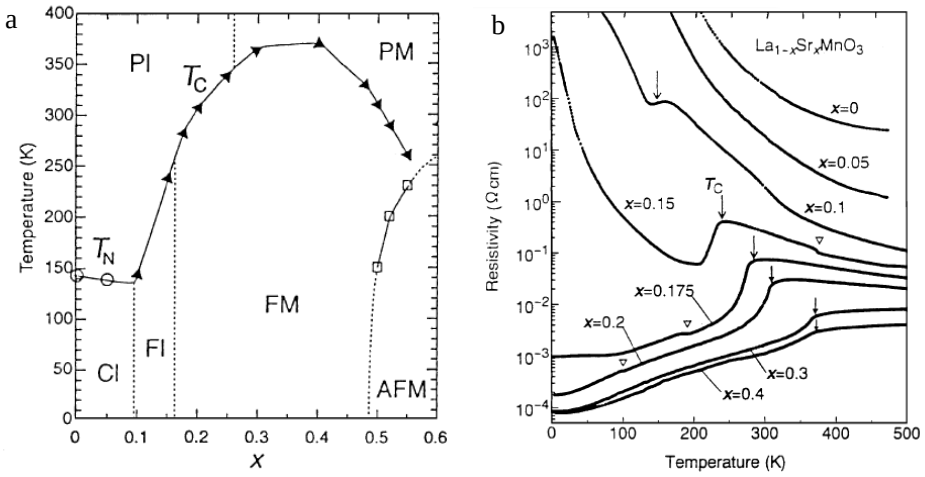

Figure 6.1: (a) Phase diagram of $La_{1-x}Sr_xMnO_3$. The AFM phase at large x is an A-type AF metal with uniform orbital order. PM, PI, FM, FI, and CI denote paramagnetic metal, paramagnetic insulator, FM metal, FM insulator, and spin-canted insulator states, respectively. T_C is the Curie temperature and T_N is the Neel temperature. (b) Temperature dependence of resistivity for various single crystals of $La_{1-x}Sr_xMnO_3$. Arrows indicate the Curie temperature. The open triangles indicate anomalies due to structural transitions. Adapted from refs. (*199*) and (*202*).

A structural study of a LSMO crystal as a function of temperature shows that it is a rhombohedral perovskite above and below T_C. The lattice parameter is $a = 3{,}876$Å and $\alpha = 90.46º$ at room temperature (*203*). When LSMO is grown as a thin-film on a cubic substrate, the unit cell is distorted and it adopts a pseudocubic structure (*204*). However, upon distorting the unit cell, the ratio between the in-plane (*a*) and out-of-plane (*c*) lattice parameters becomes important for the magnetic properties of the manganite. In Figure 6.2, the effect of epitaxial strain (*c/a* ratio) on the orbital order and consequently on the magnetotransport properties of LSMO thin-films of different compositions is shown. In this phase diagram the F region (orbital-disordered) is ferromagnetic and metallic, while the C ($3z^2$-r^2 ordered) and A regions (x^2-y^2 ordered) are insulating (*7*, *204*).

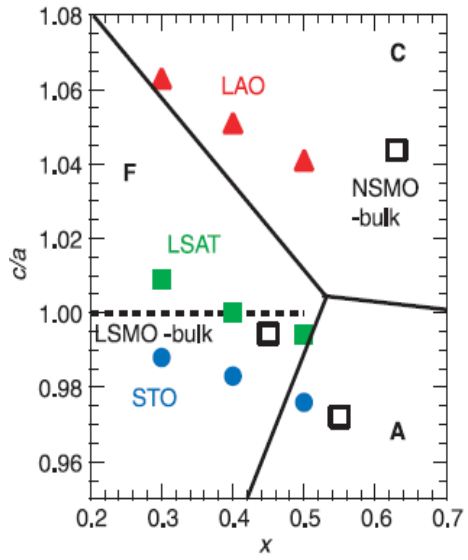

Figure 6.2: The schematic phase diagram in the plane of lattice strain c/a and doping level x. The data labeled LAO, LSAT, and STO represent the results for coherently strained epitaxial thin-films of $La_{1-x}Sr_xMnO_3$ grown on perovskite single-crystal substrates: $LaAlO_3$, (La, Sr)(Al, Ta)O_3, and $SrTiO_3$, respectively. LSMO-bulk and NSMO-bulk stand for results for the bulk single crystals of $La_{1-x}Sr_xMnO_3$and $Nd_{1-x}Sr_xMnO_3$, respectively. Adapted from (*203*).

Another relevant issue related to LSMO thin-film growth is the existence of a so-called "dead layer" or critical thickness that can be defined as the thickness above which the material remains both metallic and ferromagnetic. In different studies this dead-layer thickness for thin-films was estimated to be a few nanometers depending on the substrate chosen. For thin-films grown on STO, the LSMO dead layer thickness is estimated to be about 8 u.c. (*205*). The mechanism behind the dead layer problem, and its existence itself, is still controversial. The electronic phase-separation phenomenon at the LSMO/STO interface, where ferromagnetic insulating and metallic phases segregate within length scales of a few nanometers, is one of the possible explanations (*5*). Scanning tunneling spectroscopy (*206*) and ferromagnetic resonance (*207*, *208*) support this scenario. Another possible origin of the dead layer is an orbital reconstruction at the LSMO/STO interface. It has been proposed that a strain induced distortion of the MnO_6 octahedra leads to crystal-field splitting of the e_g levels and lowers the $d_{3z^2-r^2}$ orbital over the $d_{x^2-y^2}$ orbital resulting in a local C-type antiferromagnetic structure at the interface (*15*).

$BaTiO_3$

The discovery in 1949 of ferroelectricity in the simpler, non-hydrogen-containing perovskite oxide barium titanate dramatically changed the physical understanding of this phenomenon. $BaTiO_3$ is the prototypical example of a now very large and extensively studied perovskite oxide family. $BaTiO_3$ (BTO) is band-gap insulator with ferroelectric behavior at room temperature. At high temperature, it has a paraelectric cubic perovskite structure ($Pm\bar{3}m$) with lattice parameters: $a = b = c = 4.0$ Å. At the Curie temperature $T_c = 393\,K$, it suffers a phase transition to a ferroelectric tetragonal phase ($P4mm$) with $a = b =$ 3.987 Å, and $c =$ 4.040 Å. The ferroelectric tetragonal phase of BTO has a saturation polarization of $Ps = 0{,}26\,C/m^2$. This phase remains stable until 278 K, where there is a second transition to a ferroelectric phase with orthorhombic symmetry and $Ps = 0{,}33\,C/m^2$, and a third transition at $T = 183\,K$ to a rhombohedric structure with $Ps = 0{,}33\,C/m^2$ (*209*). These phase transitions involve small atomic displacements, dominated by the displacement of the Ti ion relative to the oxygen octahedron network (as shown in Figure 6.3), and a macroscopic strain. There is also a change in the alignment of the polar axis in each phase, changing from the <100> in the tetragonal phase, <110> for the orthorhombic and <111> in the rhombohedric phase.

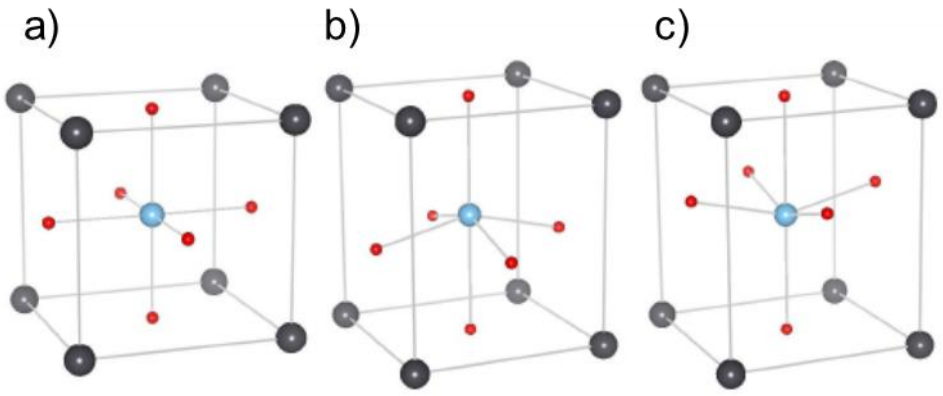

Figure 6.3: Crystal structure of the ferroelectric perovskite $BaTiO_3$. (a) High temperature paraelectric cubic phase. (b and c) Room-temperature, ferroelectric tetragonal phases for the polarization pointing up (b) and down (c). The displacements are scaled to be clearly visible. Adapted from ref. (*210*).

Ferroelectricity in perovskite oxides can exhibit a high sensitivity to changes in strain state, typically produced by external stress. Bulk ferroelectric properties can be enhanced in BTO thin-films using strain engineering (*211*). Figure 6.4 shows the expected T_C for

(001) $BaTiO_3$ under biaxial in-plane strain. The blue region represents the paraelectric phase and the yellow one, the ferroelectric phase. The intermediate green region shows the dispersion introduced in the prediction of T_C from the differences in the reported parameters used in the thermodynamic analysis. This study (*211*) implies that a compressive strain of only 1% should increase the BTO thin film T_C to values comparable to unstrained $Pb(Zr,Ti)O_3$ films. Biaxial compressive strain may increase the transition temperature by nearly 500°, and give rise to a remanent polarization at least 25% higher that the bulk. Such compressive strain supposes a constraint for the ferroelectric polarization in BTO, forcing the unit cell to expand in the out-of-plane direction and enhancing the tetragonallity. This effect assures the alignment of the ferroelectric polarization in the c-axis.

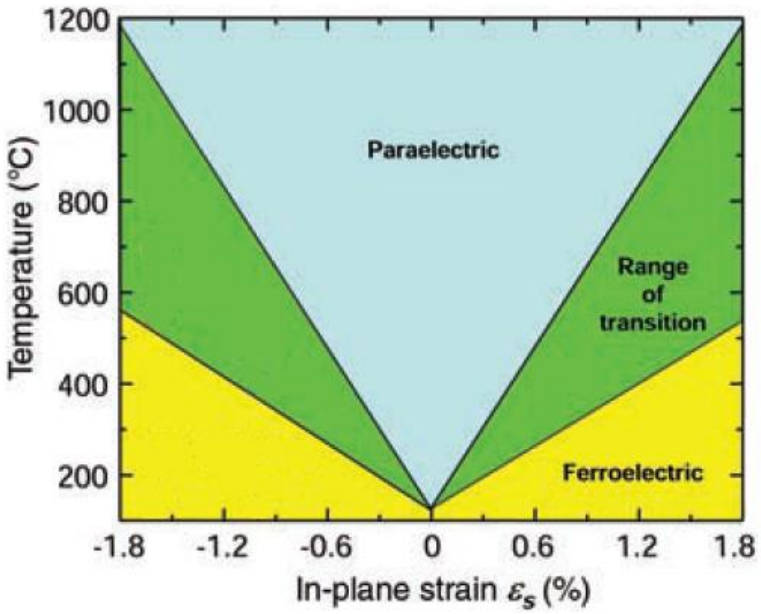

Figure 6.4: Predicted Curie temperature (T_C) of (001) $BaTiO_3$ under biaxial in-plane strain, based on thermodynamic analysis. Adapted from (*211*).

Therefore, strain engineering plays a key role to reduce the ferroelectric critical thickness, which is necessary in order to implement ferroelectric layers as active tunnel barriers in multiferroic tunnel junctions. In the case of BTO, the critical thickness has been reported to be in the range between 12 to 1 nm (*192, 212–215*). Gruverman *et al.* (*189*) have shown ferroelectricity in 2.4 nm thick BTO films, and growing highly strained BTO on LSMO/$NdGaO_3$, V. Garcia *et al.* reduced the critical thickness limit down to 1.2 nm (*188*). Moreover, the incomplete screening of polarization charges by the metallic

electrodes in a multiferroic tunnel junction (as in our case) helps stabilizing the ferroelectric state in nanometers thick ferroelectric barriers. When doping BTO with electrons (for example by introducing oxygen vacancies), ferroelectricity should be quenched because itinerant electrons screen the long range Coulomb interactions. Nevertheless, these electrons partially stabilize ferroelectricity due to the screening of the strong crystal perturbation caused by oxygen vacancies (*216*). In fact, ferroelectric displacements have been observed in oxygen reduced conducting BTO (*217*), and first-principles calculations have shown that the ferroelectric instability in BTO requires only a short-range portion of the Coulomb interactions of the order of the lattice constant, below a critical doping concentration n_c = 0.11 e/u.c. (*218*). It is important also to notice that, although these levels of doping may appear high, BTO is known to retain its ferroelectric groundstate with charge densities in excess of 2 10^{21} cm^{-3} (*218*). Doping BTO with electrons below this critical concentration may enhance the range of functionalities, opening opportunities for doped ferroelectrics in novel electronic devices.

Experimental results

The samples studied in this chapter are ultrathin epitaxial $LSMO_{60u.c.}/BTO_{11u.c.}/LSMO_{18u.c.}$ trilayers and $LSMO_{15u.c.}/BTO_{11u.c.}$ superlattices grown on top of STO (100) substrates. The growth was carried out using a high O_2 pressure (3.2mbar) and high-temperature (750 °C) sputtering deposition system (*81*). Transport measurements were carried out in tunnel junctions fabricated using standard UV optical lithography and ion milling from the trilayer samples. The samples were patterned into micron size (9x18 μm^2 and 5x10 μm^2) rectangle shape pillars and silver electrodes were evaporated to measure perpendicular transport. X-ray diffraction (XRD) measurements have been carried out using a Philips X'pert MRD diffractometer located at CAI de Difracción de Rayos-X (UCM). STEM-EELS characterization was done using an aberration-corrected NionUltraSTEM200 operated at 200 KV. EEL spectrum images were also obtained using a Nion UltraSTEM100 (*80*) operated at 60 KV. The probe forming aperture was approximately 30 mrad while the EELS collection semi-angle was 48 mrad. Random noise in the EEL spectrum images was removed using principal-component analysis (*74*). The specimens for the microscopy characterization were prepared by conventional mechanical grinding and polishing and Ar ion milling.

Transport measurements

We measured the tunnel junction resistance as a function of magnetic field swept in a hysteresis loop sequence. Several devices from different samples with identical tunneling barrier thicknesses were measured at different temperatures. In Figure 6.5(a) we show the resistance versus magnetic field sweeps measured at 14 K and with an applied voltage of 800mV. The long side of the rectangular junction was aligned with the [110] easy axis in order to improve antiparallel alignment of the magnetization vectors for top and bottom LSMO electrodes. The resistance shows abrupt jumps at magnetic field values corresponding to the reversal of the magnetization direction of the electrodes. The positive sign of the tunnel magnetoresistance found is expected for this junction as LSMO is a half-metal with positive spin polarization (*219*). We measured I(V) curves in the parallel and antiparallel states to better characterize the spin-dependent transport mechanism. Figure 6.5(b) shows a non-linear behavior, expected for a tunneling transport mechanism. We observe that the current for the parallel state is higher than for the antiparallel state for the whole voltage range, which results in positive tunnel magnetoresistance.

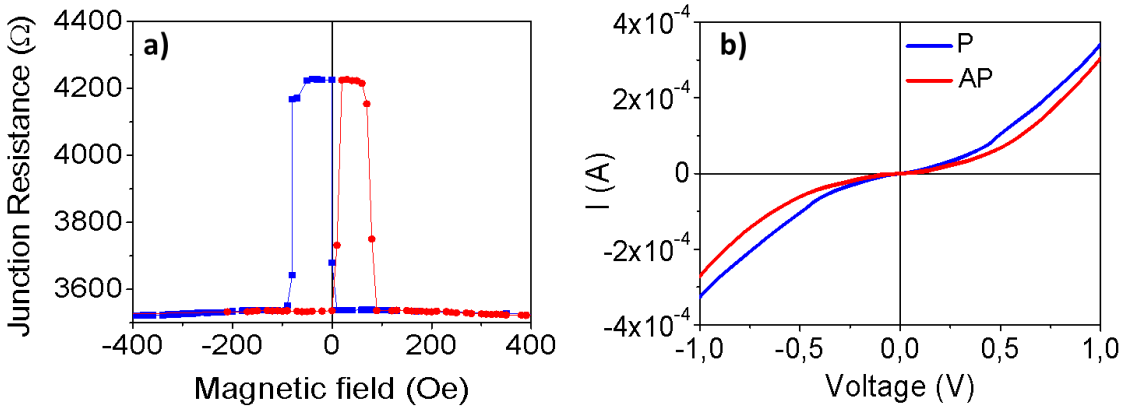

Figure 6.5: a) Junction resistance versus applied magnetic field sweeping from 4200 Oe to -4200 Oe (blue) and from -4200 Oe to 4200 Oe (red) at 14 K measured at 800 mV. b) Tunneling current as a function of applied bias at parallel (blue curve) and antiparallel (red curve) magnetic state at 14 K.

We have obtained the tunneling differential conductance as the numerical derivative of the I(V) curves. As we see in Figure 6.6(a), it exhibits pronounced oscillations in both

the parallel and antiparallel states, which is at odds with the expected parabolic dependence of the conductance of a tunnel junction with the voltage at low bias (*220*). Thus, the oscillations we observe could indicate a resonant tunneling transport through discrete unoccupied states in the ferroelectric barrier. These quantum oscillations fade out when temperature is increased and they also disappear when a large voltage is used to switch the ferroelectric polarization, indicating that the feature responsible for the presence of confined electronic states in the barrier can be removed by a strong polarizing electric field. This feature could consist of mobile defects or structural distortions affecting the local electronic properties or perhaps a domain wall as already hinted by Han et al (*198*). One way or the other, the energy separation of the conductance oscillations at low temperatures, $\Delta E=70 - 90$ meV, reflects the possibility of the presence of a strongly confined electronic states in extremely narrow regions within the ferroelectric layer. In the following we will show that in fact, the oscillations can be described by a 2D electron gas confined by a triangular potential well. In order to get further insights into the nature of this resonant tunneling state in the ferroelectric barrier, techniques capable of studying structure, chemistry and electronic properties with atomic resolution in real space are essential. We will use advanced electron microscopy, combined with density functional theory calculations to study this system in depth.

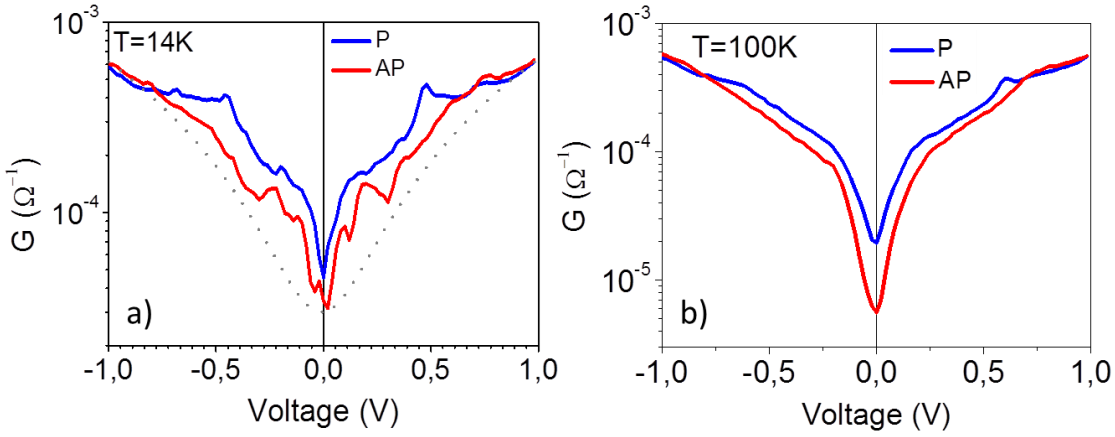

Figure 6.6: a) Differential conductance obtained as the numerical derivative of current vs. voltage at parallel (blue curve) and antiparallel (red curve) magnetic state at 14 K. b) Differential conductance measured at 100 K.

Structural characterization

We investigated a series of specimens of LSMO/BTO heterostructures grown on top of $SrTiO_3$ (100) substrates consisting on trilayers composed of $LSMO_{60u.c.}/BTO_{11u.c.}/LSMO_{18u.c}$ and superlattices with two bilayers of $LSMO_{15u.c.}/BTO_{11u.c.}$. First, we analyzed the structural properties of these samples, using both X-ray diffraction and HAADF images to study the epitaxial growth quality and EELS to analyze the elemental distribution and the terminations between the different layers.

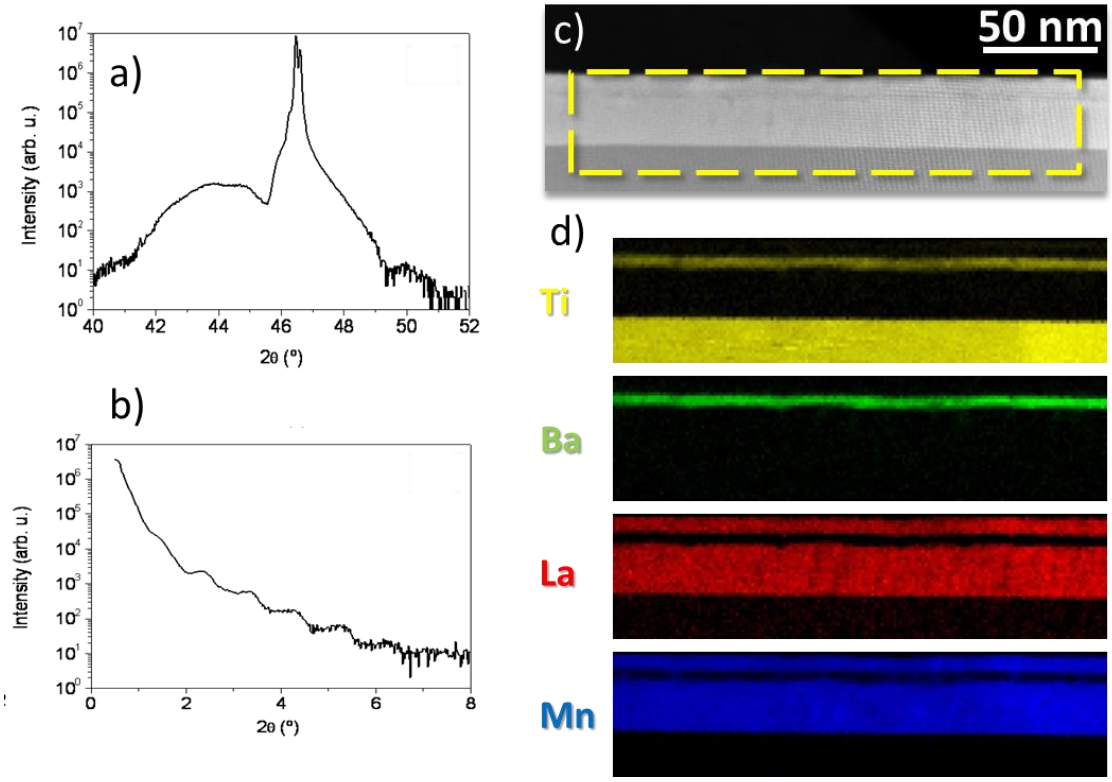

Figure 6.7: a) X-ray diffraction spectra and (b) X-ray reflectivity of a BTO/LSMO bilayer. c) Low magnification HAADF image of a LSMO/BTO/LSMO trilayer showing the region where a spectrum image was acquired. d) EELS chemical maps showing the Ti $L_{2,3}$, Ba $M_{4,5}$, La $M_{4,5}$ and Mn $L_{2,3}$ edges integrated intensities.

Figure 6.7 shows the structural characterization of a LSMO/BTO/LSMO trilayer grown on top of a (001) STO substrate. Bulk BTO lattice parameters for the tetragonal phase are $a = b = 3.987$ Å and $c = 4.040$ Å while STO has $a = b = c = 3.905$ Å. Hence, epitaxial BTO films on STO suffer a 2.06% biaxial compressive strain along the *a*

and *b* axes. The displacement towards lower angles of the (002) diffraction peak in (a) indicates an enlargement of the *c* lattice parameter due to this constrain. In addition, the reflectivity spectrum exhibits finite size oscillations, indicating the smoothness of the surface. In (c) a low magnification HAADF image shows the heterostructure, where the different layers are hardly noticeable due to the small difference in Z number between these materials. Nevertheless, we can observe a very flat surface indicating a planar growth. In order to appreciate more clearly the different layers, we used EELS to map the different chemical species in our specimen. Figure 6.7(d) shows the integrated intensity below the Ti $L_{2,3}$, Ba $M_{4,5}$, La $M_{4,5}$ and Mn $L_{2,3}$ edges after background subtraction using a power law fit. From these images we can observe how there is no major interdiffussion across the interfaces and that the layers are flat and continuous over long lateral distances.

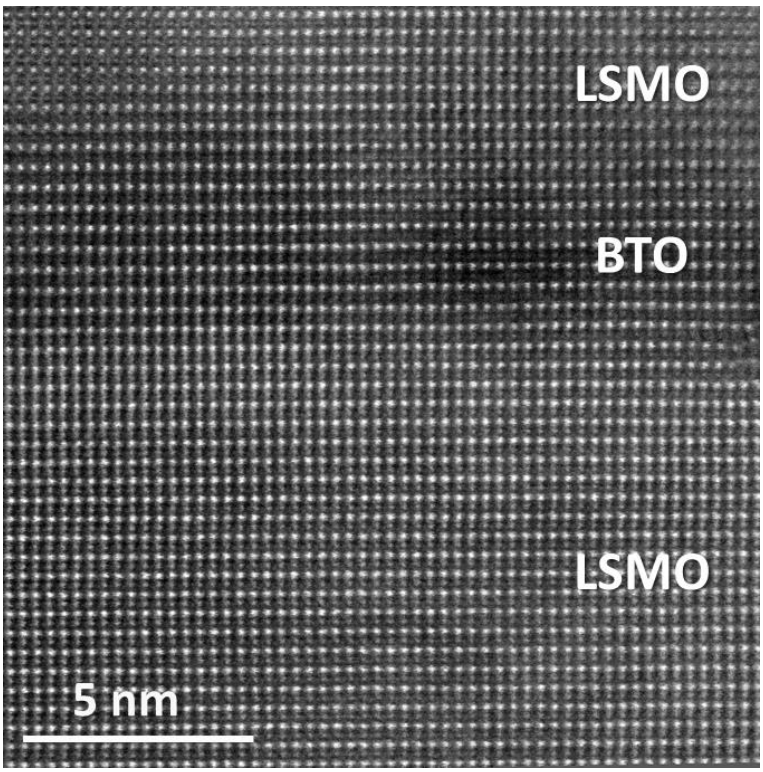

Figure 6.8: High magnification HAADF image of a LSMO/BTO/LSMO trilayer down the (110) orientation showing the epitaxial growth of each layer.

The high magnification HAADF image from Figure 6.8 exhibits the high structural quality of the sample. The growth is perfectly epitaxial and the different layers appear fully strained to the in-plane lattice parameter of the STO substrate. Such strain supposes a constraint for the ferroelectric polarization in the BTO layer. The in-plane compressive strain forces the unit cell to expand in the out-of-plane direction, pinning the ferroelectric

polarization to align preferentially along this axis (*221*). There is very little contrast between the different materials in the image so we acquired high magnification EEL spectrum images to identify the exact position of each layer and the atomic plane terminations.

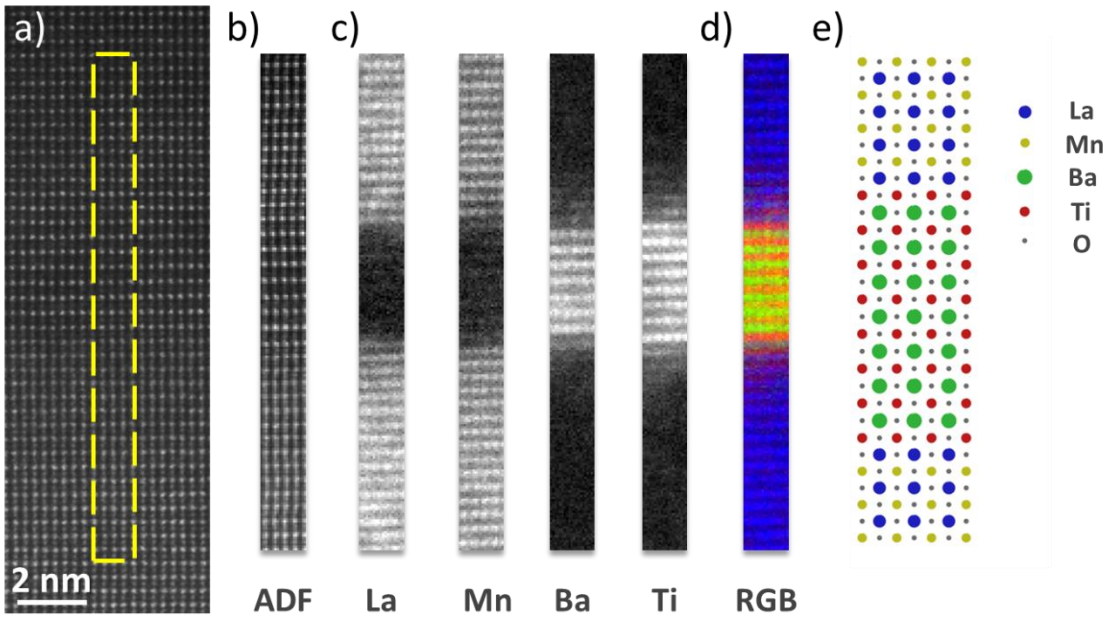

Figure 6.9: a) HAADF image of the LSMO/BTO/LSMO trilayer with the region studied marked with a yellow box. b) ADF image recorded simultaneously to the EEL spectrum image. c) La $M_{4,5}$, Mn $L_{2,3}$, Ba $M_{4,5}$ and Ti $L_{2,3}$ EELS intensity maps. d) RGB color mix with Mn in blue, Ti in red and Ba in green. e) Diagram showing the different elements in the specimen and the symmetric termination of the LSMO/BTO interfaces.

Figure 6.9 shows a high magnification EEL spectrum image of the interfaces in a LSMO/BTO/LSMO trilayer. Figure 6.9(a) shows the HAADF image of the region where the spectrum image was acquired (highlighted with a yellow square). In Figure 6.9(b) we show the simultaneous ADF image recorded with the EEL spectrum image, where we can see that the pixel sampling rate is high enough to obtain an atomic resolution spectrum image. The different chemical maps corresponding to the La $M_{4,5}$, Mn $L_{2,3}$, Ba $M_{4,5}$ and *Ti* $L_{2,3}$ edges are shown on Figure 6.9(c). We observe a TiO_2 termination for both top and bottom interfaces of the $BaTiO_3$ layer. Therefore both LSMO layers are terminated in $La_{0.7}Sr_{0.3}O$ planes. In (d) and (e) we show a color map and an atomic diagram with Ti (red), Ba (green), La (blue) ad Mn (yellow) where the symmetric termination of the BTO and LSMO layers is better perceived. The symmetric configuration produces two opposite

electric dipoles in the interfaces (*222*) which could effectively pin the ferroelectric polarization in the BTO layer, thus affecting strongly the ferroelectric properties (*223*) and possibly creating a ferroelectric dead layer at both interfaces (*224*). We will see later in the chapter how, indeed, the symmetric structure of our system is the key to explain the properties found.

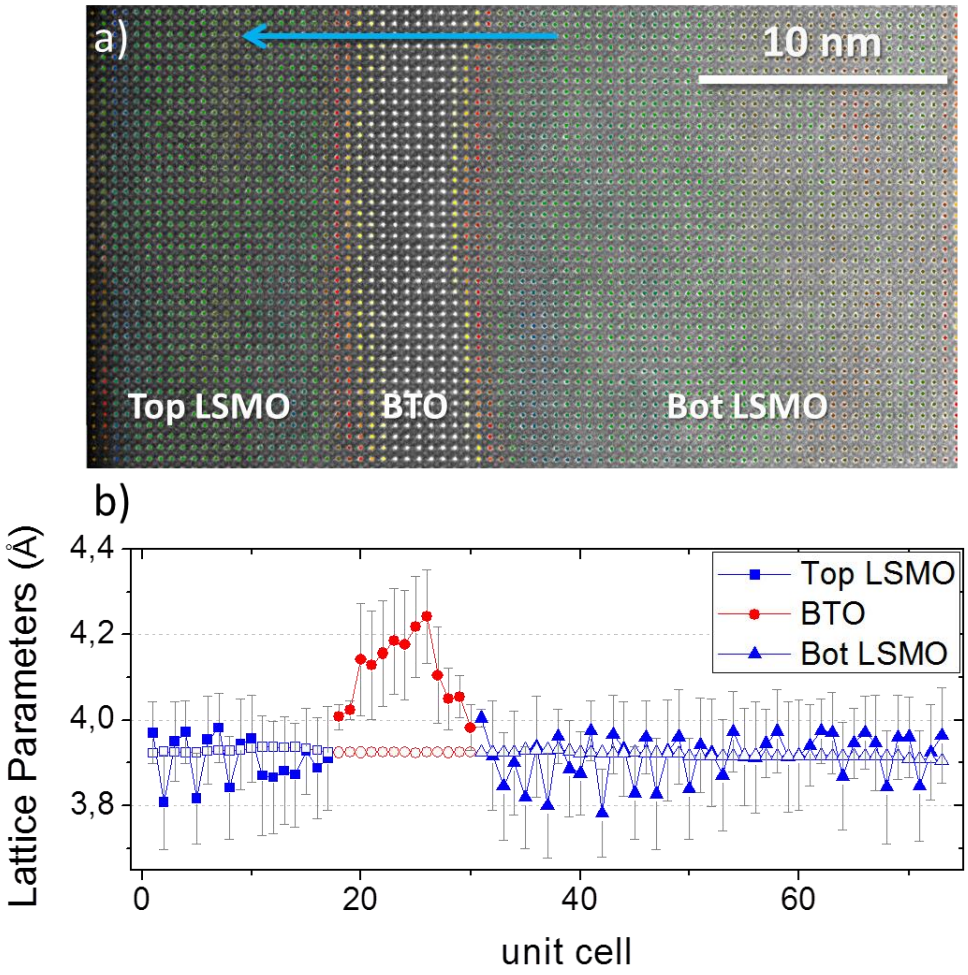

Figure 6.10: Atomic plane-by-plane values of lattice parameters for a LSMO/BTO/LSMO trilayer. a) HAADF image with a false color $\boldsymbol{\varepsilon_{yy}}$ strain map superimposed. The blue arrow indicates the growth direction. b) Out (solid symbols) and in plane (open symbols) lattice parameters profiles obtained measuring the A-site atomic positions directly on the HAADF image in (a).

We have also studied the strain behavior along the different layers of our specimen using the PPA plug-in (*66*) for Digital Micrograph. In Figure 6.10(a) we show the evolution in the out of plane lattice parameter for the three layers. We have superimposed the ε_{yy} strain map created with PPA over the original HAADF image. Thanks to this image, we can identify the position of our BTO layer, determined by the atomic columns

with a higher out-of-plane strain values (brighter spots). On the other hand, we have also measured the A-site atomic column positions directly on a HAADF image (*62–64*), explained in chapter 2. From the atomic column position mapping, we have calculated the distances for consecutive La/Ba columns in the growth direction and averaged these values for each atomic plane (Figure 6.10(b)). From this study we can estimate averaged values for BTO out and in plane lattice parameters, obtaining values of c_{BTO}=4,11 Å and a_{BTO}=3,92 Å, which correspond to a tetragonality ratio c/a of 1,05. This result is in agreement with reported values in similar ferroelectric nanometric BTO thin films (*188, 194*). Figure 6.10(b) shows that the in plane lattice parameter (open symbols) slightly increases through the different layers, which indicates a small strain relaxation along the heterostructure. In the out of plane direction we perceive strong strain gradients in both interfaces. The gradient is stronger at the bottom interface, where a maximum value is found. There is also a slight gradient in the LSMO closer to the bottom interface.

We have also performed a similar analysis studying superlattices with similar thicknesses. Next we show an example of a superlattice of 17 u.c. of $La_{0.7}Sr_{0.3}MnO_3$ and 11 u.c. of $BaTiO_3$ with two repetitions. Having thinner LSMO layers we were able to probe the substrate and the first BTO layer at the same time using magnifications high enough for our atomic resolution analysis.

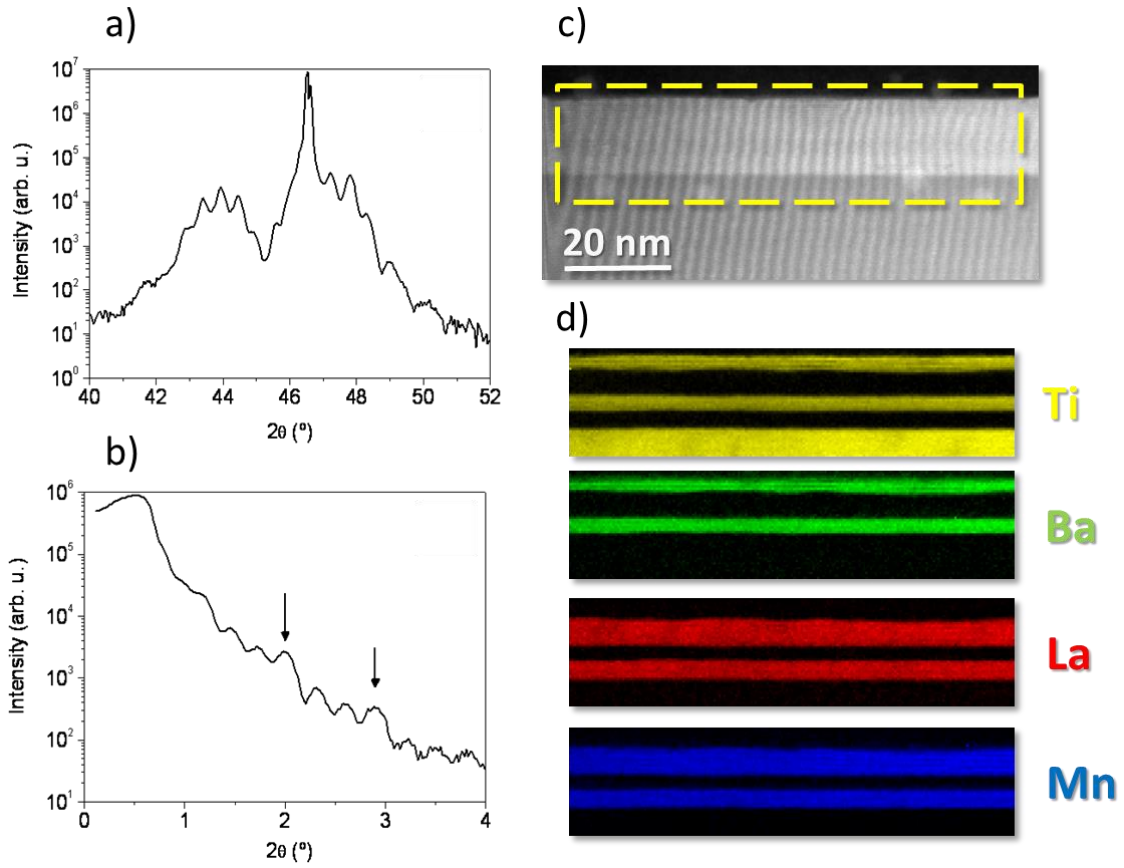

Figure 6.11: a) X-ray diffraction spectra and (b) X-ray reflectivity of a LSMO/BTO superlattice. c) Low magnification HAADF image of the superlattice showing the region where a spectrum image was acquired. d) EELS chemical maps showing the Ti $L_{2,3}$, Ba $M_{4,5}$, La $M_{4,5}$ and Mn $L_{2,3}$ edges integrated intensity.

First, we perform a structural and chemical characterization of the sample. In Figure 6.11 (a) and (b) an X-ray diffraction near the STO (002) Bragg peak and the reflectivity spectra are shown. Superlattice Bragg peaks around the substrate (002) reflection are observed. The arrows in (b) indicate again the superlattice reflections in the reflectivity spectra. These measurements exhibit the coherent growth of the heterostructure. The low magnification HAADF image in (c) shows the region where an EEL spectrum image was acquired (highlighted with a yellow rectangle). In Figure 6.11(d), we show the different chemical species in our specimen, with integrated signal maps below the Ti $L_{2,3}$, Ba $M_{4,5}$, La $M_{4,5}$ and Mn $L_{2,3}$ edges, where all the layers of the heterostructure are resolved. From this analysis, we can appreciate that the layers are flat and continuous over long lateral distances.

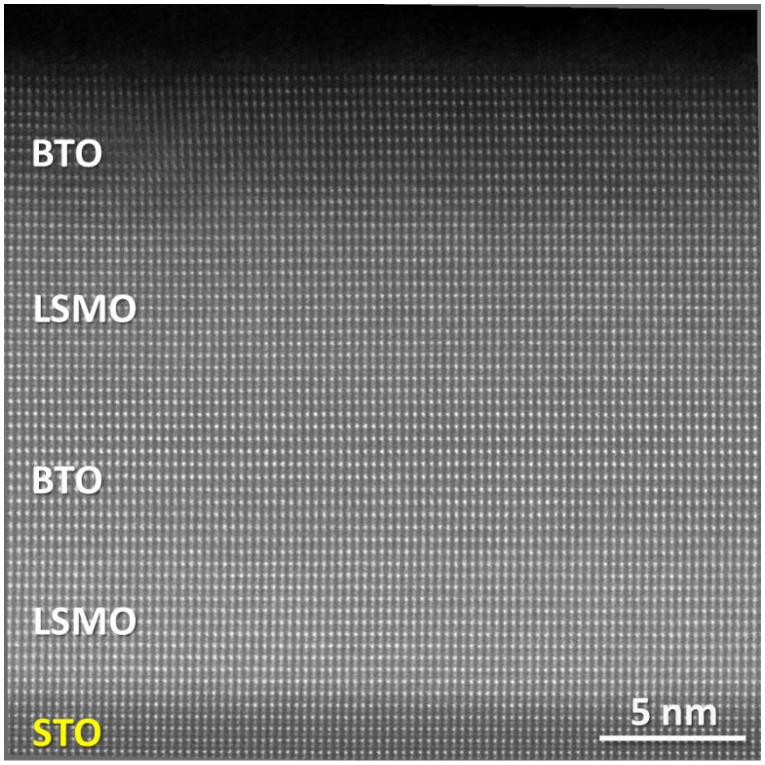

Figure 6.12: High magnification HAADF image of a $La_{0.7}Sr_{0.3}MnO_3$ / $BaTiO_3$ superlattice down the (110) direction showing the high quality epitaxial growth.

Figure 6.12 shows a high magnification HAADF image of the LSMO/BTO superlattice. The growth is perfectly epitaxial and the different layers are fully strained to STO in-plane lattice parameter. Again, such strain imposes a constraint for the ferroelectric polarization in the BTO layer making the unit cell expand in the out-of-plane direction and forcing the ferroelectric polarization to align preferentially along this axis (*221*). In this image, we can appreciate how there is nearly no contrast difference between the LSMO and the BTO layers in the image, making it very hard to identify the interfaces. We will again use EELS and strain mapping to study the layers and determine the interfacial atomic planes.

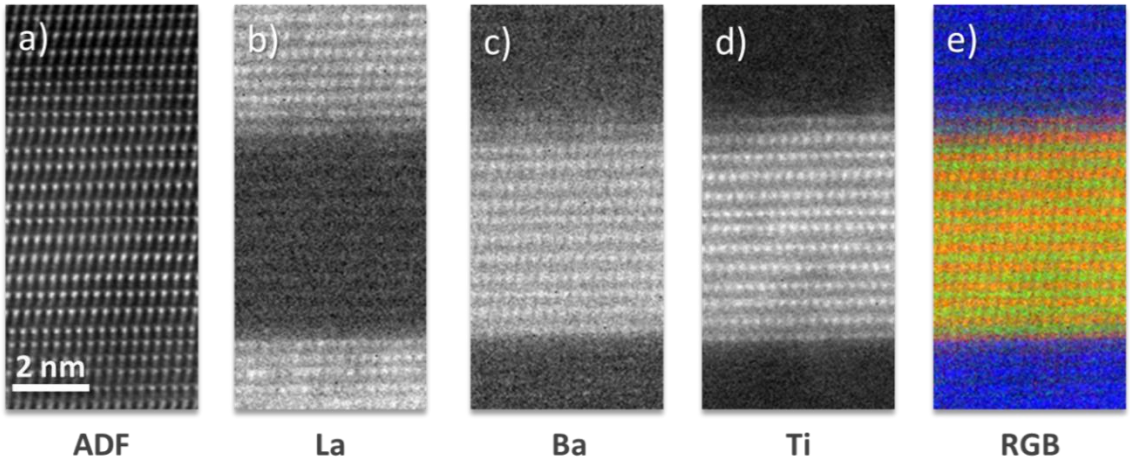

Figure 6.13: High magnification EEL spectrum image of the interfaces in a $La_{0.7}Sr_{0.3}MnO_3$ / $BaTiO_3$ superlattice. a) ADF image recorded simultaneously to the EEL spectrum image. b) La $M_{4,5}$, c) Ba $M_{4,5}$ and d) Ti $L_{2,3}$ EELS intensity maps. d) RGB color mix with La in blue, Ti in red and Ba in green. Some spatial drift is observed.

The BTO layer in the first superlattice bilayer is depicted in the high magnification EEL spectrum image of Figure 6.13. In (a) we show the simultaneous ADF image recorded with the EEL spectrum image, where some drift is observed. In Figure 6.13 (b), (c) and (d) we can see the different chemical maps corresponding to the La $M_{4,5}$, Ba $M_{4,5}$ and Ti $L_{2,3}$ edges, where a TiO_2 termination is observed for both the top and bottom interfaces of the $BaTiO_3$ layer. Again, there is a preferential TiO_2 termination for the BTO layers, and both LSMO layers are terminated in $La_{0.7}Sr_{0.3}O$ planes. These terminations may influence strongly the ferroelectricity in the BTO layer (*222–224*), as explained before.

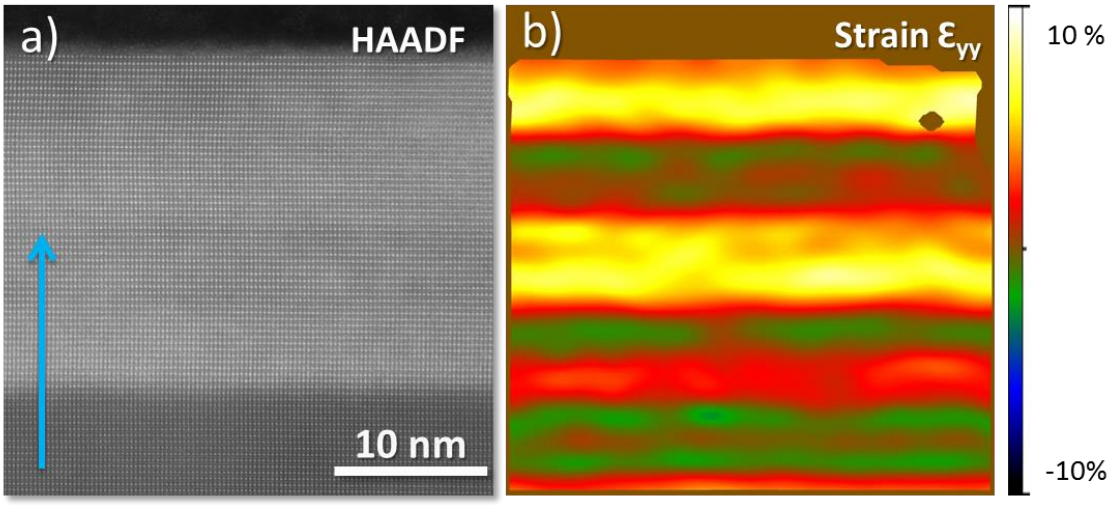

Figure 6.14: HAADF image of a $La_{0.7}Sr_{0.3}MnO_3$ / $BaTiO_3$ superlattices where the contrast between the different layers is hardly visible. The blue arrow indicates the growth direction. b) Out of plane strain map from image (a) obtained using Peak Paris Analysis (*66*, *67*) routines for Digital Micrograph.

Before proceeding to measure the atomic column positions as in the trilayers, we need to identify the exact positions of each layer in our images. This time, we perform a strain analysis of the image, using the PPA plug-in for Digital Micrograph (*66*, *67*). The result of this analysis is shown in Figure 6.14(b). The zero level (green/brown color) is assigned to the STO substrate, which we have used as a reference. The BTO layers appear much brighter in the strain map, denoting a high expansive strain due to the bigger lattice parameter of BTO. From this strain map and the EELS results, we can perfectly identify the position of the interfaces in our image.

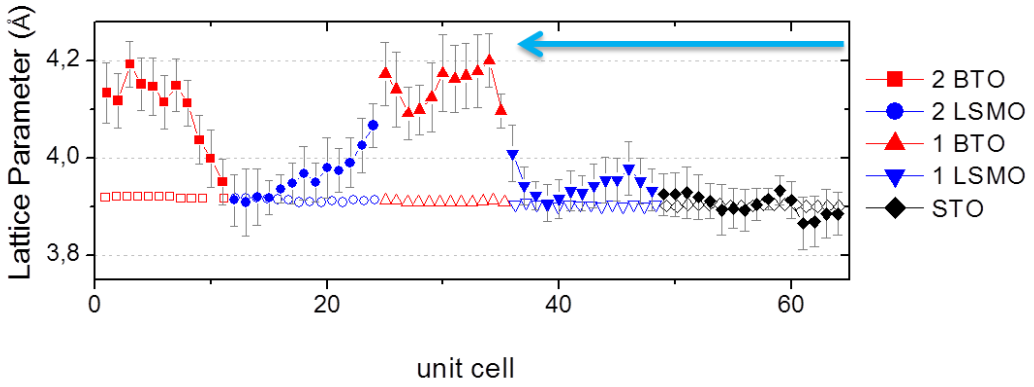

Figure 6.15: Out plane (solid symbols) and in plane (open symbols) lattice parameters profiles obtained measuring the A-site atomic positions directly in the HAADF image in Figure 6.14(a). This profile is rotated 90° with respect to Figure 6.14. The blue arrow indicates the growth direction.

Proceeding with the analysis, we select five different regions: one for each layer and another one for the substrate, in order to measure the atomic column positions for the A cation (Sr, La and Ba). The different layers need to be analyzed independently in order to obtain more accurate values for the atomic positions, since selecting regions containing materials with very different lattice parameters usually results in higher errors. The starting and finishing atomic planes for each layer have been identified using the strain mapping and the EEL spectrum images. Then, we use the procedure explained in chapter 2 to measure precisely the atomic column positions directly on the images (*64*). The values observed for the different layers (averaged over 50 unit cells laterally) are shown in the profiles of Figure 6.15, where the out and in plane lattice parameters are depicted. The values obtained are very similar to the trilayer case. The in plane lattice parameter increases along the growth direction, which is a sign of partial relaxation during the heterostructure growth. The out-of-plane lattice parameters present much stronger gradients than in the trilayer case. We measure a strain gradient at the interface between the first LSMO and BTO layers, with lattice parameters changing from 3,9 Å in the LSMO to nearly 4,2 Å in BTO. A very interesting feature is found in the second LSMO/BTO bilayer. The LSMO presents a clear strain gradient with lattice parameter values ranging from 4,1 Å in the bottom interface to a more relaxed 3,9 Å value at the top end. The second BTO layer exhibits again a highly pronounced strain gradient until the out of plane lattice parameter reaches the 4,1 Å value corresponding to fully strained BTO (*188*, *194*).

Study of the ferroelectric polarization

We can estimate the local polarization within the BTO layer using a model based on the Born effective charges (*225*, *226*). The ferroelectric polarization is defined as the sum of the multiplication of the Born effective charges by the displacements of each ion in the unit cell from their centrosymmetric position (*227*, *228*), as described by the next equation:

$$P(z)=\frac{e}{\Omega}\sum_{m=1}^{N} Z_m^{*}\,\delta u_m \qquad (6.1)$$

where N is de number of atoms in the primitive unit cell, δu_m is the change in the position vector of the mth atom, Z_m^* is the Born effective charge and Ω is the volume of the unit cell. The Born effective charges reported for BTO are 2,83 for Ba, 5,81 for Ti and -1,95 and -4,73 for the O ions in the TiO_2 and BaO planes respectively (*226*). Therefore, knowing the displacements of each atom from the "ideal" cubic structure one can obtain the ferroelectric polarization. In order to observe these structural distortions, we have looked at the crystalline specimen down the (110) pseudo-cubic direction, where oxygen atoms in the TiO_2 plane are far enough from heavier atoms to be easily resolved using the ABF imaging mode.

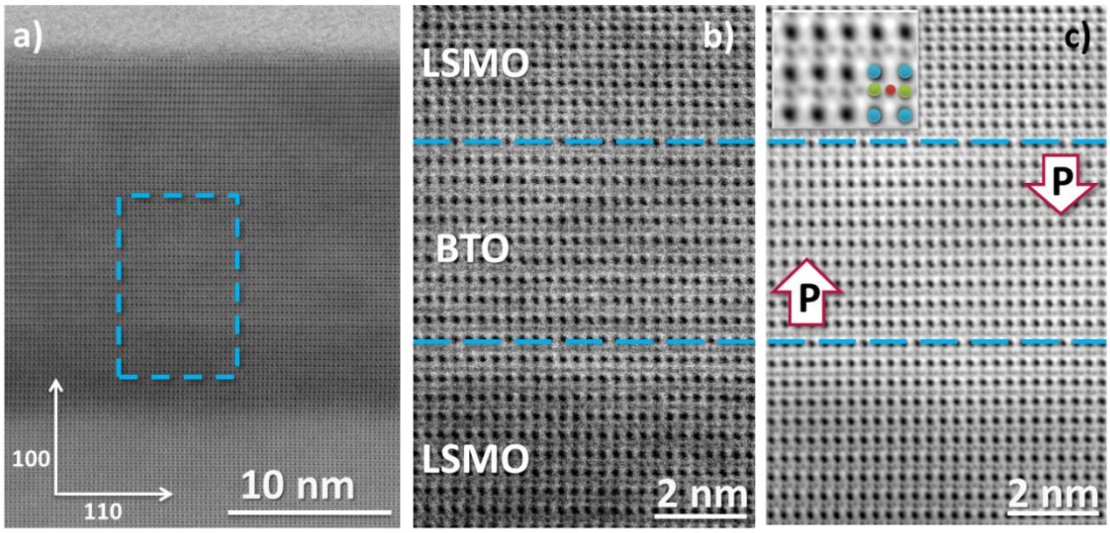

Figure 6.16: a) Raw annular bright field (ABF) image of a $La_{0.7}Sr_{0.3}MnO_3$ / $BaTiO_3$ superlattice. b) Magnified image, from the area highlighted with a blue rectangle in (a). The blue dashed lines denote the interfacial planes. c) Low noise, FFT filtered image obtained from (a) where the oxygen atoms are clearly visible. The inset shows a schematic of the BTO unit cell with Ba (blue), Ti (green) and O (red) atoms.

The ABF image in Figure 6.16(a) shows the four layers grown on top of a $SrTiO_3$ substrate. Figure 6.16(b) exhibits a magnified view of the area highlighted in (a). The interfaces between the LSMO and BTO layers are marked by blue dashed lines. Although oxygen atoms are visible in this image, in order to better appreciate the position for all atomic columns we need to reduce the noise level using a Fourier filter mask (*65*). We find that the oxygen columns in the first planes of the BTO layer are displaced downwards relative to the Ti columns (i.e., towards the bottom LSMO/BTO interface). On the other hand, within the last atomic planes near the top, the oxygen columns are displaced upwards with respect to the Ti columns. Arrows mark the local polarization

direction resulting from this structural configuration. These observations suggest that somewhere through the layer there is an inversion of the polarization direction and, hence, a ferroelectric domain wall.

In order to make a semi-quantitative estimate of the local polarization, we can use the low noise filtered images to measure the atomic column coordinates of all species (*64*) and calculate their displacements. However, since we are studying a projection of the sample down the (110) direction, we are not able to measure the oxygen columns in the Ba-O plane. Thus, we will have to make an approximation estimating the local polarization in terms of the relative displacement along the out-of-plane axis between the Ti and the planar O columns. Once we have the coordinates of all visible atomic columns, we can proceed to quantify the relative Ti-O displacement (δz), which is proportional to the local ferroelectric polarization (*224*), using the Ba sublattice as a reference, as shown in Figure 6.17.

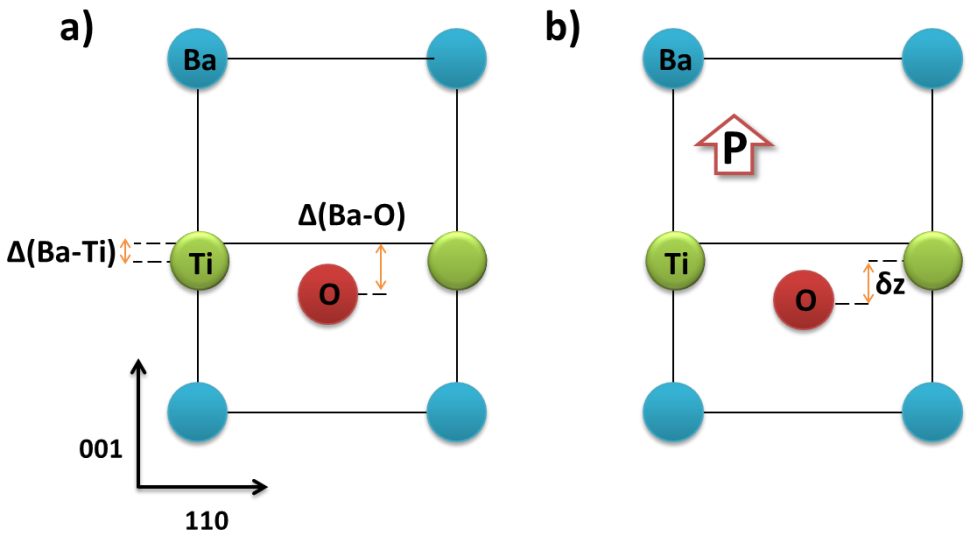

Figure 6.17: Schematic of BTO down the (110) orientation demonstrating the relative displacement measurement. a) Schematic showing the displacements of Ti and O from the center of the unit cell. b) Schematic showing the relative Ti-O displacement (δz), which is proportional to the ferroelectric polarization.

Figure 6.18 displays the calculated relative Ti-O displacement (δz) false color maps for both the first and second BTO layers in the heterostructure. Each pixel in the maps shows the value of δz for each unit cell. Mapping the values of δz like this, we can track

the local polarization in a semi-quantitative fashion unit cell by unit cell. The displacement maps show an inhomogeneous polarization along the ferroelectric layer, with positive values near the bottom interface and negative values close to the top. The profiles on the right show the lateral average. The absolute values of δz are of the order of 0.1 – 0.2 Å, consistent with previous studies (*62*, *229*, *230*). Our measurement indicates that there is a head-to-head domain wall inside the ultrathin (11 u.c.) ferroelectric layer, with a polarization profile which ranges from positive values in the bottom interface, to negative values at the top. While the shape of the domain wall is not flat, it is worth noting that, on average, its position lies in the middle of the BTO layer. This is the case for both ferroelectric layers. Although the qualitative results in both first and second layers are similar, the absolute values for δz are larger in the second BTO. Oxygen vacancies or surface reconstructions may be responsible for these high values. Also, we must note that these values actually are the projection of the polarization vector along the *c* axis, averaged along the thickness of the whole specimen. Therefore, we cannot distinguish if the displacement vector has some component parallel to the electron beam direction.

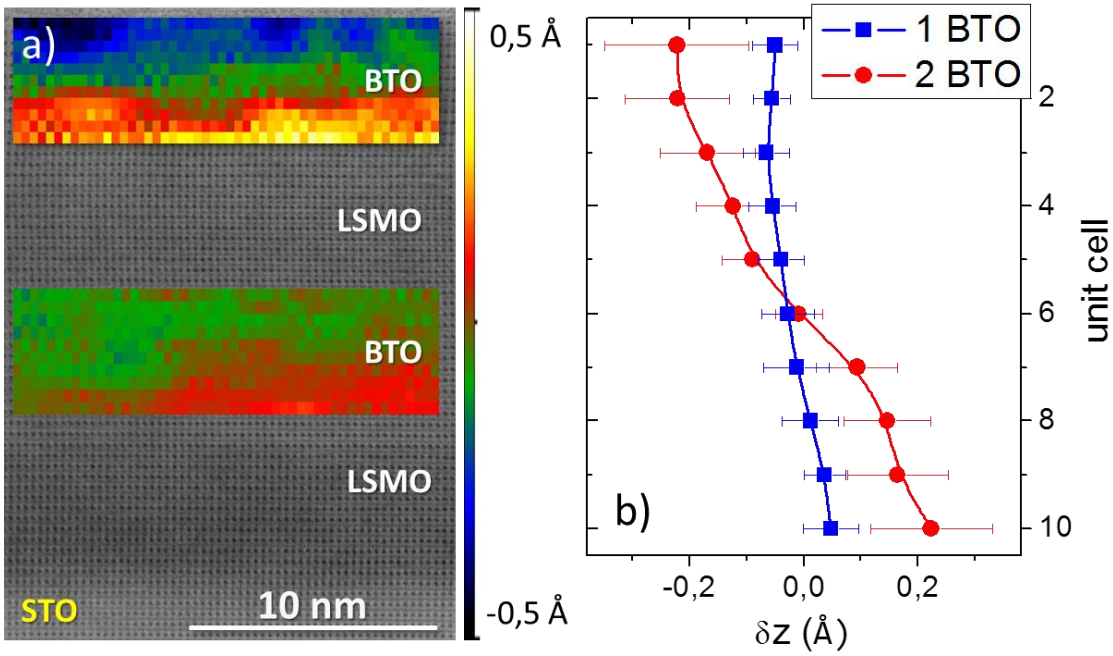

Figure 6.18: a) ABF image of the LSMO/BTO superlattice with the Ti-O δz maps for the first and second BTO layers superimposed to the image. Each pixel of the maps corresponds to one unit cell. b) Averaged horizontal profiles obtained from the maps shown in (a). The error bars correspond to the statistical deviation after averaging laterally 50 unit cells.

From now on, our attention will be focused on the study of the first BTO layer, which is more representative of the trilayer case and therefore of the measured tunnel junctions. Figure 6.19 displays a more detailed δz map superimposed over the image in Figure 6.16(c). The positive (bottom) ferroelectric domain exhibits a triangular shape, which has been predicted theoretically and observed previously for ferroelectric domains (*198*, *229*, *231*). This irregular shape results in the laterally averaged profiles in Figure 6.18(b) exhibiting a sign change that seems to extend over several unit cells. However, the local width of the domain wall is much narrower. If we pay close attention to the displacement maps, there are regions where it takes place within a unit cell. This observation suggests that the domain wall may be sharp within very short lateral length scales. Indeed, if we analyze the displacements in small regions tracing profiles perpendicular to the domain wall, the sign change occurs in a very abrupt fashion. An example of this is presented in Figure 6.19(b), which displays how the δz gradient is more pronounced within 1-2 unit cells around the zero-value plane. The slope of δz gradually decreases near both interfaces reaching a plateau, suggesting that the polarization saturates. This behavior has been predicted theoretically before (*224*) but to the best of our knowledge this is one of the first experimental observations. Regarding the saturation values, we can give an estimate of the polarization in our system by using equation 6.1 and an averaged charge for the oxygen atoms in both Ba-O and Ti-O_2 planes, defined as $\overline{Z_m^*} = -\frac{4{,}73+2\cdot 1{,}95}{3} = -4{,}3$. For a saturation displacement of $\delta z = 0.12$ Å, a value of the polarization at the interfaces of $P = 0.27\ C/m^2$ is obtained. This result is very close to the bulk polarization in BTO ($0.26\ C/m^2$).

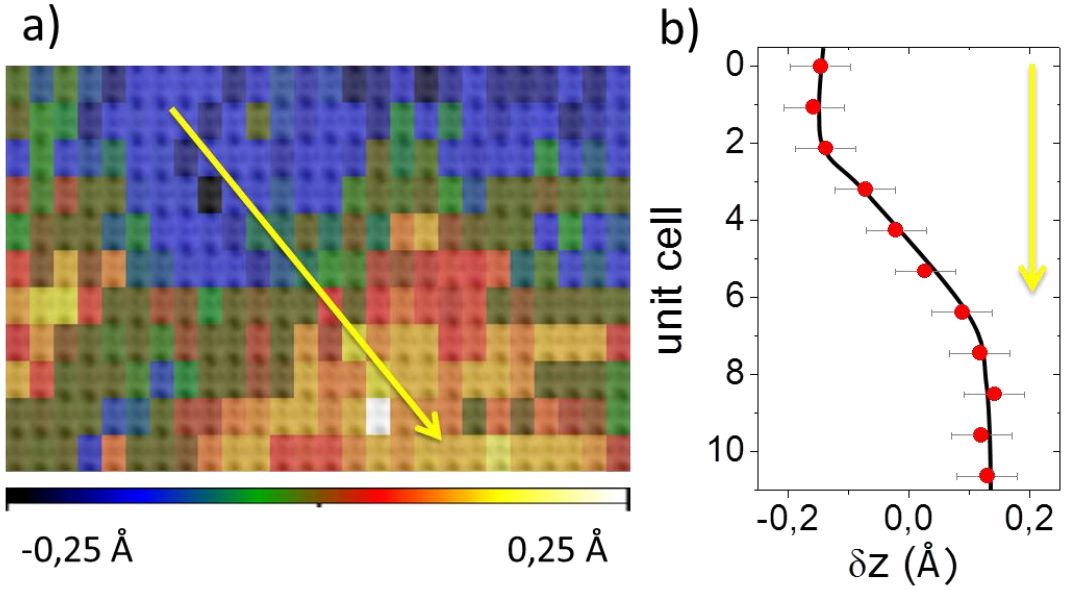

Figure 6.19: a) Ti-O δz map from the BTO layer in Figure 6.16(c), each pixel corresponding to one unit cell. b) Averaged profile of the δz displacements in the direction perpendicular to the domain wall, showing the unit cells above and below the geometric head-to-head domain wall plane. The black line is a guide for the eye. The yellow arrows indicate the direction of the profile.

The finding of a head-to-head ferroelectric domain wall in this system would imply a significant accumulation of ferroelectric bound charge at the wall, which must be screened by free negative charges (*231–235*). In undoped semiconductor ferroelectrics, the screening charge results from electron transfer across the forbidden energy gap, E_g, of the ferroelectric, which requires strong band bending until the bottom of the conduction band falls below the Fermi level. The creation of a charged domain wall thus involves an energy of $2\,P_0 Eg/e$, where P_0 is the equilibrium polarization at both sides of the domain wall. For BTO, with a $P_0 = 0.26\,C/m^2$ and an energy gap of 3.2 eV, charged domain walls have a large energy cost of $1600\,erg/cm^2$, which compares with the $2.5\,erg/cm^2$ of the neutral domain walls. The thickness of a charged domain wall is essentially determined by the availability of free carriers to screen its bound charge. Thus screening sets a width of the barrier, which can be estimated to be of the order of the Thomas Fermi screening length, the length scale for charged inhomogeneities. For intrinsic BTO with an effective density of states at the conduction band of 10^{18} cm^{-3}, the width of a charged domain wall can be estimated to be in the range 10 – 20 nm. It is thus particularly puzzling that a nanometer thick, energetically expensive head-to-head charged domain wall is found in the BTO tunnel barrier with a polarization vector directed in the (001)

crystalline orientation (which typically yields neutral domain walls). The very narrow width of the domain wall implies that free charges must be available to screen the polarization charges.

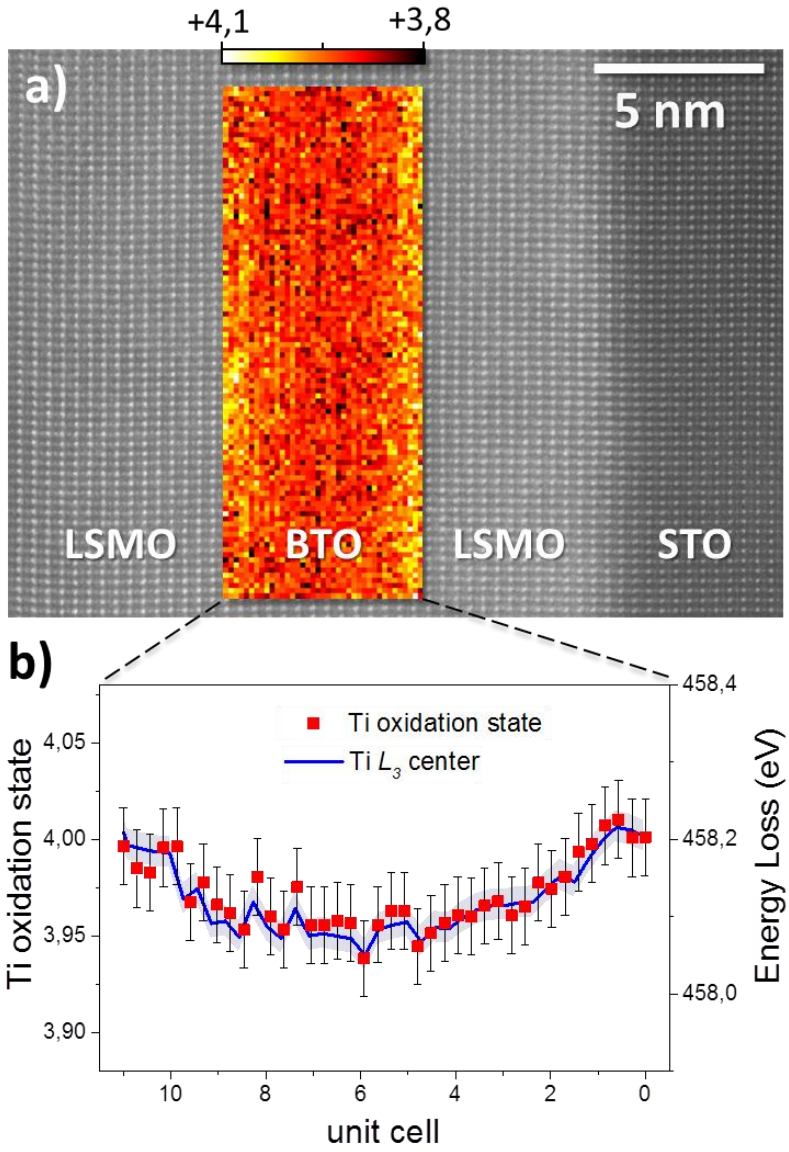

Figure 6.20: a) Z-contrast image of the LSMO/BTO superlattice. The inset shows the titanium oxidation state map from the BTO layer. b) Titanium oxidation state across the BTO layer, averaged laterally (red squares). The blue curve represents the position of the Ti L_3 edge. The origin in the x axis corresponds to the bottom BTO/LSMO interface.

Thus, in order to understand how this head-to-head domain wall configuration is stable in our system, we need to analyze the electronic properties of the ferroelectric BTO layer. This study can be addressed through the analysis of the occupation of the Ti *3d* band, which affects features such as the crystal field splitting in the L_2 and L_3 edges fine

structure (*117*). After measuring the Ti $L_{2,3}$ ELNES throughout our BTO layers, we have obtained the Ti oxidation state using the MLLS fit method (*29*, *118*) explained in chapter 2. For this aim, we have used two reference spectra for bulk $LaTiO_3$ (Ti^{+3}) and $BaTiO_3$ (Ti^{+4}) to decompose our experimental spectrum in one component for each oxidation state. This way, we obtain the Ti oxidation state for each pixel in a spectrum image, thus producing a 2D map of the Ti oxidation state across the BTO layer (*110*). Figure 6.20(a) shows an HAADF image of the superlattice, where the Ti oxidation state map obtained this way is superimposed on top of the ferroelectric layer. A reduction in the oxidation state takes place well into the BTO layer. In order to appreciate this behavior with more detail, we have averaged laterally the values for each pixel in the map, and the resulting profile is shown in Figure 6.20(b). In both interfaces the value is around the nominal +4 value, while inside the layer, a reduction to ≈ +3.95 is observed. We also find a small chemical shift of the Ti $L_{2,3}$ edge, shown in the blue curve in Figure 6.20(b), which also indicates a reduction of Ti (*116*). This observation results from a 5% of titanium atoms with a +3 oxidation state, which is equivalent to a maximum concentration of charge carriers of $n = 8 \cdot 10^{20} cm^{-3}$.

Discussion

We have used aberration corrected STEM-EELS to study the ferroelectric polarization and the electronic properties in multiferroic complex oxide heterostructures. Using the ABF imaging mode, which is sensitive to light atoms as oxygen, we have measured the atomic column positions for all species in our ferroelectric layer, and we have quantified the relative displacement between Ti and O, which is related to the ferroelectric polarization. We have also studied the fine structure of the Ti $L_{2,3}$ edge, quantifying the oxidation state, and as a result, the occupation of the Ti *3d* bands. Our findings suggest that there is a charged head-to-head domain wall inside the ferroelectric barrier. The presence of such head-to-head domain wall is connected to pinning of the ferroelectric polarization by interface dipoles. These dipoles would result from differences of the bonding strength at both sides of the interface along with atomic or electronic reconstructions due to the symmetrical LaO termination of both manganite layers. Both symmetrical interface terminations together with the donor character of the LaO plane

help stabilizing a head-to-head domain wall. Our data proof that a confined electron gas is formed within the 4.4 nm thick BTO layer.

We believe that these carriers are supplied by oxygen vacancies at the interfaces of the ferroelectric layer with the ferromagnetic LSMO layers. These vacancies may help to accommodate the large epitaxial mismatch between these materials and the strong strain gradients occurring at the BTO interfaces as shown in Figure 6.15. The presence of oxygen vacancies enhances the repulsion between B site cations, producing the observed expansion of the lattice around them (*99, 236*). Thus, the nucleation of oxygen vacancies is a mechanism that helps releasing the elastic energy stored in uniformly strained structures and accommodating this large lattice mismatch (*237*). Large concentrations of O vacancies in complex oxide thin films are not unusual and have been observed in regions under compressively strain around dislocation cores in grain boundaries in STO (*156*) and YBCO (*159*). As shown in Figure 6.21(a), the positively charged vacancies help compensate the negative polarization charges at the interfaces, contributing to stabilize the head to head domain wall. Furthermore, if we assume that each vacancy may supply one electron and that these free electrons are uniformly distributed across the BTO layer, screening the charged domain wall as the EELS measurements suggest, we can estimate an upper limit for the thickness of the domain wall of 2 nm. This result is in good agreement with the structural results in Figure 6.19. Notice also that for such electron doping, the Thomas Fermi screening length is in the range of 1 nm (*218*) which again provides the correct length scale for the width of the domain wall. It is important also to notice that although these levels of doping may appear high, BTO is known to retain its ferroelectric ground-state with charge densities in excess of $2 \cdot 10^{21} cm^{-3}$ (*216, 218*), as explained before. Assuming that the charge transferred from the ionized vacancies is about 0.05 electrons per unit cell, the carrier density for the electron gas is $n_{2D} = 3 \cdot 10^{14} cm^{-2}$, which is similar to those reported at the surface of STO single crystals and also at the LAO/STO interface (*238*). These findings lead us to think that charge in the form of free electrons accumulates in the region of the head-to-head domain wall inside the ferroelectric layer, screening the polarization discontinuity and producing a two-dimensional high mobility conduction channel (*235*).

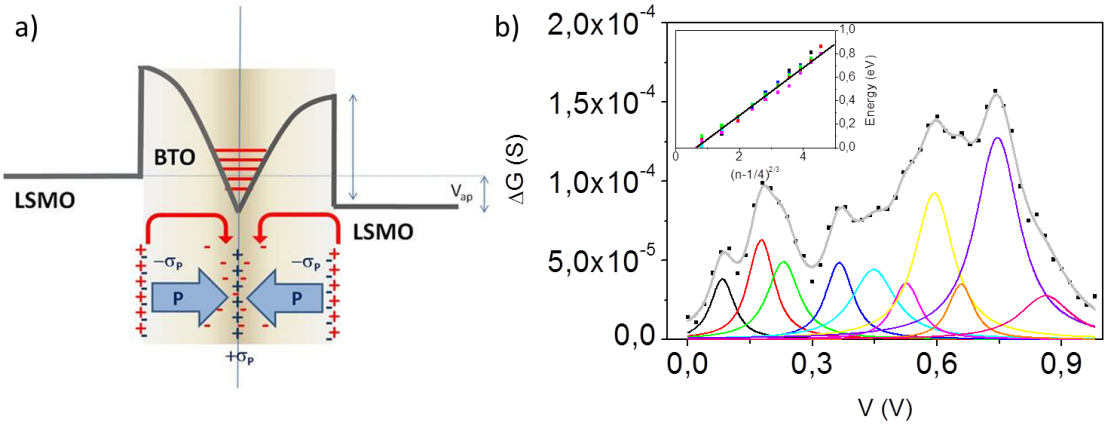

Figure 6.21: a) Energy levels and band bending schematic. b) Oscillations maxima from Figure 6.6, identified by subtracting a triangular envelop from the experimental differential conductance curves. The inset shows a fit to the values expected for a triangular well.

We believe that the 2DEG is the origin of the oscillations found in the magneto transport measurements. The charged accumulation in the domain wall can give rise to a band bending at the BTO which can be approximated by a potential well (see sketch in Figure 6.21(a)). Figure 6.21(b) shows the voltage values of the conductance maxima obtained subtracting a triangular envelope to the experimental curves from Figure 6.6. The data fit very well into to the theoretical expression corresponding to a triangular well potential as shown in the inset. The nature of the potential well is not completely understood yet and the approximation can also be done to a parabolic potential with similar results.

In summary, we have shown that the electronic confinement of the ferroelectric quantum well of the head-to-head domain wall is the mechanism responsible for the tunneling transport in our magnetic tunnel junctions. This finding traces a new avenue for future device concepts in oxide electronics exploiting the electronic structure of ferroelectric domain walls (*196*). As it has been proposed, the domain walls may constitute the active part of the device (*195*).

Chapter 7: Summary

The quest for novel functionalities in material science has often been determined by reducing dimensionality and designing nanostructured systems that exploit new physical effects. The physical phenomena occurring at these scales are ruled by the properties of small active regions, such as interfaces, point or extended defects, etc. In order to understand any underlying physics, new tools capable of analyzing these systems with atomic resolution and in real space are essential. The evolution of STEM-EELS since the development of the aberration corrector, has transformed these techniques in most powerful tools for material science research. In this work, we address a series of technologically relevant physical problems within the fields of energy, electronics and spintronics where state-of-the-art aberration corrected electron microscopy helps harnessing the macroscopic behaviour. Analyzing slight fluctuations of the atomic structure, composition and electronic environment within nanometric regions such as surfaces, grain boundaries or interfaces, we have been able to explain a number of physical effects establishing the link between the atomic and macroscopic worlds.

Experimental Results

- First, we have analyzed the formation of new superficial phases by controlled irradiation processes on titanium oxides, explaining how changes in the atomic structure and composition affect the macroscopic physical properties. Irradiation can result in the formation of high ordered TiO crystalline layers in the surface of TiO_2 (*109*). On a different front, the irradiation of $SrTiO_3$ single crystals leads to the formation of oxygen vacancies. In this case, the procedure induces an insulator-to-metal transition, doping the superficial titanium atoms and inducing surface metallic states (*87*, *110*).

- We have also combined transport measurements, the analysis of structural strain and chemical composition with atomic resolution and DFT calculations

in order to shed some light to the problem of conductivity blocking in grain boundaries of ionic conductors. Impedance spectroscopy measurements show how the width of the space charge layer at both sides of the grain boundary is $\lambda^* \approx 4 \pm 1$ Å, much thinner than previous estimates (*141*). We found a strong Y segregation to the expansive site of the dislocation cores within the grain boundary, along with a reduction in the oxygen content. These chemical fluctuations produce a lack of stoichiometry within a range of 5 Å (one unit cell), as obtained from the FWHM of the EELS oxygen and yttrium compositional profiles. The length scales found with the microscopy study are in good agreement with the results from the dielectric spectroscopy measurements. Using DFT calculations we have been able to show how the presence of oxygen vacancies is intrinsic to the grain boundary, lowering by more than 0.1 eV/Å^2 its formation energy. Electrons arising from the oxygen vacancies are captured in empty electronic states in the energy gap of the grain boundary, giving rise to an electrostatic potential that acts as a barrier for the ionic conductivity.

- The high spatial resolution of aberration corrected electron microscopy allows the study of structural distortions using atomic resolution EEL spectrum images and new detectors capable of imaging light atoms. In particular, we have analyzed collective perturbations in the oxygen sub-lattice of complex oxide heterostructures and the relationship with new physical phenomena non present in the bulk. The analysis of superlattices composed of the Mott insulator $LaMnO_3$ and the band insulator $SrTiO_3$ have shown a correlation between the rotations of the BO_6 oxygen octahedra and induced epitaxial strain controlled by the thickness of the titanate. Our findings suggest that these distortions are related to the presence of an interfacial metallic and ferromagnetic phase (*29*, *182*). Next, we combine such manganite layers with ferroelectrics materials ($BaTiO_3$) producing multiferroic tunnel junction. We have measured the relative Ti and O in-plane displacements (δz) in the ferroelectric layer, which are proportional to the polarization (*224*). Using this method, we are able to track the ferroelectric displacements unit cell by unit cell, obtaining the ferroelectric domain configuration. Our measurements show

an inversion of the polarization direction across ultra-thin ferroelectric layers, suggesting the presence of a head-to-head domain wall. This behavior has been predicted theoretically before (*224*) but to the best of our knowledge this is one of the first experimental observations. The layers exhibit strong polarization gradients that reach a plateau close to the interfaces, with a polarization value very close to the bulk material. EELS measurements have shown the accumulation of electrons screening the polarization bound charge at the domain wall and stabilizing this highly unstable charged head-to-head configuration. Moreover, our calculations show how a confined 2D electron gas with accessible electronic states is formed in the vicinity of the domain wall. Combining these studies with an analysis of transport measurements, we have explained how electronic states in the domain wall provide a mechanism for quantum resonant tunneling across our multiferroic heterostructure.

Conclusion

Throughout this thesis, we have shown how the atomic resolution analytical capabilities of the aberration corrected electron microscope provide a very powerful tool to explore minor structural distortions and slight compositional fluctuations in materials that can give rise to a very rich variety of physical phenomena. Minor densities of defects, inhomogeneous strain fields or domain walls can be now analyzed with an unprecedented level of detail, bridging the connection between atomistic mechanisms and electronic properties. The continuous development of such experimental techniques and theory beyond current limitations of spatial and energy resolution holds the promise of a very bright future for materials research in the electron microscope. Now, more than ever, the quest for frontiers yet to be revealed in the nanoscopic world is within reach.

Annex

List of publications

1) F. Y. Bruno, J. Tornos, M. Gutierrez del Olmo, **G. Sanchez Santolino**, N. M. Nemes, M. Garcia-Hernandez, B. Mendez, J. Piqueras, G. Antorrena, L. Morellón, J. M. De Teresa, M. Clement, E. Iborra, C. Leon and J. Santamaria, "*Anisotropic magnetotransport in $SrTiO_3$ surface electron gases generated by Ar+ irradiation"*, Phys. Rev. B **83**, 245120 (2011).

2) A. Rivera-Calzada , M. R. Diaz-Guillen , O. J. Dura , **G. Sanchez-Santolino** , T. J. Pennycook , R. Schmidt , F. Y. Bruno , J. Garcia- Barriocanal , Z. Sefrioui , N. M. Nemes , M. Garcia-Hernandez , M. Varela , C. Leon , S. T. Pantelides , S. J. Pennycook and J. Santamaria, "*Tailoring Interface Structure in Highly Strained YSZ/STO Heterostructures"*, Advanced Materials **23**, 5268-5274 (2011).

3) F. A. Cuellar, **G. Sanchez-Santolino**, M. Varela, M. Clement, E. Iborra, Z. Sefrioui, J. Santamaria, and C. Leon, "*Thermally assisted tunneling transport in $La_{0.7}Ca_{0.3}MnO_3/SrTiO_3$: Nb Schottky-like heterojunctions"*, Phys. Rev. B **85**, 245122 (2012).

4) **G. Sánchez-Santolino**, J. Tornos, F.Y. Bruno, F.A. Cuellas, C. León, J. Santamaría, S.J. Pennycook, M. Varela, "*Characterization of surface metallic states in $SrTiO_3$ by means of aberration corrected electron microscopy"*, Ultramicroscopy **127,** 109-113 (2013).

5) **G. Sánchez-Santolino**, M. Cabero, M. Varela, J. Garcia-Barriocanal, C. León, S.J. Pennycook and J. Santamaria , "*Oxygen Octahedral Distortions in $LaMnO_3$ / $SrTiO_3$ Superlattices"*, Microscopy and Microanalysis **20**, 03, 825-831 (2014).

6) F. Cuellar, Y. Liu, J. Salafranca, N. Nemes, E. Iborra, **G. Sánchez-Santolino**, M. Varela, M. Garcia-Hernandez, J. Freeland, M. Zhernenkov, M. R. Fitzsimmons, S. Okamoto, S. J. Pennycook, M. Bibes, A. Barthelemy, S. G. R. te Velthuis, Z. Sefrioui and C. Leon , "*Reversible electric-field control of magnetization at oxide interfaces"*, Nat. Commun. 5:4215 doi:10.1038/ncomms5215 (2014).

7) B. M. Pabon, J. I. Beltran, **G. Sánchez-Santolino**, I. Palacio, J. Lopoez-Sanchez, J. Rubio-Zuazo, J. M. Rojo, P. Ferrer, A. Mascaraque, M. C. Muñoz, M. Varela, G. R. Castro and O. Rodriguez de la Fuente , *"Formation of a titanium monoxide (001) single crystalline thin film induced by ion bombardment of titanium dioxide (110)"*, Nat. Commun. 6:6147 doi:10.1038/ncomms7147 (2015).

8) M. A. Frechero, M. Rocci, **G. Sánchez-Santolino**, A. Kumar, J. Salafranca, R. Schmidt, M. R. Diaz-Guillen, O. J. Dura, A. Rivera-Calzada, R. Mishra, S. Jesse, M. Varela, S. T. Pantelides, S. V. Kalinin, S. J. Pennycook, J. Santamaria and C. Leon, "*Paving the way to nanoionics: atomic origin of barriers for ionic transport through interfaces"*, Scientific Reports, *submitted* (2015).

9) M. N. Grisolia, **G. Sánchez-Santolino**, M. Varela, S. Valencia, R. Abrudan, E. Schierle, A. Barthelemy, J. Santamaria and M. Bibes, "*Hybridization-controlled charge transfer and induced magnetism at correlated oxide interfaces*", Nature Physics, *submitted* (2015).

10) **G. Sánchez-Santolino**, J. Tornos, D. Hernandez, J. I. Beltran, Z. Sefrioui, C. Leon, S. J. Pennycook, M. C. Muñoz, M. Varela and J. Santamaria "*Resonant tunneling across ferroelectric quantum wells in charged domain walls"*, Nature Materials, *in preparation* (2015).

Conference contributions

1)	*Magnetoelectric effects in oxide magnetic tunnel junctions with ferroelectric barriers*, **Javier Tornos**, YH Liu, SGE Te Velthuis, MR Fitzsimmons, A Rivera, R Lopez Anton, G Sanchez Santolino, M Varela del Arco, NM Nemes, SJ Pennycook, Z Sefrioui, C Leon Yebra, J Santamaria
Contribution	Oral
Location	American Physical Society March Meeting 2013, Baltimore, MA (USA)
Date	March 18-22, 2013
2)	*Study of local polarization in complex oxide Multiferroic interfaces by aberration corrected STEM_EELS*, **G. Sánchez Santolino** , J. Tornos , J. Santamaria, S. J. Pennycook and M. Varela
Contribution	Oral
Location	Enhanced data generated with electrons, EDGE 2013, Sainte-Maxime (France)
Date	May 26-31, 2013
3)	*Studies of local polarization in complex oxide Multiferroic interfaces by aberration corrected STEM-EELS*, **G. Sánchez Santolino** , J. Tornos , C. Leon, M. Varela, S. J. Pennycook and J. Santamaria
Contribution	Oral
Location	American Physical Society March Meeting 2014, Denver, CO (USA)
Date	March 3-7, 2014
4)	*Electric control of tunnel magnetoresistance in oxide multiferroic tunnel junction*, **J Tornos**, Liu Yaohua, G Sanchez-Santolino, C Munuera, SGE te Velthuis, F Mompean, M Garcia-Hernandez, M Varela, SJ Pennycook, Z Sefrioui, C Leon, J Santamaria
Contribution	Oral
Location	American Physical Society March Meeting 2014, Denver, CO (USA)
Date	March 3-7, 2014
5)	*Study of Oxygen Distortions in Titanate – Manganite Interfaces by Aberration Corrected STEM-EELS*, **G. Sánchez Santolino**, J. Tornos, M. Cabero, M. Varela, J. Garcia-Barriocanal, C. Leon, S. J. Pennycook and J. Santamaria

Contribution	Oral
Location	Microscopy & Microanalysis 2014 Meeting, Hartford, CT (USA)
Date	August 3-7, 2014
6)	*Atomic resolution studies of grain boundaries in ionic conducting materials by aberration-corrected STEM-EELS and DFT calculations*, **G. Sánchez Santolino** , J. Salafranca, M. A. Frechero, M. Rocci, R. Schmidt, A. Rivera-Calzada, R. Mishra, S. T. Pantelides, M. Varela, S. J. Pennycook, J. Santamaria and C. Leon
Contribution	Oral
Location	International Microscopy Conference 2014, Prague (Czech Republic)
Date	September 7-12, 2014
7)	*Studies of the relationship between magnetism and ferroelectricity in oxide multiferroic interfaces by aberration corrected scanning transmission microscopy*, **G. Sánchez Santolino**, J. Tornos, D. Hernandez, Z. Sefrioui, C. Leon, J.S. Pennycook, M. Varela and J. Santamaria
Contribution	Oral
Location	Annual conference on magnetism and magnetic materials, 2014, Honolulu, HI (USA)
Date	November 3-7, 2014

Short research stays

Center	Oak Ridge National Laboratory
Location	Oak Ridge, TN, 37830, USA
Date	November 13th – December 18th 2010
Funding	European Research Council
Topic	Characterization of manganite/cuprate tunnel junctions by advanced electron microscopy techniques.
Center	Oak Ridge National Laboratory
Location	Oak Ridge, TN, 37830, USA
Date	February 8th – March 19th 2011
Funding	European Research Council
Topic	Study of YSZ/STO heterostructures by aberration corrected STEM-EELS
Center	Oak Ridge National Laboratory
Location	Oak Ridge, TN, 37830, USA
Date	April 24th – May 16th 2011
Funding	European Research Council
Topic	Characterization of Ar^{+} irradiated STO by advanced electron microscopy techniques.
Center	Oak Ridge National Laboratory
Location	Oak Ridge, TN, 37830, USA
Date	July 14th – August 13th 2011
Funding	European Research Council
Topic	Study of artificial multiferroic tunnel junctions by advanced electron microscopy techniques.
Center	Oak Ridge National Laboratory
Location	Oak Ridge, TN, 37830, USA
Date	October 25th – December 16th 2011
Funding	European Research Council
Topic	Characterization of YSZ grain boundaries by aberration corrected STEM-EELS
Center	Oak Ridge National Laboratory

Location	Oak Ridge, TN, 37830, USA
Date	June 21th – July 5th 2012
Funding	European Research Council
Topic	Characterization of artificial multiferroic tunnel junctions by advanced electron microscopy techniques.
Center	Oak Ridge National Laboratory
Location	Oak Ridge, TN, 37830, USA
Date	November 29th – December 23th 2012
Funding	European Research Council
Topic	Investigation of artificial multiferroic tunnel junctions by aberration corrected STEM-EELS.
Center	Oak Ridge National Laboratory
Location	Oak Ridge, TN, 37830, USA
Date	June 30th – July 31th 2013
Funding	European Research Council
Topic	Characterization of complex oxide interfaces by aberration corrected STEM-EELS.
Center	Oak Ridge National Laboratory
Location	Oak Ridge, TN, 37830, USA
Date	July 16th – August 1st 2014
Funding	European Research Council
Topic	Studies of local polarization in ferroelectric thin films by aberration corrected STE-EELS.
Center	Oak Ridge National Laboratory
Location	Oak Ridge, TN, 37830, USA
Date	November 10th – November 26th 2014
Funding	European Research Council
Topic	Analysis of charge transfer and induced magnetism at correlated oxide interfaces by aberration corrected STE-EELS.

Bibliography

1. Y. Tokura, H. Y. Hwang, *Condensed-matter physics: Complex oxides on fire. Nat. Mater*. **7** (2008), pp. 694–695.

2. J. Mannhart, D. G. Schlom, *Oxide interfaces--an opportunity for electronics.* Science. 327, 1607–1611 (2010).

3. H. Y. Hwang *et al.*, *Emergent phenomena at oxide interfaces.* Nat. Mater. 11, 103–13 (2012).

4. E. Dagotto, *Complexity in strongly correlated electronic systems.* Science. 309, 257–262 (2005).

5. E. Dagotto, T. Hotta, A. Moreo, *Colossal magnetoresistant materials: the key role of phase separation*. Phys. Rep. 344, 1–153 (2001).

6. M. Imada, A. Fujimori, Y. Tokura, *Metal-insulator transitions*. *Rev. Mod. Phys.* **70** (1998), pp. 1039–1263.

7. Y. Tokura, N. Nagaosa, *Orbital Physics in Transition-Metal Oxides*. *Science (80-.).* **288** (2000), pp. 462–468.

8. Y. Tokura, *Correlated-Electron Physics in Transition-Metal Oxides*. Phys. Today. 56, 50 (2003).

9. M. Varela *et al.*, *Materials Characterization in the Aberration-Corrected Scanning Transmission Electron Microscope*. Annu. Rev. Mater. Res. 35, 539–569 (2005).

10. N. F. Mott, *Metal-insulator transition*. *Rev. Mod. Phys.* **40** (1968), pp. 677–683.

11. E. Dagotto, *Nanoscale Phase Separation and Colossal Magnetoresistance* (Springer, 2003).

12. E. Benckiser *et al.*, *Orbital reflectometry of oxide heterostructures.* Nat. Mater. 10, 189–93 (2011).

13. A. Ohtomo, D. A. Muller, J. L. Grazul, H. Y. Hwang, *Artificial charge-modulationin atomic-scale perovskite titanate superlattices.* Nature. 419, 378–80 (2002).

14. A. Ohtomo, H. Y. Hwang, *A high-mobility electron gas at the $LaAlO_3/SrTiO_3$ heterointerface.* Nature. 427, 423–6 (2004).

15. A. Tebano *et al.*, *Evidence of Orbital Reconstruction at Interfaces in Ultrathin $La_{0.67}Sr_{0.33}MnO_3$ Films*. Phys. Rev. Lett. 100, 137401 (2008).

16. M. Calderón *et al.*, *Magnetoelectric coupling at the interface of $BiFeO_3/La_{0.7}Sr_{0.3}MnO_3$ multilayers*. Phys. Rev. B. 84, 1–5 (2011).

17. J. Garcia-Barriocanal *et al.*, *Colossal ionic conductivity at interfaces of epitaxial ZrO_2:$Y_2O_3/SrTiO_3$ heterostructures.* Science. 321, 676–80 (2008).

18. O. Scherzer, *Über einige Fehler von Elektronenlinsen*. Zeitschrift für Phys. A Hadron. Nucl. (1936).

19. O. Scherzer, *The Theoretical Resolution Limit of the Electron Microscope*. J. Appl. Phys. 20, 20 (1949).

20. M. Haider, S. Uhlemann, E. Schwan, H. Rose, *Electron microscopy image enhanced*. Nature. 392, 5–6 (1998).

21. O. L. Krivanek, N. Dellby, A. R. Lupini, *Towards sub-Å electron beams*. Ultramicroscopy. 78, 1–11 (1999).

22. O. L. Krivanek, P. D. Nellist, N. Dellby, M. F. Murfitt, Z. Szilagyi, *Towards sub-0.5 Å electron beams.* Ultramicroscopy. 96, 229–37 (2003).

23. R. Erni, M. Rossell, C. Kisielowski, U. Dahmen, *Atomic-Resolution Imaging with a Sub-50-pm Electron Probe*. Phys. Rev. Lett. 102, 1–4 (2009).

24. Y. Sawada, H. Shimura, N. Satoh, K. Okinishi, E. Hosokawa, F. Shibata, N. Ikuhara, *Resolving 45 pm with 300 kV Aberration Corrected STEM*. Microsc. Microanal. 20, 124–125 (2014).

25. O. L. Krivanek *et al.*, *Atom-by-atom structural and chemical analysis by annular dark-field electron microscopy*. Nature. 464, 571–574 (2010).

26. O. L. Krivanek, T. C. Lovejoy, N. Dellby, R. W. Carpenter, *Monochromated STEM with a 30 meV-wide, atom-sized electron probe.* Reprod. Syst. Sex. Disord. 62, 3–21 (2013).

27. O. L. Krivanek *et al.*, *Vibrational spectroscopy in the electron microscope*. Nature. 514, 209–212 (2014).

28. R. F. Egerton, *Electron Energy-Loss Spectroscopy in the Electron Microscope* (Springer US, Boston, MA, 2011).

29. J. Garcia-Barriocanal *et al.*, *"Charge leakage" at $LaMnO_3/SrTiO_3$ interfaces.* Adv. Mater. 22, 627–32 (2010).

30. M. von Ardenne, *Das Elektronen-Rastermikroskop. Praktische Ausführung*. Z. Tech. Phys. 19, 553–572 (1938).

31. M. von Ardenne, *Das Elektronen-Rastermikroskop - Theoretische Grundlagen*. Zeitschrift für Phys. 109, 553–572 (1938).

32. D. B. Williams, C. B. Carter, *The Transmission Electron Microscope* (Springer, 2009), vol. 2.

33. R. Erni, *Aberration-Corrected Imaging in Transmission Electron Microscopy* (Imperial College Press, 2010).

34. A. R. Lupini *et al.*, in *Nanocharacterisation*, J. Hutchison, K. Angus, Eds. (Royal Society of Chemistry, 2007), pp. 28–65.

35. A. R. Lupini, thesis, University of Cambridge (2001).

36. A. V. Crewe, D. B. Salzman, *On the optimum resolution for a corrected STEM*. Ultramicroscopy. 9, 373–377 (1982).

37. O. L. Krivanek *et al.*, *Gentle STEM: ADF imaging and EELS at low primary energies*. Ultramicroscopy. 110, 935–945 (2010).

38. K. Suenaga *et al.*, *Visualizing and identifying single atoms using electron energy-loss spectroscopy with low accelerating voltage.* Nat. Chem. 1, 415–8 (2009).

39. K. Suenaga, Y. Iizumi, T. Okazaki, *Single atom spectroscopy with reduced delocalization effect using a 30 kV-STEM*. Eur. Phys. J. Appl. Phys. 54, 33508 (2011).

40. S. J. Pennycook, *Z-contrast stem for materials science*. Ultramicroscopy. 30, 58–69 (1989).

41. S. J. Pennycook, *Seeing the atoms more clearly: STEM imaging from the Crewe era to today.* Ultramicroscopy. 123, 28–37 (2012).

42. A. Howie, L. D. Marks, S. J. Pennycook, *New imaging methods for catalyst particles*. Ultramicroscopy. 8, 163–174 (1982).

43. S. Kobayashi *et al.*, *Simultaneous visualization of oxygen vacancies and the accompanying cation shifts in a perovskite oxide by combining annular imaging techniques*. Appl. Phys. Lett. 100, 0–5 (2012).

44. S. D. Findlay *et al.*, *Dynamics of annular bright field imaging in scanning transmission electron microscopy.* Ultramicroscopy. 110, 903–23 (2010).

45. R. Ishikawa *et al.*, *Direct imaging of hydrogen-atom columns in a crystal by annular bright-field electron microscopy.* Nat. Mater. 10, 278–81 (2011).

46. S. D. Findlay, Y. Kohno, L. a Cardamone, Y. Ikuhara, N. Shibata, *Enhanced light element imaging in atomic resolution scanning transmission electron microscopy.* Ultramicroscopy. 136, 31–41 (2014).

47. R. Ishikawa, A. R. Lupini, S. D. Findlay, S. J. Pennycook, *Quantitative annular dark field electron microscopy using single electron signals.* Microsc. Microanal. 20, 99–110 (2014).

48. T. J. Pennycook *et al.*, *Efficient phase contrast imaging in STEM using a pixelated detector. Part 1: Experimental demonstration at atomic resolution*. Ultramicroscopy (2014).

49. N. Shibata, S. D. Findlay, Y. Ikuhara, *Atomic-Resolution Scanning Transmission Electron Microscopy with Segmented Annular All Field Detector*. Microsc. Microanal. 20, 64–65 (2014).

50. T. Pennycook, thesis, Vanderbilt University (2012).

51. S. Schamm, G. Zanchi, *Study of the dielectric properties near the band gap by VEELS: gap measurement in bulk materials.* Ultramicroscopy. 96, 559–64 (2003).

52. G. Brockt, H. Lakner, *Nanoscale EELS analysis of dielectric function and bandgap properties in gaN and related materials*. Micron. 31, 435–40 (2000).

53. M. Stöger-Pollach *et al.*, *Cerenkov losses: a limit for bandgap determination and Kramers-Kronig analysis.* Micron. 37, 396–402 (2006).

54. M. Stöger-Pollach, *Optical properties and bandgaps from low loss EELS: pitfalls and solutions.* Micron. 39, 1092–110 (2008).

55. S. Schamm, G. Zanchi, *Contamination and the quantitative exploitation of EELS low-loss experiments.* Ultramicroscopy. 88, 211–7 (2001).

56. C. Jeanguillaume, C. Colliex, *Spectrum-image: The next step in EELS digital acquisition and processing*. *Ultramicroscopy*. **28** (1989), pp. 252–257.

57. J. A. Hunt, D. B. Williams, *Electron energy-loss spectrum-imaging*. Ultramicroscopy. 38, 47–73 (1991).

58. N. Browning, M. Chisholm, S. Pennycook, *Atomic-resolution chemical analysis using a scanning transmission electron microscope*. Nature (1993).

59. M. Bosman *et al.*, *Two-Dimensional Mapping of Chemical Information at Atomic Resolution*. Phys. Rev. Lett. 99, 086102 (2007).

60. K. Kimoto *et al.*, *Element-selective imaging of atomic columns in a crystal using STEM and EELS.* Nature. 450, 702–704 (2007).

61. D. A. Muller *et al.*, *Atomic-scale chemical imaging of composition and bonding by aberration-corrected microscopy.* Science. 319, 1073–1076 (2008).

62. M. F. Chisholm, W. Luo, M. P. Oxley, S. T. Pantelides, H. N. Lee, *Atomic-Scale Compensation Phenomena at Polar Interfaces*. Phys. Rev. Lett. 105, 197602 (2010).

63. A. Borisevich, H. Chang, M. Huijben, *Suppression of octahedral tilts and associated changes in electronic properties at epitaxial oxide heterostructure interfaces*. Phys. Rev. Lett. 105, 087204 (2010).

64. Y. Gong *et al.*, *Band gap engineering and layer-by-layer mapping of selenium-doped molybdenum disulfide.* Nano Lett. 14, 442–9 (2014).

65. Y. Kim, J. Jeong, J. Kim, Y. Kim, *Image Processing of Atomic Resolution Transmission Electron Microscope Images*. J. Korean Phys. Soc. 48, 250–255 (2006).

66. P. L. Galindo *et al.*, *The Peak Pairs algorithm for strain mapping from HRTEM images.* Ultramicroscopy. 107, 1186–93 (2007).

67. P. L. Galindo, *High Resolution Peak Measurement and Strain Mapping using Peak Pairs Analysis*. Microsc. Anal. 23, 23–25 (2009).

68. P. Bevington, D. K. Robinson, *Data Reduction and Error Analysis for the Physical Sciences* (McGraw-Hill Science/Engineering/Math, ed. 3rd, 2002).

69. H. Shuman, A. P. Somlyo, *Electron energy loss analysis of near-trace-element concentrations of calcium.* Ultramicroscopy. 21, 23–32 (1987).

70. R. D. Leapman, C. R. Swyt, *Separation of overlapping core edges in electron energy loss spectra by multiple-least-squares fitting.* Ultramicroscopy. 26, 393–403 (1988).

71. P. Longo, P. J. Thomas, R. D. Twesten, *Atomic-Level EELS Mapping Using High-Energy Edges in Dualeels^{TM} Mode*. Micros. Today. 20, 30–36 (2012).

72. R. Door, D. Gängler, *Multiple least-squares fitting for quantitative electron energy-loss spectroscopy — an experimental investigation using standard specimens*. Ultramicroscopy. 58, 197–210 (1995).

73. K. Riegler, G. Kothleitner, *EELS detection limits revisited: Ruby — a case study*. Ultramicroscopy. 110, 1004–1013 (2010).

74. M. Bosman, M. Watanabe, D. T. L. Alexander, V. J. Keast, *Mapping chemical and bonding information using multivariate analysis of electron energy-loss spectrum images.* Ultramicroscopy. 106, 1024–1032 (2006).

75. E. R. Malinowski, *Factor Analysis in Chemistry* (Wiley, 3rd editio., 2002).

76. I. T. Jolliffe, *Principal Component Analysis* (Springer, 2nd editio., 2002).

77. M. Varela *et al.*, *Atomic-resolution imaging of oxidation states in manganites*. Phys. Rev. B. 79, 085117 (2009).

78. S. Lichtert, J. Verbeeck, *Statistical consequences of applying a PCA noise filter on EELS spectrum images*. Ultramicroscopy, 1–8 (2012).

79. J. a Mundy *et al.*, *Visualizing the interfacial evolution from charge compensation to metallic screening across the manganite metal-insulator transition.* Nat. Commun. 5, 3464 (2014).

80. O. L. Krivanek *et al.*, *An electron microscope for the aberration-corrected era.* Ultramicroscopy. 108, 179–95 (2008).

81. M. Varela, Z. Sefrioui, D. Arias, *Intracell Changes in Epitaxially Strained $YBa_2Cu_3O_{7-x}$ Ultrathin Layers in $YBa_2Cu_3O_{7-x}/PrBa_2Cu_3O_7$ Superlattices*. Phys. Rev. Lett. 83, 3936–3939 (1999).

82. D. W. Reagor, V. Y. Butko, *Highly conductive nanolayers on strontium titanate produced by preferential ion-beam etching.* Nat. Mater. 4, 593–6 (2005).

83. A. Singh *et al.*, *Transforming insulating rutile single crystal into a fully ordered nanometer-thick transparent semiconductor.* Nanotechnology. 21, 415303 (2010).

84. S. Facsko, *Formation of Ordered Nanoscale Semiconductor Dots by Ion Sputtering*. *Science (80-.).* **285** (1999), pp. 1551–1553.

85. U. Valbusa, C. Boragno, F. B. de Mongeot, *Nanostructuring surfaces by ion sputtering*. J. Phys. Condens. Matter. 14, 8153–8175 (2002).

86. S. Thiel, G. Hammerl, A. Schmehl, C. W. Schneider, J. Mannhart, *Tunable quasi-two-dimensional electron gases in oxide heterostructures.* Science (80-.). 313, 1942–5 (2006).

87. F. Bruno, J. Tornos, M. del Olmo, G. Santolino, *Anisotropic magnetotransport in $SrTiO_3$ surface electron gases generated by Ar^+ irradiation*. Phys. Rev. B. 83, 1–8 (2011).

88. V. Y. Butko, H. Wang, D. Reagor, *A magnetic field sensitive interfacial metallic state in a crystalline insulator*. Nanotechnology. 19, 305401 (2008).

89. H. Gross, N. Bansal, Y. S. Kimg, S. Oh, *Metal-insulator transition on $SrTiO_3$ surface induced by ionic-bombardment*. J. Appl. Phys. 110, 1–7 (2011).

90. D. Kan *et al.*, *Blue-light emission at room temperature from Ar^+-irradiated $SrTiO_3$*. Nat. Mater. 4, 816–819 (2005).

91. D. Kan *et al.*, *Blue luminescence from electron-doped $SrTiO_3$*. Appl. Phys. Lett. 88, 191916 (2006).

92. U. Diebold, *The surface science of titanium dioxide*. Surf. Sci. Rep. 48, 53–229 (2003).

93. A. Ghosh, F. Wakim, R. Addiss, *Photoelectronic Processes in Rutile*. Phys. Rev. 184, 979–988 (1969).

94. D. Cronemeyer, *Infrared Absorption of Reduced Rutile TiO_2 Single Crystals*. Phys. Rev. 113, 1222–1226 (1959).

95. K. Hashimoto, H. Irie, A. Fujishima, *TiO_2 Photocatalysis: A Historical Overview and Future Prospects*. Jpn. J. Appl. Phys. 44, 8269–8285 (2005).

96. M. P. Warusawithana *et al.*, *A ferroelectric oxide made directly on silicon*. Science (80-.). 324, 367 (2009).

97. Y. A. Abramov, V. G. Tsirelson, V. E. Zavodnik, S. A. Ivanov, *The chemical bond and atomic displacements in $SrTiO_3$ from X-ray diffraction analysis*. Acta Crystallogr. Sect. B Struct. Sci. 51, 942–951 (1995).

98. A. Okazaki, M. Kawaminami, *Lattice constant of strontium titanate at low temperatures*. Mater. Res. Bull. 8, 545–550 (1973).

99. D. A. Freedman, D. Roundy, T. A. Arias, *Elastic effects of vacancies in strontium titanate: Short- and long-range strain fields, elastic dipole tensors, and chemical strain*, 1–14 (2008).

100. J. Schooley, W. Hosler, M. L. Cohen, *Superconductivity in Semiconducting $SrTiO_3$*. Phys. Rev. Lett. 12, 474–475 (1964).

101. O. Tufte, P. Chapman, *Electron mobility in semiconducting strontium titanate*. Phys. Rev. 442, 4–10 (1967).

102. H. Frederikse, W. Thurber, W. Hosler, *Electronic transport in strontium titanate*. Phys. Rev. 134, 2–5 (1964).

103. G. Koster, B. L. Kropman, G. J. H. M. Rijnders, D. H. a. Blank, H. Rogalla, *Quasi-ideal strontium titanate crystal surfaces through formation of strontium hydroxide*. Appl. Phys. Lett. 73, 2920 (1998).

104. L. J. van der Pauw, *A method of measuring the resistivity and hall coefficient of lamellae of arbitrary shape*. Philips Tech. Rev. 26, 220 (1958).

105. Y. Tokura *et al.*, *Filling dependence of electronic properties on the verge of metal–Mott-insulator transition in* $Sr_{1-x}La_xTiO_3$. Phys. Rev. Lett. 70, 2126–2129 (1993).

106. R. Cowley, *The phase transition of strontium titanate*. Philos. Trans. R. Soc. London. Ser. A Math. Phys. Eng. Sci. 354, 2799 (1996).

107. A. Meldrum, L. A. Boatner, W. J. Weber, R. C. Ewing, *Amorphization and recrystallization of the* ABO_3 *oxides*. J. Nucl. Mater. 300, 242–254 (2002).

108. Y. Zhang *et al.*, *Response of strontium titanate to ion and electron irradiation*. J. Nucl. Mater. 389, 303–310 (2009).

109. B. Pabón *et al.*, *Formation of titanium monoxide (001) single-crystalline thin film induced by ion bombardment of titanium dioxide (110)*. Nat. Commun. 6 (2015).

110. G. Sánchez-Santolino *et al.*, *Characterization of surface metallic states in* $SrTiO_3$ *by means of aberration corrected electron microscopy.* Ultramicroscopy. 127, 109–113 (2012).

111. D. W. Fischer, *Molecular-Orbital Interpretation of the Soft X-Ray* $L_{II,III}$ *Emission and Absorption Spectra from Some Titanium and Vanadium Compounds*. J. Appl. Phys. 41, 3561 (1970).

112. L. A. Grunes, R. D. Leapman, N. Wilker, *Oxygen K near-edge fine structure: An electron-energy-loss investigation with comparisons to new theory for selected 3d transition-metal oxides*. Phys. Rev. B. 25 (1982).

113. R. D. Leapman, L. A. Grunes, P. L. Fejes, *Study of the* $L_{2,3}$ *edges in the 3d transition metals and their oxides by eels with comparisons to theory*. Phys. Rev. B. 26 (1982).

114. F. De Groot, M. Grioni, J. Fuggle, *Oxygen 1s x-ray-absorption edges of transition-metal oxides*. Phys. Rev. B. 40, 5715–5723 (1989).

115. H. Kurata, C. Colliex, *Electron-energy-loss core-edge structures in manganese oxides*. Phys. Rev. B. 48, 2102–2108 (1993).

116. M. Yoshiya, I. Tanaka, K. Kaneko, H. Adachi, *First principles calculation of chemical shifts in ELNES/NEXAFS of titanium oxides*. J. Phys. Condens. Matter. 11, 3217–3228 (1999).

117. E. Stoyanov, F. Langenhorst, G. Steinle-Neumann, *The effect of valence state and site geometry on Ti $L_{3,2}$ and O K electron energy-loss spectra of Ti_xO_y phases*. Am. Mineral. 92, 577–586 (2007).

118. S. Berger, S. Pennycook, *Detection of nitrogen at {100} platelets in diamond* (1982).

119. A. S. Hamid, *Atomic and electronic structure of oxygen vacancies and Nb-impurity in $SrTiO_3$*. Appl. Phys. A. 97, 829–833 (2009).

120. D. Ricci, G. Bano, G. Pacchioni, F. Illas, *Electronic structure of a neutral oxygen vacancy in $SrTiO_3$*. Phys. Rev. B. 68, 224105 (2003).

121. J. Ngai, Y. Segal, F. Walker, C. Ahn, *Electrostatic modulation of anisotropic magnetotransport in Ar^+-irradiated $SrTiO_3$: Effects of boundary scattering*. Phys. Rev. B. 83, 3–6 (2011).

122. R. Ormerod, *Solid oxide fuel cells*. Chem. Soc. Rev. (2003).

123. J. Goodenough, *Oxide-ion electrolytes*. Annu. Rev. Mater. Res. (2003).

124. J. Fergus, *Electrolytes for solid oxide fuel cells*. J. Power Sources (2006).

125. B. C. Steele, a Heinzel, *Materials for fuel-cell technologies.* Nature. 414, 345–52 (2001).

126. X. Guo, *Physical origin of the intrinsic grain-boundary resistivity of stabilized-zirconia: role of the space-charge layers*. Solid State Ionics. 2738 (1995).

127. D. Owen, A. Chokshi, *The high temperature mechanical characteristics of superplastic 3 mol% yttria stabilized zirconia*. Acta Mater. 46, 667–679 (1998).

128. M. Aoki, Y. Chiang, I. Kosacki, *Solute Segregation and Grain-Boundary Impedance in High-Purity Stabilized Zirconia*. J. Am. Ceram. Soc. (1996).

129. A. J. Verkerk, M. J.; Middelhuis, B. J. and Burggraaf, *Effect of grain boundaries on the conductivity of high-purity ZrO_2-Y_2O_3 ceramics*. Solid State Ionics. 6, 159–170 (1982).

130. K. Hayashi, T. Yamamoto, Y. Ikuhara, T. Sakuma, *Misorientation Dependence of Grain Boundary Resistivity in Nb-Doped Barium Titanate*. Key Eng. Mater. 181-182, 51–54 (2000).

131. S. Badwal, *Grain boundary resistivity in zirconia-based materials: effect of sintering temperatures and impurities*. Solid State Ionics. 76, 67–80 (1995).

132. C. Tian, *Ionic conductivities, sintering temperatures and microstructures of bulk ceramic CeO_2 doped with Y_2O_3*. Solid State Ionics. 134, 89–102 (2000).

133. X. Guo, J. Maier, *Grain boundary blocking effect in zirconia: a Schottky barrier analysis*. J. Electrochem. Soc. (2001).

134. X. Guo, W. Sigle, J. Maier, *Blocking Grain Boundaries in Yttria-Doped and Undoped Ceria Ceramics of High Purity*. J. Am. Ceram. Soc. 86, 77–87 (2003).

135. T. van Dijk, A. J. Burggraaf, *Grain boundary effects on ionic conductivity in ceramic $Gd_xZr_{1-x}O_{2-(x/2)}$ solid solutions*. Phys. Status Solidi. 63, 229–240 (1981).

136. T. Nakagawa *et al.*, *Oxygen diffusion blocking of single grain boundary in yttria-doped zirconia bicrystals*. J. Mater. Sci. 40, 3185–3190 (2005).

137. Y. Sato *et al.*, *Role of Pr Segregation in Acceptor-State Formation at ZnO Grain Boundaries*. Phys. Rev. Lett. 97, 106802 (2006).

138. A. Hayashi, K. Noi, A. Sakuda, M. Tatsumisago, *Superionic glass-ceramic electrolytes for room-temperature rechargeable sodium batteries*. Nat. Commun. (2012).

139. D. Pergolesi, E. Fabbri, A. D'Epifanio, *High proton conduction in grain-boundary-free yttrium-doped barium zirconate films grown by pulsed laser deposition*. Nat. Mater. (2010).

140. N. Balke *et al.*, *Nanoscale mapping of ion diffusion in a lithium-ion battery cathode.* Nat. Nanotechnol. 5, 749–54 (2010).

141. X. Guo, R. Waser, *Electrical properties of the grain boundaries of oxygen ion conductors: acceptor-doped zirconia and ceria*. Prog. Mater. Sci. 51, 151–210 (2006).

142. M. Frechero, *Paving the way to nanoionics: atomic origin of barriers for ionic transport through interfaces*. Sci. Rep. (2015).

143. J. Macdonald, E. Barsoukov, J. R. Barsoukov, Evgenij and Macdonald, *Impedance Spectroscopy: Theory, Experiment and Applications* (Wiley, 2nd Editio., 2005).

144. M. A. Frechero *et al.*, *Caracterización eléctrica de fronteras de grano en conductores iónicos mediante medidas de espectroscopia de impedancias en un bicristal*. Boletín la Soc. Española Cerámica y Vidr. 51, 13–18 (2012).

145. H. Scott, *Phase relationships in the zirconia-yttria system*. J. Mater. Sci. 10, 1527–1535 (1975).

146. W. Nernst, *On the electrolytic conduction of solid bodies at high temperatures*. Z. Electrochem (1899).

147. A. Pimenov, J. Ullrich, P. Lunkenheimer, A. Loidl, C. H. Ruscher, *Ionic conductivity and relaxations in $ZrO_2 - Y_2O_3$ solid solutions*. Solid State Ionics. 109, 111–118 (1998).

148. J. M. Dixon, L. D. LaGrange, U. Merten, C. F. Miller, J. T. Porter, *Electrical Resistivity of Stabilized Zirconia at Elevated Temperatures*. J. Electrochem. Soc. 110, 276 (1963).

149. I. R. Gibson, G. P. Dransfield, *Sinterability of commercial 8 mol% yttria-stabilized zirconia powders and the effect of sintered density on the ionic conductivity*. J. Mater. Sci. 33, 4297–4305 (1998).

150. A. K. Jonscher, *Dielectric relaxation in solids*. J. Phys. D. Appl. Phys. 32, R57–R70 (1999).

151. A. Rivera, J. Santamaría, C. León, *Electrical conductivity relaxation in thin-film yttria-stabilized zirconia*. Appl. Phys. Lett. 78, 610 (2001).

152. O. J. Durá *et al.*, *Ionic conductivity of nanocrystalline yttria-stabilized zirconia: Grain boundary and size effects*. Phys. Rev. B. 81, 184301 (2010).

153. C. W. Binns, K. J.; Lawrenson, P. J. and Trowbridge, *The analytical and numerical solution of electric and magnetic fields* (Wiley, New York, 1992), vol. 6.

154. S. Ramanathan, *Interface-mediated ultrafast carrier conduction in oxide thin films and superlattices for energy*. J. Vac. Sci. Technol. A Vacuum, Surfaces, Film. 27, 1126 (2009).

155. Z. Wang *et al.*, *Atom-resolved imaging of ordered defect superstructures at individual grain boundaries.* Nature. 479, 380–3 (2011).

156. M. Kim *et al.*, *Nonstoichiometry and the Electrical Activity of Grain Boundaries in $SrTiO_3$*. Phys. Rev. Lett. 86, 4056–4059 (2001).

157. Y. Yan *et al.*, *Impurity-Induced Structural Transformation of a MgO Grain Boundary*. Phys. Rev. Lett. 81, 3675–3678 (1998).

158. N. Shibata *et al.*, *Atomic-scale imaging of individual dopant atoms in a buried interface.* Nat. Mater. 8, 654–8 (2009).

159. R. F. Klie *et al.*, *Enhanced current transport at grain boundaries in high-T_c superconductors*. Nature. 435, 475–8 (2005).

160. Y. Lei, Y. Ito, N. D. Browning, T. J. Mazanec, *Segregation Effects at Grain Boundaries in Fluorite-Structured Ceramics*. J. Am. Ceram. Soc. 85, 2359–2363 (2002).

161. K. Matsui, H. Yoshida, Y. Ikuhara, *Grain-boundary structure and microstructure development mechanism in 2–8mol% yttria-stabilized zirconia polycrystals*. Acta Mater. 56, 1315–1325 (2008).

162. E. Dickey, X. Fan, S. Pennycook, *Structure and Chemistry of Yttria Stabilized Cubic Zirconia Symmetric Tilt Grain Boundaries*. J. Am. Ceram. Soc. 68 (2001).

163. R. L. González-Romero, J. J. Meléndez, D. Gómez-García, F. L. Cumbrera, a. Domínguez-Rodríguez, *Segregation to the grain boundaries in YSZ bicrystals: A Molecular Dynamics study*. Solid State Ionics. 237, 8–15 (2013).

164. P. E. Blöchl, *Projector augmented-wave method*. Phys. Rev. B. 50, 17953–17979 (1994).

165. G. Kresse, *From ultrasoft pseudopotentials to the projector augmented-wave method*. Phys. Rev. B. 59, 1758–1775 (1999).

166. G. Kresse, J. Hafner, *Ab initio molecular dynamics for liquid metals*. Phys. Rev. B. 47, 558–561 (1993).

167. G. Kresse, *Efficient iterative schemes for ab initio total-energy calculations using a plane-wave basis set*. Phys. Rev. B. 54, 11169–11186 (1996).

168. K. Kliewer, J. Koehler, *Space Charge in Ionic Crystals. I. General Approach with Application to NaCl*. Phys. Rev. 140, A1226–A1240 (1965).

169. J. Maier, *Ionic conduction in space charge regions*. Prog. Solid State Chem. 23, 171–263 (1995).

170. N. Reyren *et al.*, *Superconducting interfaces between insulating oxides.* Science (80-.). 317, 1196–9 (2007).

171. J. Wang *et al.*, *Epitaxial $BiFeO_3$ multiferroic thin film heterostructures.* Science (80-.). 299, 1719–22 (2003).

172. R. F. Berger, C. J. Fennie, J. B. Neaton, *Band Gap and Edge Engineering via Ferroic Distortion and Anisotropic Strain: The Case of $SrTiO_3$*. Phys. Rev. Lett. 107, 146804 (2011).

173. C. Jia *et al.*, *Oxygen octahedron reconstruction in the $SrTiO_3/LaAlO_3$ heterointerfaces investigated using aberration-corrected ultrahigh-resolution transmission electron microscopy*. Phys. Rev. B. 79, 081405 (2009).

174. Y.-M. Kim *et al.*, *Interplay of octahedral tilts and polar order in $BiFeO_3$ films.* Adv. Mater. 25, 2497–504 (2013).

175. J. H. Lee, K. T. Delaney, E. Bousquet, N. a. Spaldin, K. M. Rabe, *Strong coupling of Jahn-Teller distortion to oxygen-octahedron rotation and functional properties in epitaxially strained orthorhombic $LaMnO_3$*. Phys. Rev. B. 88, 174426 (2013).

176. G. H. Jonker, J. H. Van Santen, *Ferromagnetic compounds of manganese with perovskite structure*. Physica. 16, 337–349 (1950).

177. R. von Helmolt, J. Wecker, B. Holzapfel, *Giant negative magnetoresistance in perovskitelike $La_{2/3}$ $Ba_{1/3}$ MnO_x ferromagnetic films*. Phys. Rev. Lett. 71, 2331–2333 (1993).

178. R. M. Kusters, J. Singleton, D. A. Keen, R. McGreevy, W. Hayes, *Magnetoresistance measurements on the magnetic semiconductor $Nd_{0.5}Pb_{0.5}MnO_3$*. Phys. B Condens. Matter. 155, 362–365 (1989).

179. M. a. Gilleo, *Crystallographic studies of perovskite-like compounds. III. La(M_x, $Mn_{1-x}O_3$ with M = Co, Fe and Cr*. Acta Crystallogr. 10, 161–166 (1957).

180. J. B. A. A. Elemans, B. Van Laar, K. R. Van Der Veen, B. O. Loopstra, *The crystallographic and magnetic structures of $La_{1-x}Ba_xMn_{1-x}Me_xO_3$ (Me = Mn or Ti)*. J. Solid State Chem. 3, 238–242 (1971).

181. P. Norby; I. G. Krogh Andersen; and E. Krogh Andersen, *The Crystal Structure of Lanthanum Manganate(lll), $LaMnO_3$ at Room Temperature and at 1273 K under N_3*. J. Solid State Chem. 119, 191–196 (1995).

182. G. Sanchez-Santolino *et al.*, *Oxygen octahedral distortions in $LaMO_3/SrTiO_3$ superlattices.* Microsc. Microanal. 20, 825–31 (2014).

183. S. J. Pennycook, M. Varela, *New views of materials through aberration-corrected scanning transmission electron microscopy.* J. Electron Microsc. (Tokyo). 60 Suppl 1, S213–23 (2011).

184. M. Choi, F. Oba, Y. Kumagai, I. Tanaka, *Anti-ferrodistortive-Like Oxygen-Octahedron Rotation Induced by the Oxygen Vacancy in Cubic $SrTiO_3$*. Adv. Mater. 25, 86–90 (2013).

185. Ş. Smadici *et al.*, *Electronic Reconstruction at $SrMnO_3$-$LaMnO_3$ Superlattice Interfaces*. Phys. Rev. Lett. 99, 196404 (2007).

186. S. J. May *et al.*, *Enhanced ordering temperatures in antiferromagnetic manganite superlattices.* Nat. Mater. 8, 892–897 (2009).

187. J. P. Velev *et al.*, *Magnetic tunnel junctions with ferroelectric barriers: prediction of four resistance States from first principles.* Nano Lett. 9, 427–32 (2009).

188. V. Garcia *et al.*, *Giant tunnel electroresistance for non-destructive readout of ferroelectric states.* Nature. 460, 81–4 (2009).

189. A. Gruverman *et al.*, *Tunneling electroresistance effect in ferroelectric tunnel junctions at the nanoscale.* Nano Lett. 9, 3539–43 (2009).

190. P. Maksymovych *et al.*, *Polarization control of electron tunneling into ferroelectric surfaces.* Science. 324, 1421–5 (2009).

191. V. Garcia *et al.*, *Ferroelectric control of spin polarization.* Science. 327, 1106–10 (2010).

192. J. Junquera, P. Ghosez, *Critical thickness for ferroelectricity in perovskite ultrathin films*. Nature. 422, 506–509 (2003).

193. Z. Wen, C. Li, D. Wu, A. Li, N. Ming, *Ferroelectric-field-effect-enhanced electroresistance in metal/ferroelectric/semiconductor tunnel junctions.* Nat. Mater. 12, 617–21 (2013).

194. Y. W. Yin *et al.*, *Enhanced tunnelling electroresistance effect due to a ferroelectrically induced phase transition at a magnetic complex oxide interface.* Nat. Mater. 12, 397–402 (2013).

195. G. Catalan, J. Seidel, R. Ramesh, J. F. Scott, *Domain wall nanoelectronics*. Rev. Mod. Phys. 84, 119–156 (2012).

196. J. Seidel *et al.*, *Conduction at domain walls in oxide multiferroics.* Nat. Mater. 8, 229–34 (2009).

197. E. K. Salje, *Multiferroic domain boundaries as active memory devices: trajectories towards domain boundary engineering.* Chemphyschem. 11, 940–50 (2010).

198. M.-G. Han *et al.*, *Interface-induced nonswitchable domains in ferroelectric thin films*. Nat. Commun. 5, 1–9 (2014).

199. A. Urushibara, Y. Moritomo, T. Arima, A. Asamitsu, *Insulator-metal transition and giant magnetoresistance in* $La_{1-x}Sr_xMnO_3$. Phys. Rev. B. 51, 103–109 (1995).

200. J. Park, E. Vescovo, H. Kim, C. Kwon, *Direct evidence for a half-metallic ferromagnet*. Nature. 392, 794–796 (1998).

201. M. Salamon, M. Jaime, *The physics of manganites: Structure and transport*. Rev. Mod. Phys. 73, 583–628 (2001).

202. H. Fujishiro, T. Fukase, M. Ikebe, *Charge Ordering and Sound Velocity Anomaly in* $La_{1-x}Sr_xMnO_3$ $(X \geq 0.5)$. J. Phys. Soc. Japan. 67, 2582–2585 (1998).

203. J. M. D. Coey, M. Viret, S. von Molnár, *Mixed-valence manganites*. Adv. Phys. 48, 167–293 (1999).

204. Y. Konishi *et al., Orbital-State-Mediated Phase-Control of Manganites*. J. Phys. Soc. Japan. 68, 3790–3793 (1999).

205. M. Huijben *et al., Critical thickness and orbital ordering in ultrathin $La_{0.7}Sr_{0.3}MnO_3$ films*. Phys. Rev. B. 78, 094413 (2008).

206. T. Becker *et al., Intrinsic Inhomogeneities in Manganite Thin Films Investigated with Scanning Tunneling Spectroscopy*. Phys. Rev. Lett. 89, 237203 (2002).

207. M. Bibes *et al., Charge trapping in optimally doped epitaxial manganite thin films*. Phys. Rev. B. 66, 134416 (2002).

208. M. Bibes *et al., Nanoscale Multiphase Separation at $La_{2/3}Ca_{1/3}MnO_3/SrTiO_3$ Interfaces*. Phys. Rev. Lett. 87, 067210 (2001).

209. J. J. Wang, F. Y. Meng, X. Q. Ma, M. X. Xu, L. Q. Chen, *Lattice, elastic, polarization, and electrostrictive properties of $BaTiO_3$ from first-principles*. J. Appl. Phys. 108, 034107 (2010).

210. C. H. Ahn, K. M. Rabe, J.-M. Triscone, *Ferroelectricity at the nanoscale: local polarization in oxide thin films and heterostructures.* Science. 303, 488–91 (2004).

211. K. J. Choi *et al., Enhancement of ferroelectricity in strained $BaTiO_3$ thin films.* Science. 306, 1005–9 (2004).

212. N. Sai, A. Kolpak, A. Rappe, *Ferroelectricity in ultrathin perovskite films*. Phys. Rev. B. 72, 020101 (2005).

213. R. Nakao *et al., Critical thickness for ferroelectricity of $BaTiO_3$ by first-principles calculations*. Appl. Phys. Lett. 86, 222901 (2005).

214. G. Gerra, A. Tagantsev, N. Setter, K. Parlinski, *Ionic Polarizability of Conductive Metal Oxides and Critical Thickness for Ferroelectricity in $BaTiO_3$*. Phys. Rev. Lett. 96, 1–4 (2006).

215. X.-Y. Wang, Y.-L. Wang, R.-J. Yang, *Lattice model for strained nanoscale ferroelectric capacitors: Investigation on fundamental size limits in ferroelectricity*. Appl. Phys. Lett. 95, 142910 (2009).

216. T. Kolodiazhnyi, M. Tachibana, H. Kawaji, J. Hwang, E. Takayama-Muromachi, *Persistence of Ferroelectricity in $BaTiO_3$ through the Insulator-Metal Transition*. Phys. Rev. Lett. 104, 147602 (2010).

217. J. Hwang, T. Kolodiazhnyi, J. Yang, M. Couillard, *Doping and temperature-dependent optical properties of oxygen-reduced $BaTiO_{3-\delta}$*. Phys. Rev. B. 82, 214109 (2010).

218. Y. Wang, X. Liu, J. D. Burton, S. S. Jaswal, E. Y. Tsymbal, *Ferroelectric Instability Under Screened Coulomb Interactions*. Phys. Rev. Lett. 109, 247601 (2012).

219. M. Bowen *et al.*, *Nearly total spin polarization in $La_{2/3}Sr_{1/3}MnO_3$ from tunneling experiments*. Appl. Phys. Lett. 82, 233 (2003).

220. B. Anthony, J Bland, C Heinrich, *Ultrathin Magnetic Structures III* (Springer, 2005).

221. L. Kim, J. Kim, D. Jung, J. Lee, U. V. Waghmare, *Polarization of strained $BaTiO_3/SrTiO_3$ artificial superlattice: First-principles study*. Appl. Phys. Lett. 87, 052903 (2005).

222. C.-G. Duan, R. F. Sabirianov, W.-N. Mei, S. S. Jaswal, E. Y. Tsymbal, *Interface Effect on Ferroelectricity at the Nanoscale*. Nano Lett. 6, 483–487 (2006).

223. X. Liu, Y. Wang, P. Lukashev, J. Burton, E. Tsymbal, *Interface dipole effect on thin film ferroelectric stability: First-principles and phenomenological modeling*. Phys. Rev. B. 85, 1–8 (2012).

224. Y. Wang *et al.*, *Ferroelectric dead layer driven by a polar interface*. Phys. Rev. B. 82, 094114 (2010).

225. R. Pick, M. Cohen, R. Martin, *Microscopic theory of force constants in the adiabatic approximation*. Phys. Rev. B. 1 (1970).

226. P. Ghosez, J. Michenaud, X. Gonze, *Dynamical atomic charges: The case of ABO_3 compounds*. Phys. Rev. B. 58, 6224–6240 (1998).

227. I. MacLaren, R. Villaurrutia, B. Schaffer, L. Houben, A. Peláiz-Barranco, *Atomic-Scale Imaging and Quantification of Electrical Polarisation in Incommensurate Antiferroelectric Lanthanum-Doped Lead Zirconate Titanate*. Adv. Funct. Mater. 22, 261–266 (2012).

228. A. Y. Borisevich *et al., Interface dipole between two metallic oxides caused by localized oxygen vacancies*. Phys. Rev. B. 86, 140102 (2012).

229. C.-L. Jia *et al., Atomic-scale study of electric dipoles near charged and uncharged domain walls in ferroelectric films.* Nat. Mater. 7, 57–61 (2008).

230. C.-L. Jia *et al., Unit-cell scale mapping of ferroelectricity and tetragonality in epitaxial ultrathin ferroelectric films.* Nat. Mater. 6, 64–9 (2007).

231. M. Y. Gureev, a. K. Tagantsev, N. Setter, *Head-to-head and tail-to-tail 180^{°} domain walls in an isolated ferroelectric*. Phys. Rev. B. 83, 184104 (2011).

232. H. Chen, S. Ismail-Beigi, *Ferroelectric control of magnetization in $La_{1-x}Sr_xMnO_3$ manganites: A first-principles study*. Phys. Rev. B. 86, 1–13 (2012).

233. C.-G. Duan, S. Jaswal, E. Tsymbal, *Predicted Magnetoelectric Effect in $Fe/BaTiO_3$ Multilayers: Ferroelectric Control of Magnetism*. Phys. Rev. Lett. 97, 047201 (2006).

234. J. M. Rondinelli, M. Stengel, N. a Spaldin, *Carrier-mediated magnetoelectricity in complex oxide heterostructures.* Nat. Nanotechnol. 3, 46–50 (2008).

235. E. A. Eliseev, a. N. Morozovska, G. S. Svechnikov, V. Gopalan, V. Y. Shur, *Static conductivity of charged domain walls in uniaxial ferroelectric semiconductors*. Phys. Rev. B. 83, 235313 (2011).

236. Y.-M. Kim *et al.*, *Probing oxygen vacancy concentration and homogeneity in solid-oxide fuel-cell cathode materials on the subunit-cell level.* Nat. Mater. 11, 888–94 (2012).

237. J. Gazquez *et al.*, *Lattice mismatch accommodation via oxygen vacancy ordering in epitaxial $La_{0.5}Sr_{0.5}CoO_{3-\delta}$ thin films.* APL Mater. 1, 012105 (2013).

238. A. F. Santander-Syro *et al.*, *Two-dimensional electron gas with universal subbands at the surface of $SrTiO_3$.* Nature. 469, 189–93 (2011).